



university of
 groningen

faculty of science
 and engineering

kapteyn astronomical
 institute

UNIVERSITY OF GRONINGEN

MASTER THESIS

**An observational study of the $z \sim 4$
strongly lensed dusty star-forming galaxy
MM18423+5938**

Author:

Frits SWEIJEN
s2364883

Supervisors:

Dr. J. P. McKEAN
C. SPINGOLA

Second Reader:

Prof. Dr. L. V. E. Koopmans

Coordinator:

Prof. Dr. M. A. W. Verheijen

Kapteyn Astronomical Institute

August 4, 2017

"Our situation is like a puzzle box, Jane. Every time I think I know what is going on, suddenly there's another layer of complications."

John Perry - John Scalzi's *The Last Colony*

"Sometimes you gotta run before you can walk."

Working with radio data taught me this

University of Groningen

Abstract

Faculty of Science and Engineering
Kapteyn Astronomical Institute

Master of Science

**An observational study of the $z \sim 4$ strongly lensed dusty star-forming galaxy
MM18423+5938**

by Frits SWEIJEN
s2364883

In this thesis we present the result of a study on the strongly gravitationally lensed dusty star-forming galaxy (DSFG) MM18423+5938. We use data from the HST at $1.1 \mu\text{m}$ to discuss the lens morphology, which is more complex than it appears to be. With the VLA, we use 5 GHz observations to add a second photometric data point to the synchrotron part of the spectrum. The system is doubly imaged in the radio continuum, with $S_{5 \text{ GHz}} = 74 \pm 19 \text{ mJy}$. We find a spectral index of $\alpha = -0.83 \pm 0.34$; consistent with other DSFG samples. The molecular gas content was studied through CO(1-0) and CO(2-1) emission using both previously published data and archival data. We find the CO(1-0) line intensity to be $I_{\text{CO}(1-0)} = 0.5 \pm 0.3 \mu^{-1} \text{Jy km s}^{-1}$ with a line luminosity of $L'_{\text{CO}(1-0)} = 3.1 \pm 1.9 \times 10^{11} \mu^{-1} \text{K km s}^{-1} \text{pc}^2$, resulting in a molecular gas mass of $M_{\text{gas}} = 2.5 \pm 0.5 \times 10^{11} \mu^{-1} M_{\odot}$. For the CO(2-1) emission we find a lensed line intensity $I_{\text{CO}(2-1)} = 2.8 \pm 1.5 \mu^{-1} \text{Jy km s}^{-1}$, where μ is the magnification, resulting in a line luminosity of $L_{\text{CO}(2-1)'} = 4.5 \pm 0.8 \times 10^{11} \mu^{-1} \text{K km s}^{-1} \text{pc}^2$. We identify a possible double peak profile, which would be a hint of a rotating disk, but detailed dynamical modeling is required to test this. Splitting the line into a (relative) red, green and blue part shows different spatial structures, further hinting at a rotating structure. Finally $250 \mu\text{m}$, $350 \mu\text{m}$ and $500 \mu\text{m}$ measurements from the Herschel Observatory were used to constrain the peak of the SED. We fitted an MBB and power law to the spectrum. From the SED, we then obtained $T_d = 37.8_{-1.9}^{+2.0} \text{ K}$, $\beta = 1.7 \pm 0.2$, $L_{\text{FIR}} = 9.76 \pm 0.30 \times 10^{13} \mu^{-1} L_{\odot}$, $q = 2.59 \pm 0.47$ and $\text{SFR} = 1.7 \times 10^4 \mu^{-1} M_{\odot} \text{yr}^{-1}$. All of the parameters are consistent with other, unlensed DSFGs assuming a magnification $\mu \sim 12$, where applicable.

Acknowledgements

First I would like to thank my supervisor John McKean for providing this research opportunity and guiding me through it. I also thank the members of the radio lensing group at Kapteyn for their input during group meetings, for always being willing to help answer questions about data reduction or interpretation of results or lending a coffee card for some extra fuel. Finally I want to thank the second reader Leon Koopmans and master research coordinator Marc Verheijen for taking time to read this thesis.

Contents

Abstract	iii
Acknowledgements	v
1 Introduction	1
1.1 Dusty Star-forming Galaxies	4
1.2 Gravitational Lensing	6
1.3 MM18423+5938	13
1.4 Thesis Outline	16
2 Observations and Data Reduction	17
2.1 HST	17
2.1.1 Observations	17
2.1.2 Dithering	20
2.1.3 Combining Images with AstroDrizzle	21
2.1.4 Fitting Objects with Galfit	31
2.2 VLA	33
2.2.1 Observations	34
2.2.2 Data Reduction	36
Radio Astronomy: Observing with Interferometers	36
Radio Astronomy: The Measurement Equation	40
Calibration of VLA Data	40
2.3 Herschel	56
2.3.1 Observations and Data Reduction	56
3 Results	59
3.1 1.1 μm Emission	59
3.2 5 GHz Radio Continuum Emission	61
3.3 Molecular Line Emission	65
3.3.1 The CO(1-0) Transition	65
3.3.2 The CO(2-1) Transition	74
3.4 250, 350 and 500 μm Sub-mm Emission and SED Fitting	84
3.4.1 SED Fitting	84
4 Interpretation	89
4.1 Continuum	89
4.2 The Molecular Gas	91
4.3 Heated Dust Emission	95

4.3.1	Radio-FIR Correlation and SFR	97
5	Conclusion	103
5.1	Future Studies	105
A	VLA Calibration Script	115

Chapter 1

Introduction

UNTIL the early 17th century, humankind had only been able to study the Universe with a pair of eyes and a curious mind. It was from this moment in time that we could embark on a new journey, exploring the vast cosmic ocean we call space. Starting from humble optical telescopes of a few centimeters in diameter, technology and science has advanced rapidly over the last decades in ways that were difficult to imagine a mere century ago. Astronomy is now a high-tech, multi-wavelength area of research implementing state-of-the-art technology to push back further the scientific frontier. Advanced techniques such as adaptive optics are used on large meter-sized optical telescopes such as the VLT and Keck to minimize the atmospheric effects on Earth. Giant radio telescopes which are tens to hundreds of meters in size (WSRT, IRAM, Effelsberg, Arecibo) gaze upon the sky to reveal the insides of heavily obscured, dust-enshrouded regions in galaxies. Finally, cryogenically cooled telescopes were launched into space to hunt for the faintest of radiation. Even today we are still going. With new telescopes on the horizon, such as the 40 meter E-ELT, the LSST, JWST or the SKA, we are going to probe space on an unprecedented scale and sensitivity, bringing us another step closer to unraveling the mysteries of the Universe.

How galaxies form, or structure in general to some extent, is still an open question. Various types of dark matter can reproduce certain aspects of structure, but we have yet to find a model that reproduces all of the features we see today. The currently accepted cosmological model is that of a flat, matter-dominated Universe filled with mostly cold dark matter and having a non-zero cosmological constant dominating the energy density: the Λ CDM cosmological model. The energy density of the Universe at a redshift z is related to the Hubble constant by

$$\left(\frac{H(z)}{H_0}\right)^2 = \Omega_{\Lambda,0} + \Omega_{k,0}(1+z)^2 + \Omega_{m,0}(1+z)^3 + \Omega_{r,0}(1+z)^4 \quad (1.1)$$

where Ω_{Λ} , Ω_k , Ω_m and Ω_r are the dark energy, curvature, matter and radiation energy densities, respectively. A subscript 0 indicates the current value at $z = 0$. Hence, for the Universe *now* this reduces to

$$1 = \Omega_{\Lambda} + \Omega_k + \Omega_m + \Omega_r. \quad (1.2)$$

Assuming a matter dominated ($\Omega_r = 0$) and flat ($\Omega_k = 0$) Universe, we obtain the well known relation

$$\Omega_{\Lambda} + \Omega_m = 1 \quad (1.3)$$

in the case of a Λ CDM cosmology. The latest Planck results [[Planck Collaboration](#)

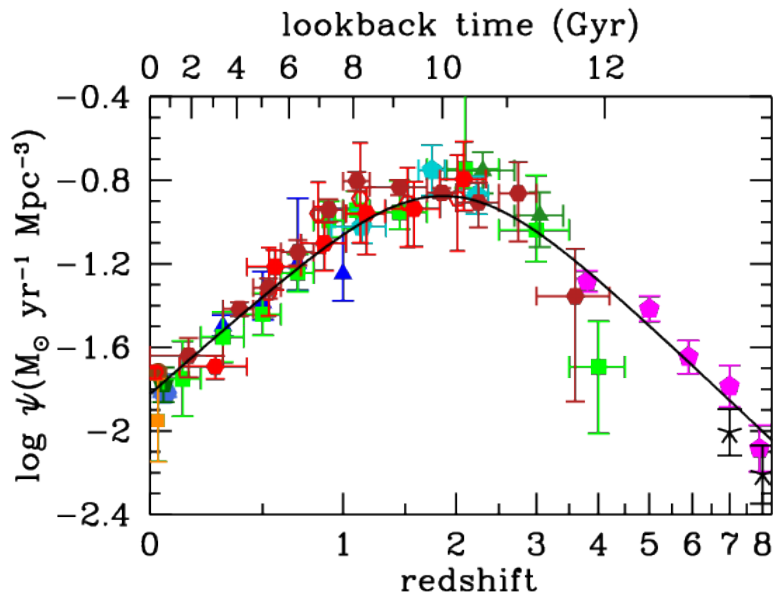


FIGURE 1.2: The SFR density as a function of redshift as presented in [Madau and Dickinson 2014](#). The red symbols are derived from IR measurements. The other symbols are derived from FUV measurements. The solid black line is the best fit.

the early Universe merged into larger objects that would eventually form galaxies at their centers. To test this idea, large surveys have been conducted to study the large scale structure of the Universe, but these surveys can also be used to study galaxy populations and the formation of stars at both low and high redshift in multiple parts of the electromagnetic spectrum. In the optical there are for example the *SDSS* and *VIPER* surveys (e.g. [Duarte Puertas et al. 2017](#); [Siudek et al. 2017](#)) probing out to $z \sim 1$, and the *VUDS* or *z9-CANDELS* pushing the boundaries to $z \sim 6$ and $z \sim 10$, respectively (e.g. [Tasca et al. 2015](#); [Bouwens et al. 2016](#)). The current record for the highest redshift galaxy is held by [\[Oesch et al. 2016\]](#) who spectroscopically confirmed a $z_{\text{grism}} = 11.09^{+0.08}_{-0.12}$ galaxy with the HST. In the radio regime surveys like the *USS* survey with the GMRT and the *VLA-COSMOS* survey with the VLA probe galaxies from nearby up to about $z \sim 6$ (e.g. [Intema et al. 2017](#); [Carilli et al. 2007](#)). Finally the *H-ATLAS* surveyed the sky in the FIR part of the electromagnetic spectrum (e.g. [Pearson et al. 2013](#)). As large surveys are always a compromise between sensitivity and area, the data may not have optimal signal-to-noise ratio for all sources. Therefore candidates usually need to be selected for specific follow-up observations; possibly limiting the number of objects available for a given scientific goal.

The first stars already formed early on around $z \sim 30$ bringing an end to the dark ages and starting the reionization of the Universe [[Barkana and Loeb 2001](#)]. Later the stars coalesced into larger structures to form galaxies. The galaxies then continued forming stars and started building up the stellar mass in the Universe. In Fig. 1.2 the SFR density is shown as a function of redshift. We see that it steadily increases up till a redshift of $z \sim 2$, after which it decreases to its present day value. This is an indication

that on average the SFR itself was probably the highest around this redshift as well. In the 1980s, measurements taken with the *Infrared Astronomical Satellite* (IRAS) revealed that a significant amount of radiation was emitted at infrared wavelengths; comparable to the amount of radiation emitted by optical objects. Dust absorbs the UV radiation from young hot stars and reprocesses this into infrared radiation. An important implication of this was that there might be an entire population of heavily dust-obscured galaxies not seen in the optical [Casey et al. 2014; Soifer et al. 1986]. For galaxies at high redshift, the infrared emission is redshifted into sub-mm wavelengths. Surveys in this part of the spectrum would thus confirm the presence of star forming galaxies at high redshift. It was later discovered that some of these galaxies were forming stars at extreme rates and had IR luminosities comparable to local ULIRGS.

1.1 Dusty Star-forming Galaxies

To detect the galaxies that would make up this hidden population, surveys were initiated with the *James Clerk Maxwell Telescope* (JCMT) at $850 \mu\text{m}$. This indeed revealed a population of galaxies being bright in the sub-mm, implying dust-heated star formation activity [Casey et al. 2014; Smail et al. 1997; Barger et al. 1998]. Now that there was a confirmed population of high-redshift dusty star-forming galaxies, follow up surveys began to gather more samples. In the last decade and a half surveys, in the far-infrared to submm have been conducted, along with interferometric follow up of selected sources using for example the VLA, ALMA or even VLBI. Notable examples are observations of the *Cosmological Evolution Survey* (COSMOS) field at millimeter wavelengths by MAMBO (1.2 mm , Bertoldi et al. 2007) and AzTEC (1.1 mm , Scott et al. 2008), mapping 400 arcmin^2 and 0.3 deg^2 , respectively, finding 31 sources combined. The Herschel Space Observatory conducted large surveys mapping approximately 570 deg^2 with the *Herschel Astrophysical Terahertz Large Area Survey* (H-ATLAS) and another 380 deg^2 with the *Herschel Multi-tiered Extragalactic Survey* (HerMES) [Eales et al. 2010; Oliver et al. 2012] adding more samples to the collection.

The radio-FIR correlation discussed by Condon 1992, tells us there is a relation between emission in the FIR and emission in the radio. If this relation remains valid to higher redshifts for sub-mm galaxies, then they are expected to be faint radio sources as well. Generally, this trend seems to be true with a value of $q_{\text{IR}} \approx 2.4$ (for the definition see Chapter 3), however there has been some discussion about the evolution of this correlation e.g. Ivison et al. 2010b; Ivison et al. 2010a; Murphy 2009; Bell 2003. In 2003 Chapman et al. did optical follow up with the Keck telescope in an attempt to get accurate redshifts for ten dusty star-forming galaxies that were selected to be representative for the population. Using spectroscopy they found a median redshift of 2.4, implying dusty star-forming galaxies are predominantly a (relatively) high-redshift population. In 2010, Lima et al. found a consistent result by analyzing the BLAST, SCUBA, AzTEC and SPT surveys from which they found that most of the DSFGs have a redshift larger than 2. Carilli and Walter 2013 discuss that the selection technique used in Chapman et al. 2003 suffers from a low-redshift bias however. Using lensing and molecular spectroscopic follow up we have indeed discovered dusty star-forming galaxies at higher redshifts even up to $z \sim 5$ or 6 (e.g. Riechers et al. 2017; Riechers et al. 2011a; Ikarashi et al. 2017; Vieira et al. 2013; Daddi et al. 2009).

The nature of their emission makes dusty star-forming galaxies most easily detected in the FIR to sub-mm wavelengths. We can use this to our advantage to learn about their star formation rate. In [Kennicutt 1998b](#), a relation between the FIR luminosity of a galaxy and its star formation rate

$$\text{SFR} = \frac{L_{\text{FIR}}}{5.8 \cdot 10^9 L_{\odot}} M_{\odot} \text{ yr}^{-1} \quad (1.4)$$

was introduced, assuming a Salpeter IMF. In this thesis I will follow the definition of L_{FIR} as defined in [Kennicutt 1998a](#):

$$L_{\text{FIR}} = L_{8\mu\text{m}-1000\mu\text{m}}. \quad (1.5)$$

Quite often measurements are not available over this entire range, but only near the peak as the emission is brightest here. Therefore, a conversion is done from measurements near the peak to obtain an estimate of the total FIR luminosity. The IR luminosity is defined here between $42.5 \mu\text{m}$ and $122.5 \mu\text{m}$ ¹ as in [Helou et al. 1988](#):

$$L_{\text{IR}} = L_{42.5\mu\text{m}-122.5\mu\text{m}}. \quad (1.6)$$

This is converted to a total FIR luminosity by

$$L_{\text{FIR}} = 1.91 \times L_{\text{IR}} \quad (1.7)$$

as in [Chapman et al. 2010](#). Using either Eqn. 1.4 to convert the high FIR luminosities $\gtrsim 10^{12} L_{\odot}$ to a star formation rate or studying the IR emission of dusty star-forming galaxies by other means implies star formation rates in these objects of hundreds to thousands of solar masses per year [[Chapman et al. 2010](#); [Rowan-Robinson et al. 2017](#); [Ivion et al. 2010b](#); [Ivion et al. 2010a](#)]. The star formation rate in our Milky Way ($1.7 M_{\odot} \text{ yr}^{-1}$ [[Robitaille and Whitney 2010](#)]; $1.65 \pm 0.19 M_{\odot} \text{ yr}^{-1}$ [[Licquia and Newman 2015](#)]) dwarfs in comparison. While some of these galaxies seem to harbor an AGN that can contaminate the sample (as they can also reach high FIR luminosities), they only make up approximately $\sim 20\%$ of samples, while the remaining $\sim 80\%$ is starburst dominated [[Coppin et al. 2010](#); [Hainline et al. 2009](#)].

The next question is then how these starbursts are fueled. Such high rates of star formation would require large amounts of gas and short depletion times of these reservoirs. A rough estimate with gas masses of $M_{\text{gas}} \sim 10^{10} - 10^{11} M_{\odot}$ and $\text{SFR} \sim 10^2 - 10^3 M_{\odot} \text{ yr}^{-1}$ would mean the gas is consumed in a few 10 to 100 Myr. [Carilli and Walter 2013](#) indeed point out gas consumption timescales of $\leq 10^7$ yr for DSFGs in their review. [Toft et al. 2014](#) estimate timescales of $\tau_{\text{burst}} = 42_{-29}^{+40}$ Myr for the duration of these starburst events as well; mentioning their result is consistent with other independent estimates. To bring in the required amount of gas two scenarios have been proposed: *high-redshift, gas-rich major mergers* and *cold mode accretion* (CMA) from the cosmic web. These two scenarios also distinguish between computational techniques; the former uses semi-analytical models (SAM), while the latter uses numerical simulations [[Engel et al. 2010](#)]. Many authors provide evidence for dusty star-forming galaxies being a result of a major merger. The arguments have varying origins, being based for example on gas or dynamical masses, mass ratios between binaries, comparisons with local ULIRGS, stellar populations in compact quiescent galaxies or the physical structure of the gas reservoir(s). See for example [Toft et al.](#)

¹Note that [Helou et al. 1988](#) defines *this* to be L_{FIR} . To avoid confusion double check which definition the literature in question is using.

2014 and references therein, and [Tacconi et al. 2008](#); [Riechers et al. 2011a](#); [Riechers et al. 2011b](#); [Wuyts et al. 2010](#); [Engel et al. 2010](#) and [Rybak et al. 2015b](#). In this way the gas is thus supplied by wet mergers. Feedback processes such igniting an AGN then quench star formation after a short while and the galaxies then evolve passively. The idea for this scenario comes from the fact that dusty star-forming galaxies seem to be a high-redshift analogue to local ULIRGS such as Arp220, which are merger-induced starbursts. A possible problem for this scenario however is that there are some dusty star-forming galaxies that have evidence for a disk or disk-like, extended structure of gas. Something that is not expected (but not impossible) from a merger. One example of such an object is the by now well studied $z = 4$ dusty star-forming galaxy GN20 [[Carilli et al. 2010](#); [Casey et al. 2009](#); [Hodge et al. 2015](#); [Hodge et al. 2011](#)]. Another issue with the merger scenario is that the process of massive mergers cannot fully explain the observed number density of DSFGs. In [Davé et al. 2010](#) this is quantified around $z = 2$. Based on results from [Narayanan et al. 2009](#) they show that the predicted number density is still an order of magnitude below the observed value.

In search for a solution, another scenario for accretion was introduced: CMA. The idea of cold accretion was explored some time ago already by [Finlator et al. 2006](#); [Dekel et al. 2009](#) and [Kereš et al. 2009](#) with hydrodynamical simulations. [Davé et al. 2010](#) expand on this previous research with a larger sample of 41 simulated dusty star-forming galaxies. In their simulation, the galaxies sit in large potential wells and are fed by smooth infall and gas-rich satellites [[Davé et al. 2010](#)]. Since DSFGs around $z = 2$ are compact, disturbed systems in general, this cannot immediately be interpreted as the result of a merger. The finding of star formation happening in extended regions of a few kpc instead of being confined to the inner core as, with local ULIRGS, is also brought up as an indication for CMA as an alternative. It is possible however to get extended regions of star formation from mergers so they do not draw any conclusions from this. With their simulations [Davé et al. 2010](#) are able to reproduce the observed number density and stellar masses of DSFGs, but they fail to reproduce the star formation rates by a factor of roughly 4 or less. This is one of the reasons why it is still unknown what exactly fuels the star formation in these objects. As pointed out by both [Davé et al. 2010](#) and [Engel et al. 2010](#), there has not yet been a model that satisfactory reproduces the observed number densities, stellar masses or star formation rates all at the same time. Recently [Narayanan et al. 2015](#) have succeeded to simulate a DSFG that is in reasonable agreement with observational constraints. The results of their simulation implies that these galaxies are not short lived, merger-induced starburst phenomena, but long lasting and fueled by infalling gas.

1.2 Gravitational Lensing

As DSFGs reside at moderately high redshifts, they have a reasonable chance of being lensed by a (massive) foreground galaxy. At the price of giving us a distorted view of the object, gravitational lensing can greatly magnify the flux density of the object being lensed. Since DSFGs are still relatively weak sources (of the order of mJy) the magnification of their flux density introduced by lensing allows for detection of these objects at higher redshifts than would normally be possible or better detection at similar redshifts compared to non-lensed DSFGs. One has of course to be lucky to find such a system in the first place, hence searching for lensed DSFGs is best done with large surveys. Besides allowing us to study faint objects at distances normally

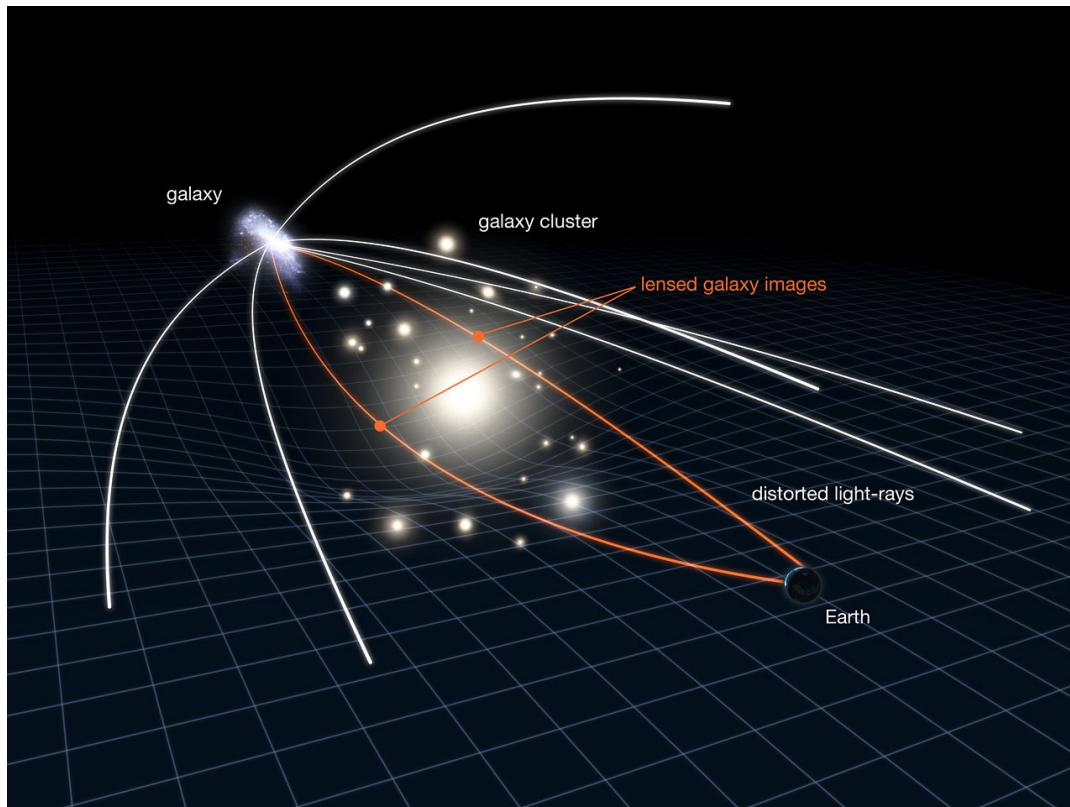


FIGURE 1.3: A basic illustration of a background galaxy being lensed by a foreground cluster of galaxies. The white and orange rays represent light rays emitted from the background galaxy. Credit: NASA, ESA&L. Calçada

unaccessible, gravitational lensing can also help us understand the spatial distribution of mass in the lensing galaxies (or clusters), help us study dark matter and the geometry of the Universe as angular diameter distances change if this geometry changes [Treu 2010]. Figure 1.3 shows a basic illustration of strong lensing. Light rays from the source are bent around the lens causing our view of the object to be magnified, but distorted.

Weak vs. Strong

In the context of gravitational lensing we can differentiate between two regimes: strong lensing and weak lensing. These correspond to different scales and different degrees of alignment between the lensing galaxy and the object being lensed.

Weak lensing is as its name implies a weak effect. The background galaxy appears only slightly distorted and there is no major magnification. Weak lensing is only detected in ensembles of sources manifesting itself, for example, as an apparent alignment of galaxies [Bartelmann and Schneider 2001]. Strong lensing on the other hand is easily identified. The key of a strong lens is multiple images, arc segments or (if you are lucky) a complete Einstein ring and a moderate to high magnification. For strong lensing we can distinguish cases of macrolensing, millilensing and microlensing, as mentioned in Treu 2010. On the smallest scales, down to micro arcseconds, we have *microlensing* caused by individual stars in the lensing halo resulting in small, rapid fluctuations in the magnification. In Figure 1 of Pooley et al. 2009, it is demonstrated with the quasar PG1115+080 that microlensing can change the magnification pattern quite rapidly. Images are seen to appear and disappear over the course of

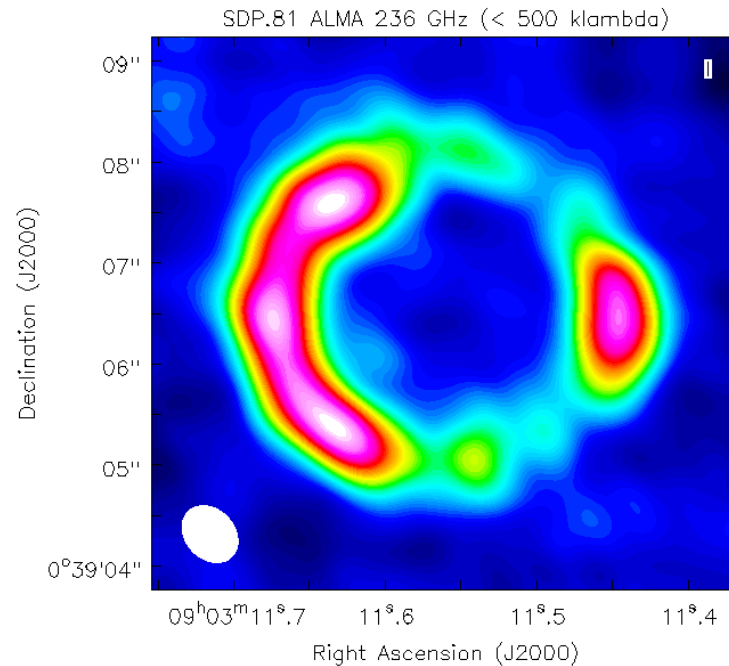


FIGURE 1.4: An ALMA continuum image at 236 GHz as presented in [Rybak et al. 2015a](#). There are three images on the left and a fourth on the right. Careful inspection shows that there may also be a low surface brightness Einstein ring.

eight years. *Millilensing* plays a role on slightly larger scales of milliarcseconds. This can be caused by small companions or satellites of the lensing galaxy. This effect can also be used to search for or study (dark matter) substructure on kiloparsec scales in the lens galaxy; see for example [Moustakas and Metcalf 2003](#); [Koopmans 2005](#); [Vegetti and Koopmans 2009](#); [Nierenberg et al. 2017](#). The presence of small scale substructure can be inferred by looking for deviations from a smooth model. If such a simple model leaves residuals than that may be evidence of substructure in the lens. The aforementioned simple, smooth model is called a macro model. This is a model to reproduce macroscopic properties of the lens, such as the Einstein radius and the number of images. Such a model is often represented by a *Singular Isothermal Ellipsoid* (SIE) for which solutions were presented in [Kormann et al. 1994](#). Figure 1.4 shows an ALMA continuum image by [Rybak et al. 2015a](#) of SDP.81 clearly showing strong lensing with multiple images and a hint of a low surface brightness Einstein ring. According to [Collett 2015](#) there are now several hundred strong lens systems known.

Lensing Theory

To conclude this short introduction to lensing the general framework behind it and some important concepts that will be needed are introduced. In Fig. 1.5 the basic geometry in lensing is shown. The various symbols are explained in Tab. 1.1.

In this case we will also make use of the *thin-lens approximation*. In this approximation we consider the lens thickness to be negligible and collapse it into a single plane. We can then derive an important equation by using the small angle approximation by using the small angle approximation. The angles β , α and θ can be related to each other through the angular

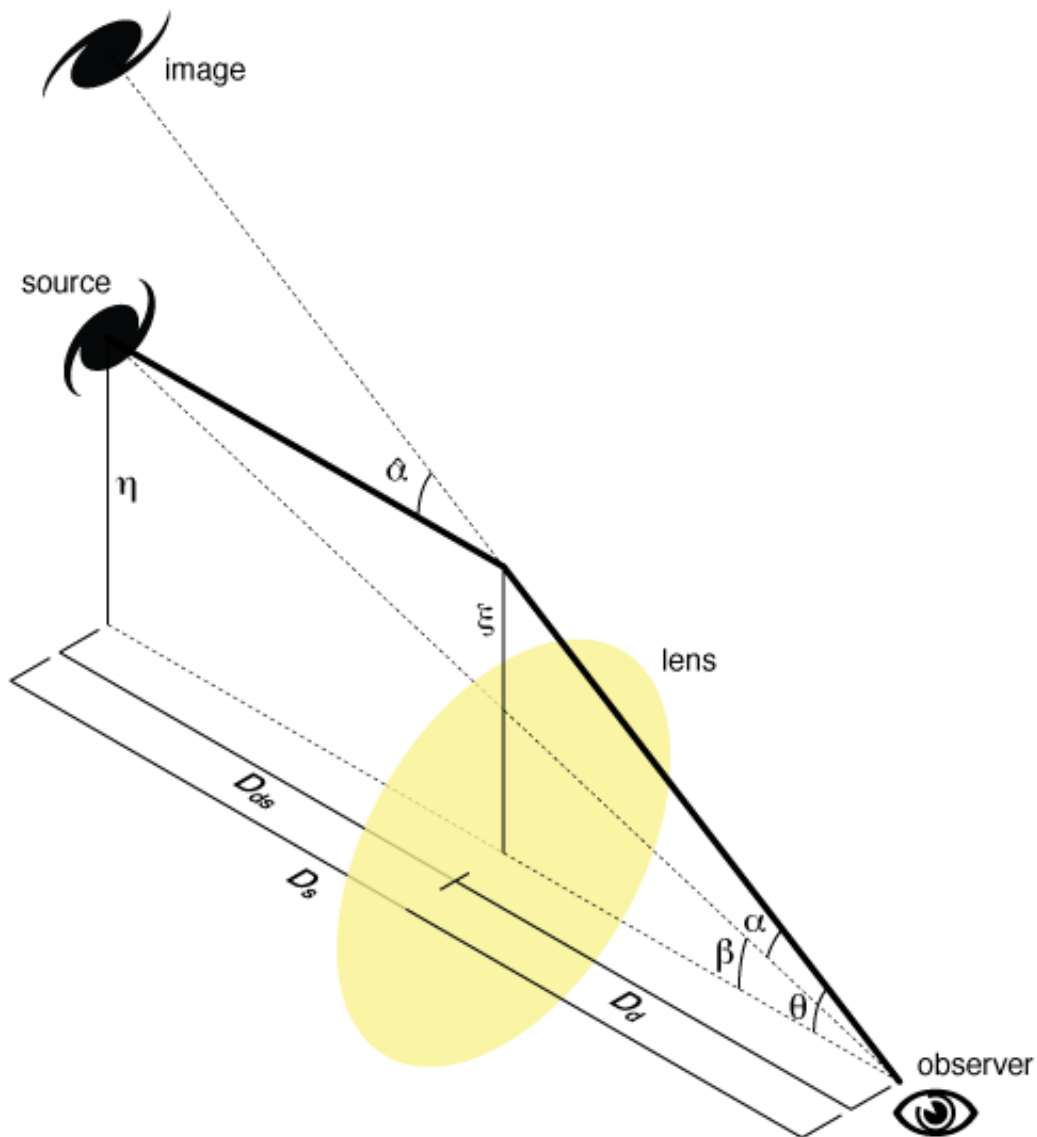


FIGURE 1.5: A simple representation of the assumed geometry for a source being strongly lensed by a deflector. In the case of a relatively weak gravitational field we can explain lensing with this geometry.

SYMBOL	MEANING
α	Scaled deflection angle.
$\hat{\alpha} \equiv \frac{D_{ds}}{D_s} \alpha$	Deflection angle.
β	True angular position of the source.
θ	Apparent angular position of the source.
D_{ds}	Angular diameter distance from the deflector to the source.
D_d	Angular diameter distance from the observer to the deflector.
D_s	Angular diameter distance from the observer to the source.
$\xi = D_d \theta$	The impact parameter.

TABLE 1.1: Legend to Fig. 1.5

diameter distances as

$$D_s\theta = D_s\beta + D_{ds}\hat{\alpha}. \quad (1.8)$$

Rearranging terms we can write

$$\beta = \theta - \frac{D_{ds}}{D_s}\hat{\alpha} \quad (1.9)$$

and by defining the scaled deflection angle $\alpha \equiv \frac{D_{ds}}{D_s}\hat{\alpha}$ we derive the *lens equation*

$$\beta = \theta - \alpha. \quad (1.10)$$

This is a linear relation between the deflection angle α to the source and image positions β and θ . If α itself is now a linear function of θ then there is only one solution as two linear functions will only intersect each other once. On the other hand if α is a *non-linear* function there can be multiple values of θ satisfying Eqn. 1.10 for a given β , i.e. multiple images can be produced. To quantify this let's assume a lens with a constant surface density Σ . The deflection angle then becomes

$$\alpha(\theta) = \frac{4\pi G}{c^2} \frac{D_d D_{ds}}{D_s} \Sigma \theta. \quad (1.11)$$

In the case $\beta = 0$ we can define the *critical surface density*

$$\Sigma_{crit} \equiv \frac{c^2}{4\pi G} \frac{D_s}{D_d D_{ds}} \quad (1.12)$$

which allows us to define a dimensionless parameter for the mass density called the **convergence**

$$\kappa = \frac{\Sigma}{\Sigma_{crit}}. \quad (1.13)$$

This parameter allows us to set a condition for multiple images (strong lensing) to occur:

$$\begin{cases} \text{Strong lensing: } \kappa > 1 \\ \text{Weak lensing: } \kappa < 1 \end{cases} \quad (1.14)$$

where $\kappa = 1$ is the transition from weak to strong lensing. This transition allows us to derive another important lensing quantity as $\kappa = 1$ corresponds to $\beta = 0$. By slightly rewriting Eqn. 1.11 as

$$\alpha(\theta) = \frac{4G}{c^2} \frac{D_{ds}}{D_s} \Sigma \pi \xi \quad (1.15)$$

by replacing $D_s\theta$ with ξ . Subsequently using this identity again we can write

$$\alpha(\theta) = \frac{4G}{c^2} \frac{D_{ds}}{D_s D_d} \frac{\Sigma \pi \xi^2}{\theta} \quad (1.16)$$

and finally using $M(\theta) = \Sigma \pi \xi^2$ we obtain

$$\alpha(\theta) = \frac{4G}{c^2} \frac{D_{ds}}{D_s D_d} \frac{M(\theta)}{\theta} \quad (1.17)$$

Substituting this in Eqn.1.10 for $\beta = 0$ we get the **Einstein radius** θ_E :

$$\theta_E = \sqrt{\frac{4GM(\theta_E)}{c^2} \frac{D_{ds}}{D_s D_d}}. \quad (1.18)$$

where M is the mass within an angular radius θ . The power of this equation lies in the fact that if we know the Einstein radius we can already infer something about the mass of the lensing galaxy within this radius if we know the distances or vice versa if we know the mass within the Einstein radius we can infer information about the distances between the objects.

A different way to derive the lensing equation is based on Fermat's principle. This principle states that light will travel along a path of stationary optical path length with respect to small deviations from this path, implying practically the same travel time for those paths. In the context of gravitational lensing this is expressed with the **Fermat potential**

$$\tau(\theta, \beta) = \underbrace{\frac{1}{2}(\theta - \beta)^2}_{\text{Geometric Delay}} - \underbrace{\psi(\theta)}_{\text{Shapiro Delay}} \quad (1.19)$$

which in physical units can be seen as a *time delay surface*

$$t(\theta, \beta) = \frac{1 + z_d}{c} \frac{1}{2} (\theta - \beta)^2 - \psi(\theta) \quad (1.20)$$

where z_d is the deflector redshift and ψ is the *deflection potential* defined by $\nabla^2 \psi = 2\kappa$. The time delay (with respect to the unlensed source) consists of two components:

- **Geometric Delay:** caused by the extra geometrical path length with respect to an unlensed source.
- **Shapiro Delay:** caused by the extra travel time due to curvature of space-time. The gravitational potential can be seen as introducing a refractive index, effectively "slowing down" the light.

The lensing equation now follows from the setting the gradient of this Fermat potential equal to zero

$$\nabla \tau = 0 \quad (1.21)$$

and hence images form when the travel time is either a minimum, maximum or saddle point of the time delay surface.

Lensing Theory - Magnification, Caustics and Critical Curves

Strong gravitational lensing does not only produce multiple images, it also distorts and magnifies the object. The distortion can be represented as a transformation from the source plane β to the image plane θ with the Jacobian

$$\begin{aligned} A(\theta) &= \frac{\partial \beta}{\partial \theta} \\ &= \delta_{ij} - \frac{\partial^2 \psi(\theta)}{\partial \theta_i \partial \theta_j} \end{aligned} \quad (1.22)$$

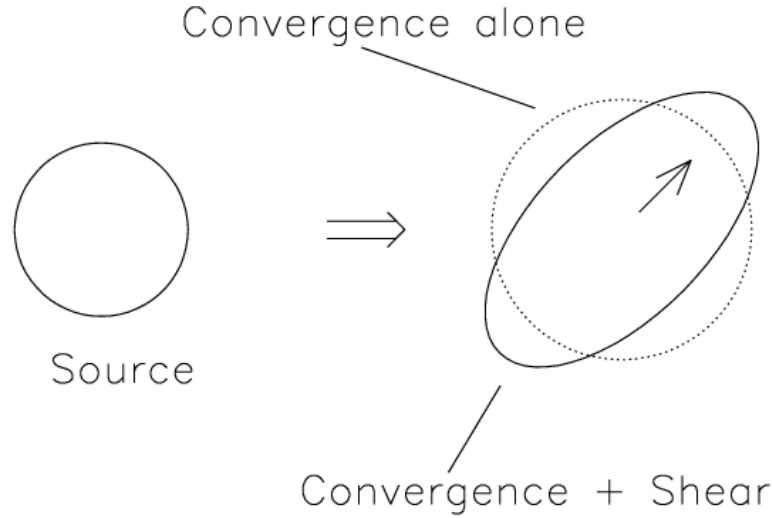


FIGURE 1.6: A simple illustration demonstrating the effects convergence and shear have on a circular object being lensed. Image from [Dekel and Ostriker 1999](#).

In matrix form this is a 2×2 symmetric matrix:

$$A = \begin{pmatrix} 1 - \kappa - \gamma_1 & -\gamma_2 \\ -\gamma_2 & 1 - \kappa + \gamma_1 \end{pmatrix} \quad (1.23)$$

where κ is again the convergence and γ_1, γ_2 are components of the **shear** $\gamma^2 = \gamma_1^2 + \gamma_2^2$. Starting from a circular object the convergence will make it appear larger or smaller. The shear will flatten and rotate the object. This effect is illustrated in Fig. 1.6.

The inverse of $A(\theta)$ maps the image plane θ to the source plane β and is called the **magnification matrix** $M(\theta)$ given by

$$\begin{aligned} M(\theta) &\equiv A^{-1}(\theta) \\ &= \frac{\partial \theta}{\partial \beta}. \end{aligned} \quad (1.24)$$

The magnification is given by the determinant of this matrix:

$$\mu = \frac{1}{(1 - \kappa)^2 - \gamma^2} \quad (1.25)$$

obtained by $\det M = \det A^{-1} = \frac{1}{\det A}$. In the case that $(1 - \kappa)^2 - \gamma^2 \rightarrow 0$ we have $\mu \rightarrow \infty$. This corresponds to similar transition regions as we had earlier for $\kappa = 1$. When crossing these lines of infinite magnification, more images are created or destroyed depending on which direction the source moves. The terminology depends on whether one considers these transition lines in the source plane or image

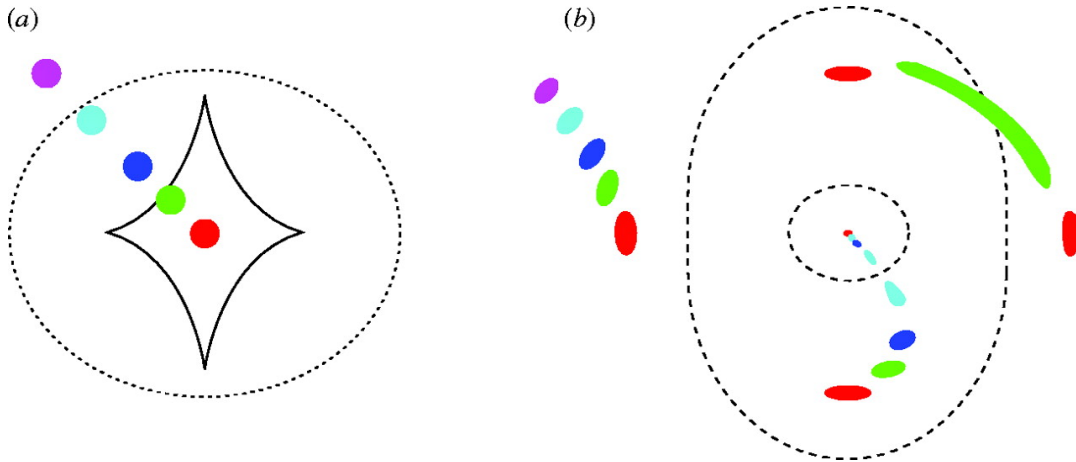


FIGURE 1.7: An illustration from Ellis 2010 demonstrating critical curves and caustics. Depending on the position of the source (different color circles) in the source plane (a) different configurations of images are produced in the image plane (b).

plane. In the source plane they are called **caustics** while in the image plane they are called **critical curves**. Figure 1.7 gives an example of an elliptical lens. The smooth sections of the caustics are called *folds* and the sharply pointed regions are called *cusps*.

1.3 MM18423+5938

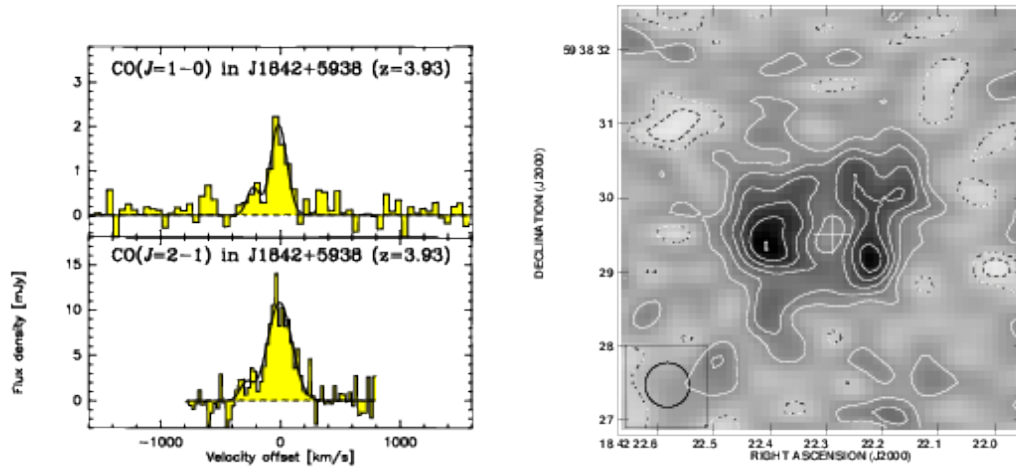
MM18423+5938 (hereafter just MM18423) is a DSFG discovered by Lestrade et al. 2009 during a study of debris disks around dwarf stars. They published the discovery the year after in Lestrade et al. 2010 where they also derive a spectroscopic redshift of $z = 3.9296 \pm 0.00013$ using CO(6-5) and CO(4-3) emission lines. What made this object interesting is that it was reported as the brightest DSFG in the North at the time. Since then two more papers have been published on this object by Lestrade et al. 2011 and McKean et al. 2011. Using SED modeling Lestrade et al. 2010 found a FIR luminosity of $4.8 \times 10^{14} L_{\odot}$ as well as an extreme star formation rate of $8.3 \times 10^4 M_{\odot} \text{ yr}^{-1}$. Due to this, they propose the system is probably gravitationally lensed. Follow up observations were made with the WSRT at 1.4 GHz by McKean et al. 2011. They find a FIR luminosity of $5.6_{-2.4}^{+4.1} \times 10^{13} L_{\odot}$ and a star formation rate of $9.4_{-4.9}^{+7.4} \times 10^3 M_{\odot} \text{ yr}^{-1} \mu^{-1}$. An order of magnitude lower than Lestrade et al. 2010, but still high they conclude given the low excitation of the gas implied by measurements of CO.

The mismatch between the measurements by an order of magnitude can be attributed to the lack of photometric datapoints preventing a reliable fit and analysis of MM18423's SED. In 2011 Lestrade et al. published another paper in which they revise their luminosity estimate to be in the range $2 \times 10^{13} - 3 \times 10^{14} L_{\odot}$ uncorrected for lensing. A first estimate of the magnification is made using CO(2-1) emission giving $\mu \sim 12$. Currently the status quo for MM18423 is that it is a bright object with L_{FIR} exceeding $10^{12} L_{\odot}$ implying it is a dusty, (extreme) starbursting galaxy with a star formation rate likely of the order of $10^3 - 10^4 M_{\odot} \text{ yr}^{-1}$; a high-redshift analogue of local ULIRGS.

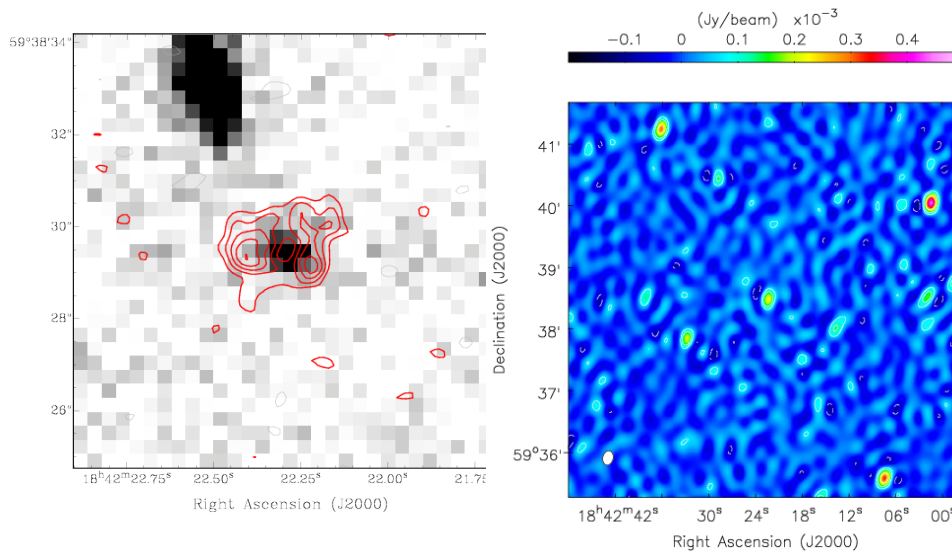
In Tab. 1.2 the current measurements available for MM18423 are summarized. In Fig. 1.8 a summary of available imaging and spectroscopic data is shown.

Parameter	Value	Authors
<i>Photometry</i>		
3 mm	$2^{+2.0}_{-1.5}$ mJy	Lestrade et al. 2010
2 mm	9 ± 3 mJy	Lestrade et al. 2010
1.2 mm	30 ± 2 mJy	Lestrade et al. 2010
100 μm	< 600 mJy	Lestrade et al. 2010
60 μm	< 100 mJy	Lestrade et al. 2010
24 μm	< 0.6 mJy	Lestrade et al. 2010
1.4 GHz	217 ± 37 mJy	McKean et al. 2011
<i>Line Emission</i>		
CO(1-0) ^a	2.67 ± 0.44 mJy	Lestrade et al. 2011
CO(2-1) ^a	12.75 ± 1.53 mJy	Lestrade et al. 2011
CO(4-3)	26.7 ± 3 mJy	Lestrade et al. 2010
CO(6-5)	6.4 ± 1 mJy	Lestrade et al. 2010
CO(7-6)	4.2 ± 0.9 mJy	Lestrade et al. 2010
CI(³ P ₂ – ³ P ₀)	1.9 ± 0.6 mJy	Lestrade et al. 2010
CI(³ P ₂ – ³ P ₁)	4.2 ± 1 mJy	Lestrade et al. 2010
<i>SED Parameters</i>		
L_{FIR}	$2 \times 10^{13} - 3 \times 10^{14} L_{\odot} \mu^{-1}$	Lestrade et al. 2011
	$5.6^{+4.1}_{-2.4} \times 10^{13} L_{\odot} \mu^{-1}$	McKean et al. 2011
SFR	$3300 - 22000 M_{\odot} \text{yr}^{-1} \mu^{-1}$	Lestrade et al. 2011
	$9.4^{+7.4}_{-4.9} \times 10^3 M_{\odot} \text{yr}^{-1} \mu^{-1}$	McKean et al. 2011
T_d	45 K	Lestrade et al. 2010
	24^{+7}_{-5} K	McKean et al. 2011

TABLE 1.2: A summary of currently known photometry, line emission and SED related parameters for MM18423. *a*: They identify two components to the line. The reported flux density here is those components added together and the uncertainty is obtained through error propagation.



A. Lestrade et al. 2011



B. Lestrade et al. 2011

C. McKean et al. 2011

FIGURE 1.8: A collection of plots from previous works on MM18423. *Top*: the spectra of the CO(1-0) and the CO(2-1) emission lines obtained from C-array VLA data, at 26 km s^{-1} resolution. To the right of it is their map of the FWHM of the line using natural weighting. *Bottom left*: the contours of the CO(2-1) emission as shown on the grayscale map overlaid on an optical image of the system. *Bottom right*: A 1.4 GHz WSRT map of MM18423+5938 made by McKean et al. 2011.

1.4 Thesis Outline

The work in this thesis will be a continuation of the previous studies. Our goal was to accomplish the following:

- Add new data points to the SED: a 5 GHz measurement with the EVLA and three measurements from SPIRE on the Herschel Space Observatory at 250, 350 and 500 μm .
- Confirm the dust temperature found by earlier studies or further constrain the plausible range of values.
- Study the molecular gas at more scales: EVLA D-array and B-array observations of both the CO(1-0) and CO(2-1) transitions are used.

In Chapter 2 the details of the observations are presented along with the data reduction strategies used. As data from different telescopes was used this chapter contains sections dedicated to the data reduction process specific to those telescopes. In Chapter 3 the lens plane analysis of the measurements is presented. The lensed values for the various luminosities, star formation rate and gas mass are presented along with a first interpretation of the observed configuration of the lensed images. In Chapter 4 these values are interpreted, followed by a conclusion in Chapter 5.

Chapter 2

Observations and Data Reduction

DATA reduction varies from telescope to telescope. As each instrument or system records data in its own way, different reduction and calibration strategies are needed. For this project, data from the Hubble Space Telescope (HST), the Very Large Array (VLA) and the Herschel Space Observatory were used. These observations probe the NIR, radio and FIR/sub-mm emission of MM18423, respectively. This chapter will describe the observations and data reduction process for each telescope individually. First the details of the observations are summarized, followed by the data reduction process.

2.1 HST

2.1.1 Observations

The HST has been operational for 26 years and it is still a widely used telescope. Current instruments on the telescope are STIS, NICMOS, ACS, COS and WFC3 allowing the HST to observe from the near infrared up to the ultraviolet. For the observations of MM18423 WFC3 was used. The WFC3 camera can operate in two modes: UV and IR. In Tab. 2.1 the specifications for each mode are summarized, as listed in Dressel 2016. The temperature here refers to the operational temperature. The HST observed MM18423 on September 20th 2011 (GO:12480; PI Carilli 2011) from 05:58:18 to 06:49:24 for a total observing time of 51m06s. Multiple exposures were taken using a dither pattern to obtain a better sampling of the point spread

TABLE 2.1: WFC3 UV/VIS and IR instrument specifications.

UV/VIS			IR		
Pixels		2051 × 4096	Pixels		1024 × 1024
Pixel Size	μm	15 × 15	Pixel Size	μm	18 × 18
Plate Scale	["/pixel]	0.040	Plate Scale	["/pixel]	0.13
Field of View	["]	162 × 162	Field of View	["]	136 × 123
Wavelengths	[nm]	200 - 1000	Wavelengths	[nm]	800 - 1700
Temperature	[K]	190	Temperature	[K]	145

function (PSF). The technique of dithering will be explained in the next section. For this observation WFC3 was operating in IR mode using the *F110W* wideband filter, also known as *Wide YJ*. This filter has a pivot wavelength of $\lambda_p = 1153.4$ nm and a width of $\Delta\lambda = 443.0$ nm. Multiple exposures were taken with four pointings. At each pointing two exposures of 349.233s were made, giving a total exposure time of 698.465s per pointing. With four pointings in total, the total integration time was 2793.862 s. Since we are looking at a high-redshift source we are not actually probing the infrared emission. The radiation we receive is redshifted by

$$\lambda_{\text{obs}} = \frac{\lambda_{\text{em}}}{1+z} \quad (2.1)$$

where λ_{obs} is the observed wavelength and λ_{em} the wavelength emitted by the source. At a redshift of $z \cong 4$ this means we are looking at 222 nm rest-frame emission, i.e. the UV emission. The presence of UV emission is an indicator that hot, usually young stars (O and B type) are present and hence can be an indicator of star formation.

Figure 2.1 shows the eight individual exposures all with the same brightness scale. During the reduction we noticed a decrease in background brightness throughout subsequent exposures. These effects are most likely caused by either Helium I emission or other effects of the Earth's atmosphere. At the beginning of an orbit the telescope is still picking up some emission from the upper part of the atmosphere. As the observation progresses the telescope will look away from the Earth and hence the effect becomes less.¹

The value of the background is taken from the MDRIZSKY keyword in the FITS file. The values are listed in Tab. 2.2 where the decreasing background is quantified with measurements made by the AstroDrizzle software during the initial pipeline reduction done by the system. The raw data from the telescope is not directly usable by astronomers. At the STScI a preliminary reduction is done to provide the end user with calibrated FITS files. In the case of WFC3 data, it is not immediately processed when it arrives, but rather when the data is requested for retrieval. This is called *on-the-fly reprocessing* (OTFR) and is done by the OPUS pipeline. A schematic overview of this reduction process can be seen in Fig. 2.2. The OTFR pipeline consists of three main steps, which will be shortly explained below.

TABLE 2.2: AstroDrizzle Sky Values

Observation	Sky Value [cps]
05:58:18	2.45
06:04:28	1.75
06:11:21	1.30
06:17:31	1.06
06:24:22	0.83
06:30:32	0.66
06:37:25	0.62
06:43:35	0.65

OPUS The *Operational Pipeline Unified System* converts the raw packets from the telescope into images and applies basic calibrations. In the end this results in a flat fielded, calibrated image. For WFC3 data the calibration is carried out by *calwf3*.

Calwf3 According to Dressel 2016 the following calibrations and corrections are applied when *calwf3* is run:

¹Concluded through personal communication with the STScI.

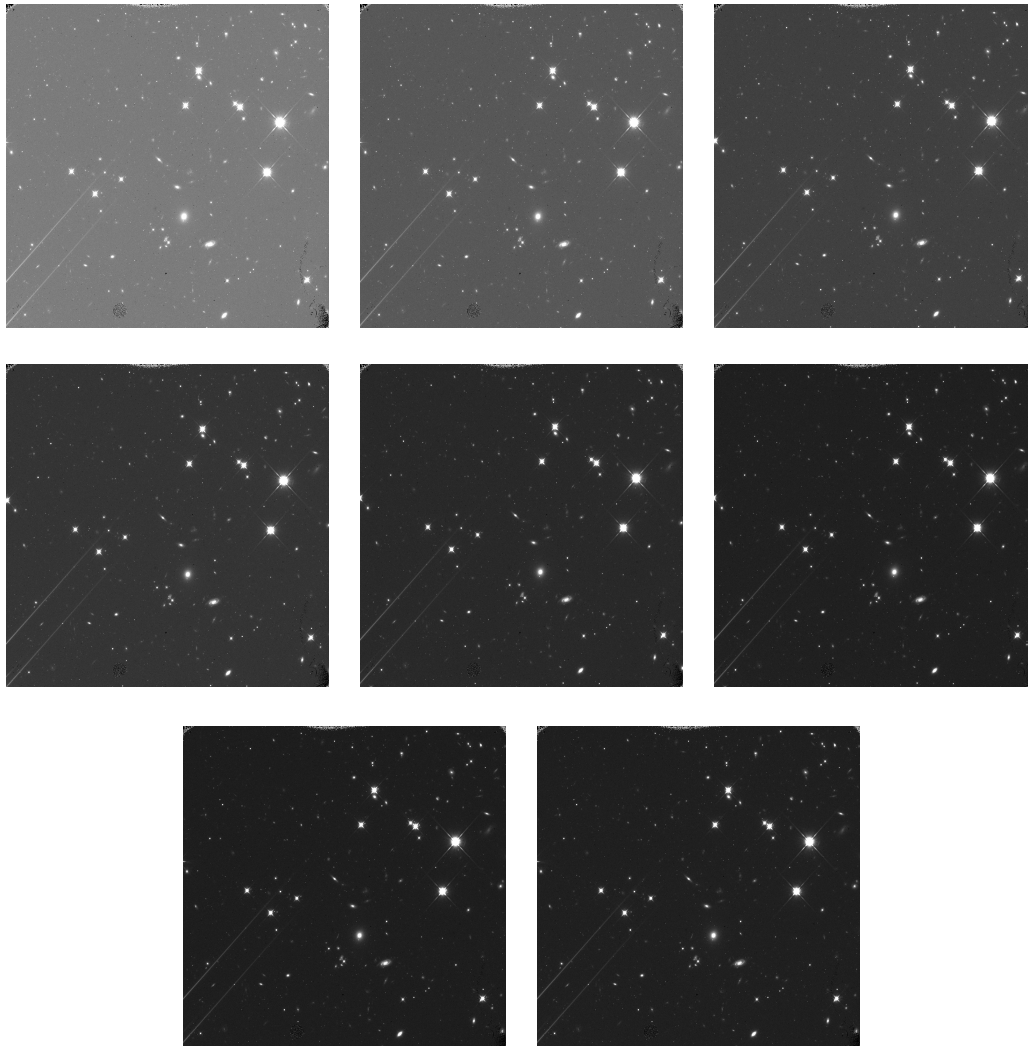


FIGURE 2.1: The eight flat fielded images of the entire observed field. Time is increasing from left to right. The intensity scale is the same for all eight images, showing that the first observations have a brighter background than the later observations. This is due to either Helium I emission or the Earth's limb.

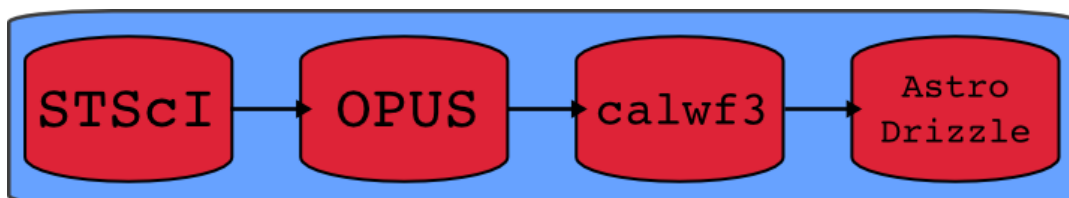


FIGURE 2.2: A schematic overview of the OTFR pipeline. The acronyms respectively mean: *Space Telescope Science Institute (STScI)*; *Operational Pipeline Unified System (OPUS)*; *Calibrate WFC3 (calwf3)*.

- Bad pixels are flagged.
- Changes in the bias level are tracked and removed by so called *reference pixel subtraction*.
- Initial readout is removed from all subsequent exposures to remove spatial bias structure. This is called *zero-read subtraction*
- Through *dark current subtraction* the noise arising from thermally excited electrons is removed.
- Non-linearity is corrected for by flagging saturated pixels defined by being more than 5% off from linear.
- Flat field corrections are applied and gain calibration is done.
- Through *up-the-ramp fitting* the final value of every pixel is determined and effects due to cosmic rays are removed.
- Photometric calibration is applied.

AstroDrizzle The final step is to produce a quick-look image for initial inspection. Since there is likely a better set of parameters for a specific data set, a better quality image can be obtained by redoing this step with optimal parameters.

2.1.2 Dithering

A complete and in-depth discussion of dithering can be found in the HST Dither Handbook by [Koekemoer 2002](#). This section will introduce the concept of dithering and why it is important.

During an observation there are several ways in which information can be lost. This can be due to natural phenomena such as cosmic rays or due to instrumental effects such as hot pixels or bad columns. Occurrences like cosmic rays can be planned for in advance e.g. by taking multiple exposures, as it is unlikely that two or more images will have a cosmic ray at the same position. Instrumental effects are more difficult to deal with, because they are always present. Another reason for information loss is not sampling the PSF correctly or rather sampling it sub-optimally. Ideally one would want the FWHM of the PSF to be sampled by a little over two pixels (Nyquist sampling). Sampling with less pixels means a loss of spatial information. Whether or not this is an issue depends on the FWHM of the telescope's PSF and the detector pixel size. In the case of WFC3 the pixel size is of the same order as the FWHM, so the issue is present. As it turns out, we can counter these effects up to a certain extent by taking multiple exposures in a specific pattern and then combining these images. Doing these patterned observations is called *dithering* and the algorithm to combine the images is the *drizzle* algorithm.

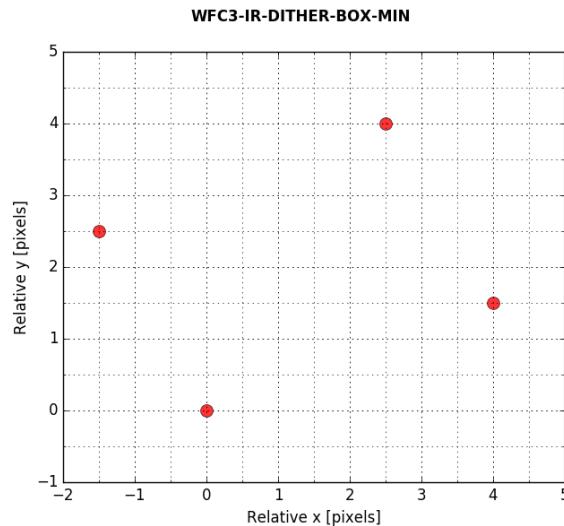
In summary there are thus two main reasons to use dithering:

1. removal of bad pixels in the image.
2. recovery of spatial information by better sampling of the PSF.

Bad pixel removal To remove bad pixels, exposures are separated by an integer number of pixels. This way light from the object of interest falls on a different pixel. Doing this multiple times allows the observer to correct for the bad pixel by using the other values at the other pixels and carrying out a median fit.

TABLE 2.3: DITHER PATTERN PROPERTIES.

Pattern Type		WFC3-IR-DITHER-BOX-MIN
Number of Points		4
Point Spacing	[arcsec]	1.716
Line Spacing	[arcsec]	1.095
Pattern Orientation	[deg]	18.528
Angle between Sides	[deg]	74.653

FIGURE 2.3: The dither pattern used for this observation. Adapted from [Dahlen et al. 2010](#).

PSF Sampling To improve the sampling of the PSF the exposures are shifted with respect to each other by a fraction of a pixel. This is called *sub-pixel dithering*. Consider a half-pixel shift. By doing this effectively a new pixel is created from two touching halves of neighbouring pixels and therefore resolution is increased, at the expense, however, of having correlated noise.

The effects can be combined by doing a full pixel shift with a sub-pixel shift. For the observation of MM18423 the WFC3-IR-DITHER-BOX-MIN pattern was used. The pattern is shown in Fig. 2.3. Its properties for this observation are summarized in Tab. 2.3. The point and line spacing are three times the default values [[Dahlen et al. 2010](#)].

2.1.3 Combining Images with AstroDrizzle

Image Reconstruction

The image quality of an exposure is degraded because of two reasons. First is the fact that a telescope has a PSF, meaning it is not equally sensitive to signals coming from different directions. The second reason has to do with the fact that CCDs are not perfect. A pixel on the CCD can be thought of as having a PSF that maps signals to the *physical pixel* (PP). However, due to charge diffusion the response of a single pixel can extend beyond its physical size, called the *electronic pixel* (EP). This effect is characterized by the pixel response function or PRF. An observation is thus essentially a convolution of the signal with subsequent response functions [[Fruchter](#)

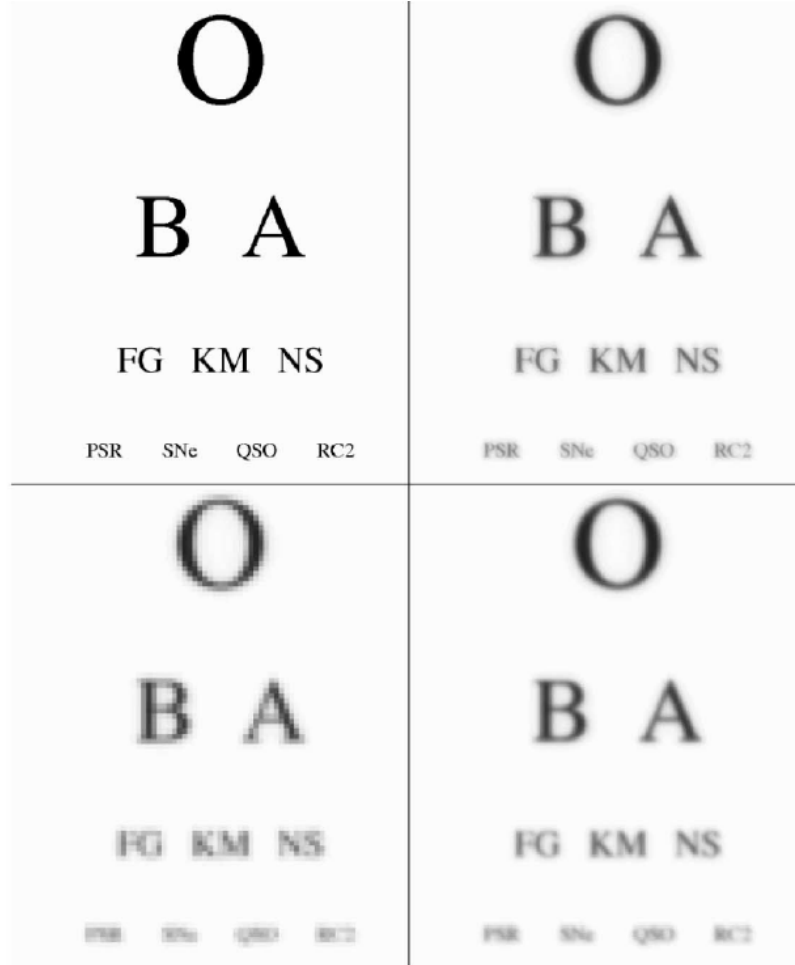


FIGURE 2.4: *Top left*: original image. *Top right*: after convolution with HST and WFPC2 optics. *Bottom left*: after convolution with the physical pixel. *Bottom right*: reconstructed image from a 3x3 grid of dithered “observations” using interlacing. Image credit: [Gonzaga 2012](#).

and Hook 2002; Dressel 2016]. First an observed image,

$$I_O = \text{signal} \otimes \text{PSF} \quad (2.2)$$

is produced by the PSF. Next the detector produces the detected image

$$I_D = \text{signal} \otimes \text{PSF} \otimes \text{PRF} \quad (2.3)$$

or

$$I_D = \text{signal} \otimes \text{PSF} \otimes (\text{EP or PP or (EP+PP)}) \quad (2.4)$$

by convolving I_O with the pixel response function. The biggest loss of quality at this step comes from the convolution with the physical pixel PP as seen in the bottom left of Fig. 2.4. Two common techniques for reconstructing an image are interlacing and shift-and-add. In the case of a perfect dither with uniform sub-pixel offsets and no rotation or distortion, interlacing can be used. The pixels of the individual images are inserted in an alternating pattern depending on the offset of each image. This technique is illustrated in Fig. 2.5.

In reality however, the offsets are never perfect, because there are errors in the telescope pointing for example. Therefore, it is often not possible to just use pure

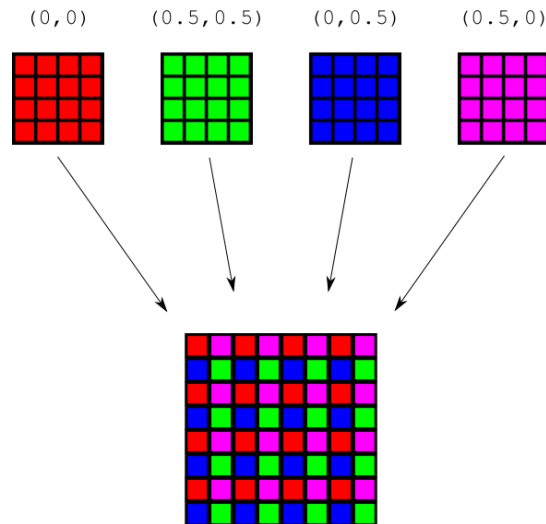


FIGURE 2.5: Illustration depicting the interlacing method to reconstruct images. Pixels from each image are used in an alternating pattern on the final image. The numbers above the gridded squares denote the offset w.r.t. some point.

interlacing. A different method that overcomes these issues is the shift-and-add technique. This however requires convolution with the physical pixel again, which is, as we saw earlier, something to be avoided if possible. The drizzle algorithm tries to combine the best of both methods [Fruchter and Hook 2002; Gonzaga 2012].

Drizzle - The Method

Drizzling is a technique first implemented in the reduction of the Hubble Deep Field (HDF) data as the camera used to take exposures (WFPC2) undersampled the PSF, causing the resolution to decrease. In order to reclaim part of this resolution, multiple images were drizzled together. Drizzle also corrects for the geometric distortion of the images due to the light not falling perpendicular on the camera.

To reduce the data, the DrizzlePac software² was used. A number of parameters can be adjusted, but for our purposes we left most of the settings at their default values. Optimizing the drizzle process depends mainly on two parameters: *final_pixfrac* and *final_scale* (from here on referred to as just *pixfrac* and *scale*). The idea of drizzling is illustrated in Fig. 2.6 [Gonzaga 2012]. First the input pixels (shown in red) are shrunk to a smaller size (shown in blue). This step is to reduce the effect of convoluting the signal with the physical pixel which was shown in Fig. 2.4. These shrunk pixels are then corrected for any distortions, shifts and rotations before being “drizzled” down onto the output grid. Care should be taken, however, that the pixel is not shrunk too much. If they become too small then the output grid will not be completely covered and hence there will be gaps in the output image. The main game of drizzling is thus to find the optimal balance between making the pixels small enough such that convolution with them does not degrade the image more than necessary and keeping them large enough to cover the output grid uniformly [Fruchter and Hook 2002].

²<http://drizzlepac.stsci.edu/>

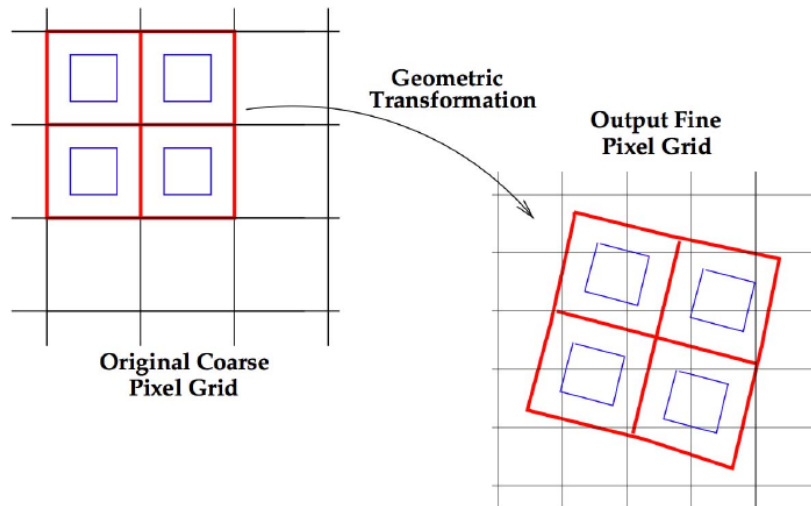


FIGURE 2.6: Illustration of the drizzling process. The original pixels (red) are first shrunk to a smaller size (blue), corrected for any distortions and then “drizzled” down onto a finer output grid. Image credit: [Gonzaga 2012](#).

Drizzle - Applied to the Data

As mentioned above, the ideal sampling of the PSF is having slightly over two pixels in the FWHM. Along with the consequences of choosing the pixel scale too small mentioned above, we first try to optimize for the scale parameter *final_scale*. Since the PSF is sampled by the pixels, changes in their scale will be reflected by changes in the PSF. For the first optimization we kept the *pixfrac* parameter constant at a value of 1.0 and we varied the scale parameter. The preference to sample the PSF properly leads to an initial value of the scale parameter of half the native pixels scale. For the WFC3 camera this means an initial guess of $final_scale = 0.065'' \text{ pixel}^{-1}$. We therefore explored a small range around this value from 0.55 – 0.75 and two extreme values to represent oversampling and undersampling the PSF represented by 0.01 and $0.13'' \text{ pixel}^{-1}$, respectively. To compare how this changes the PSF, a star in the vicinity of the source was cut out and imaged for each attempt. Since stars are point sources their shape should be a good indicator of the PSF of the telescope.

Figure 2.7 shows the explored range of values around the native plate scale. We found the most suitable scale to be $0.060'' \text{ pixel}^{-1}$ as this was the lowest value with a reasonable smooth PSF while sampling the PSF at least twice (2.16 times in this case). In Fig. 2.8, two extreme examples of sampling are shown: highly oversampling the PSF with a scale significantly smaller than the native plate scale and undersampling with a scale that is equal to the native plate scale. In the first case the contours become blocky and the central region starts to become more square. If the scale is set too small, the PSF will eventually start to resemble the used dither pattern [[Koekemoer 2002](#)].

Now that the scale parameter is optimized we keep it fixed at its optimal value and start optimizing the *pixfrac* parameter. According to [Gonzaga 2012](#) a good statistic for this parameter is the ratio between the standard deviation σ and the median pixel value in a region of the *weight image* corresponding to the region of interest on the sky. This ratio should not exceed 0.2 and the *pixfrac* value should also not be smaller than the chosen scale. We used DS9 to measure the median and standard deviation in the region of interest and from these values we calculated the statistic. For *pixfrac* values from 0.1 up to 1.0 were chosen, separated by steps of 0.1. Figure 2.9 shows the

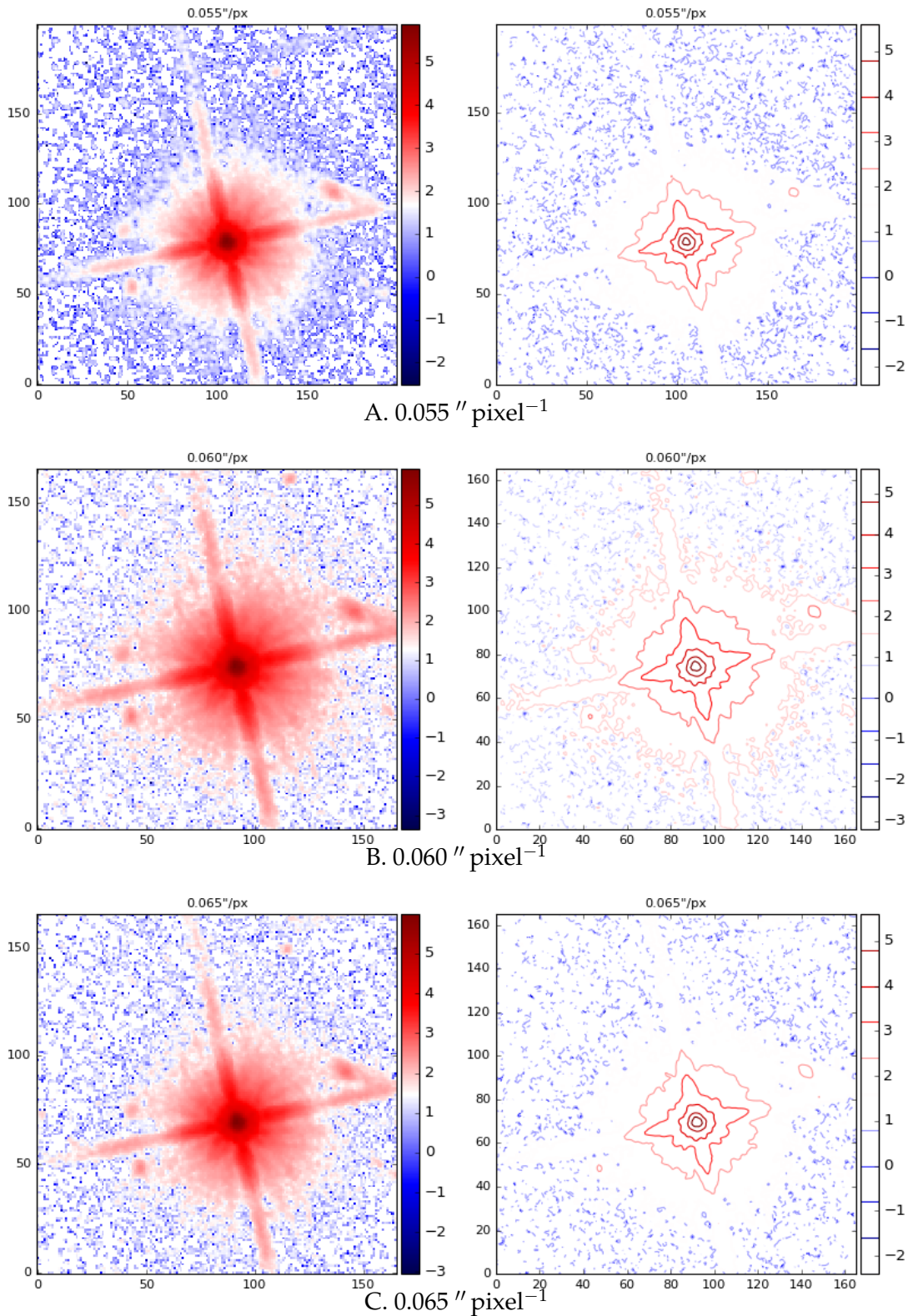


FIGURE 2.7: A comparison of PSFs resulting from different choices for the *final_scale* parameter. The displayed values are 0.55, 0.60, 0.65, 0.70 and 0.75'' pixel⁻¹, respectively. The pixel values represent counts, but the (color) scale here has no real meaning other than to highlight differences between the images.

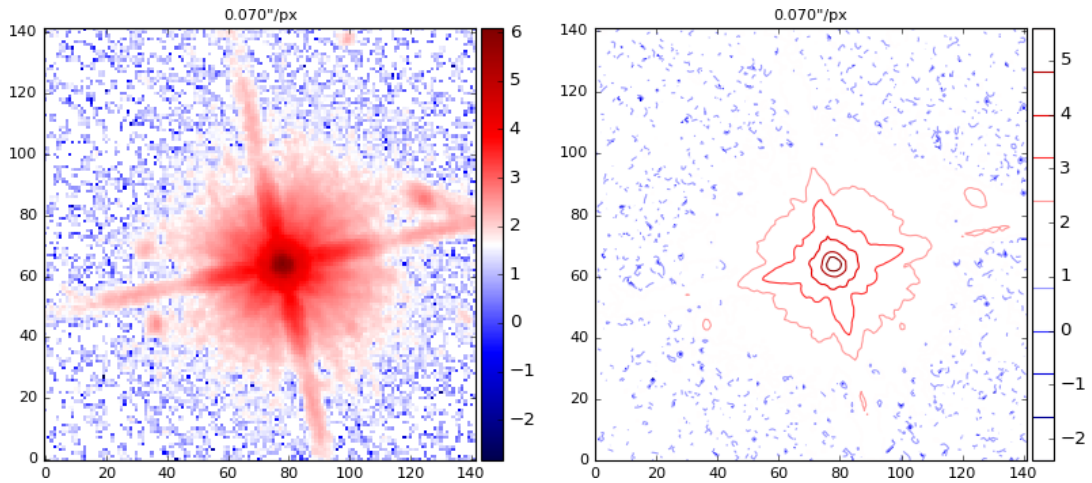
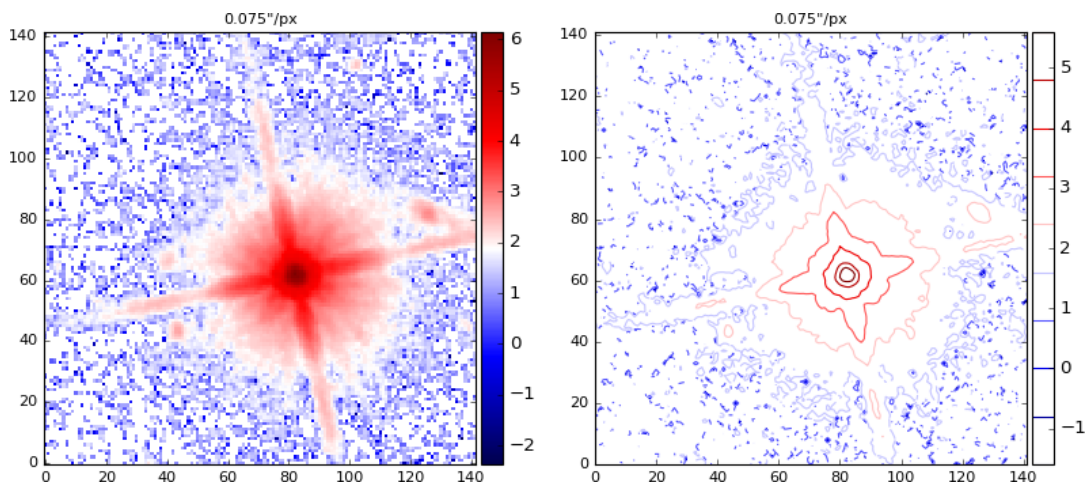
D. $0.070'' \text{ pixel}^{-1}$ E. $0.075'' \text{ pixel}^{-1}$

FIGURE 2.7: A comparison of PSFs resulting from different choices for the *final_scale* parameter. The displayed values are 0.55, 0.60, 0.65, 0.70 and 0.75'' pixel⁻¹, respectively. The pixel values represent counts, but the (color) scale here has no real meaning other than to highlight differences between the images.

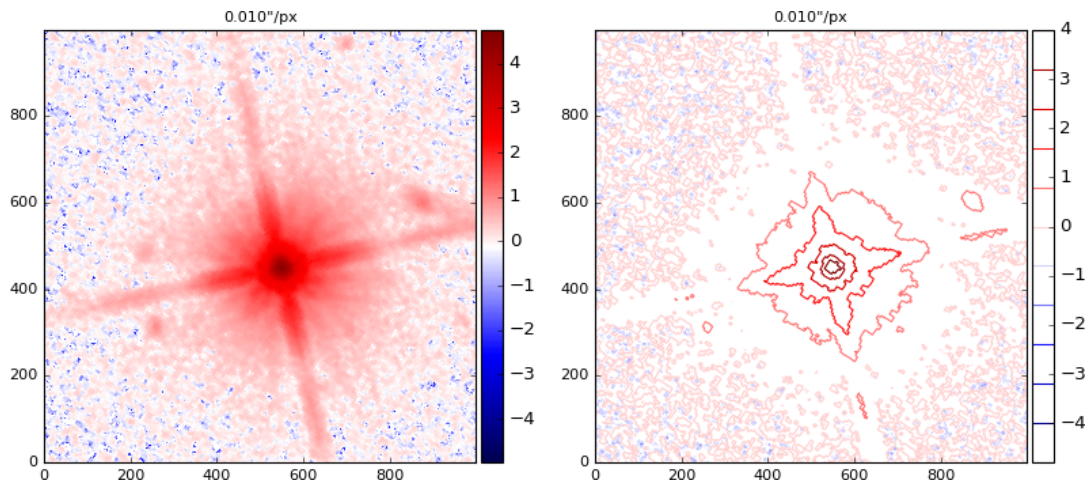
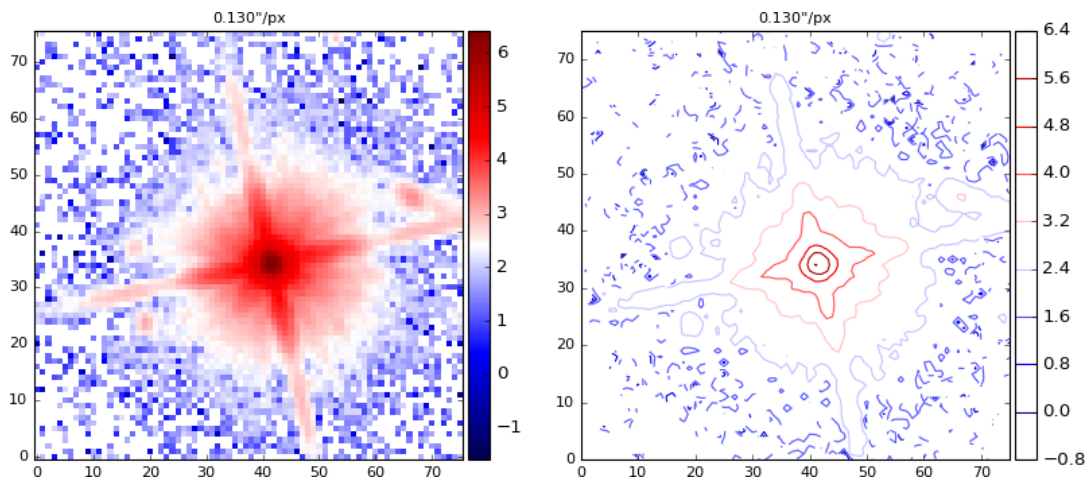
A. 0.010 " pixel⁻¹B. 0.13 " pixel⁻¹

FIGURE 2.8: Two extreme cases: oversampling (*top*) with a scale of 0.01 " pixel⁻¹ and undersampling (*bottom*) with a scale of 0.13 " pixel⁻¹, the native WFC3 plate scale.

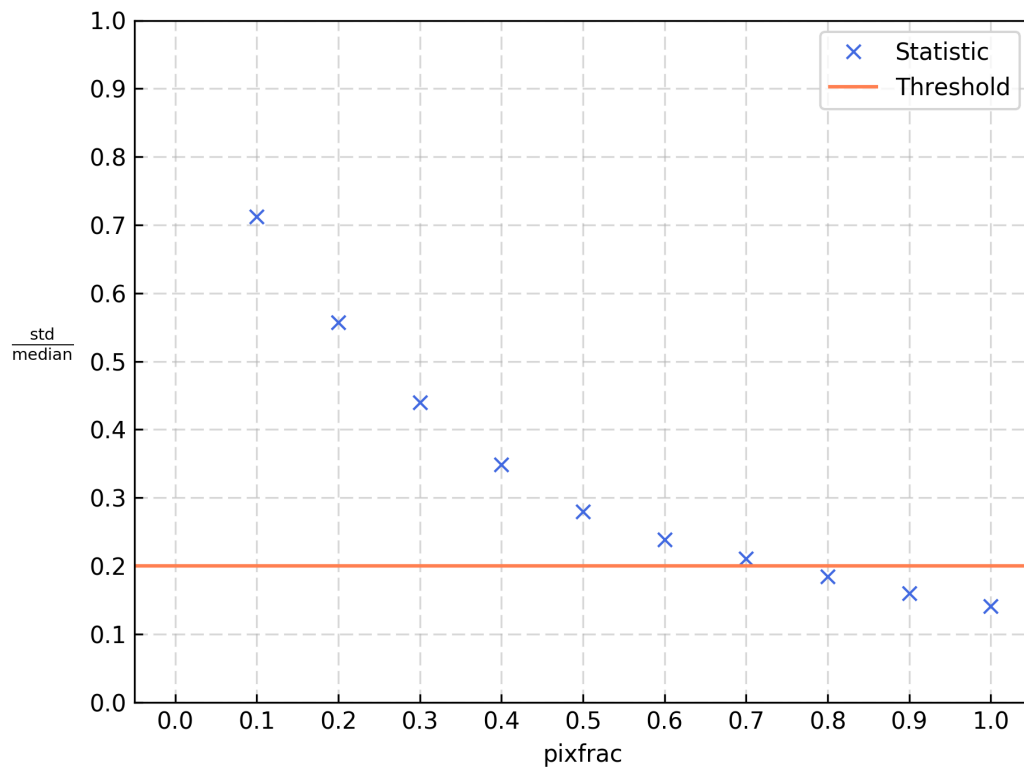


FIGURE 2.9: The standard deviation divided by the median pixel value of the weight image in the region of interest as a statistic for the pixfrac parameter. The threshold value of 0.2 is indicated by the horizontal red line. The calculated ratios are depicted by the blue crosses. From this we can conclude that a pixfrac of 0.8 is the optimum value.

pixfrac values with their corresponding σ -over-median value. To show the difference the pixfrac parameter can make, Fig. 2.10 shows a comparison between a pixfrac of 0.1 (meaning the pixels are excessively shrunk) and a pixfrac of 1.0 (no shrinking at all). Shrinking the pixels too much causes the output image to no longer be covered adequately and hence pixels without data will start to appear in the image. Based on these results, we found an optimal value of 0.8 for the *final_pixfrac* parameter. Now that we have optimized both parameters the drizzling process was run one final time with these values to produce the final image. The result including a zoom in of the source area, is shown in Fig. 2.11 with north being up and east pointing to the left.

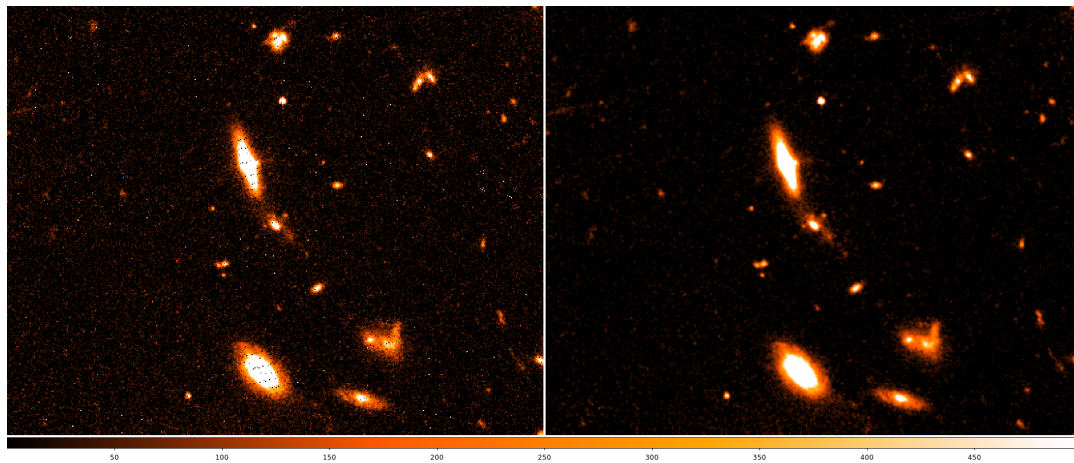


FIGURE 2.10: A comparison between a pixfrac of 0.1 (*left*) and a pixfrac of 1.0 (*right*). The black dots in the left image are pixels where no data is present due to the drizzled pixels being too small to sufficiently cover the output image.

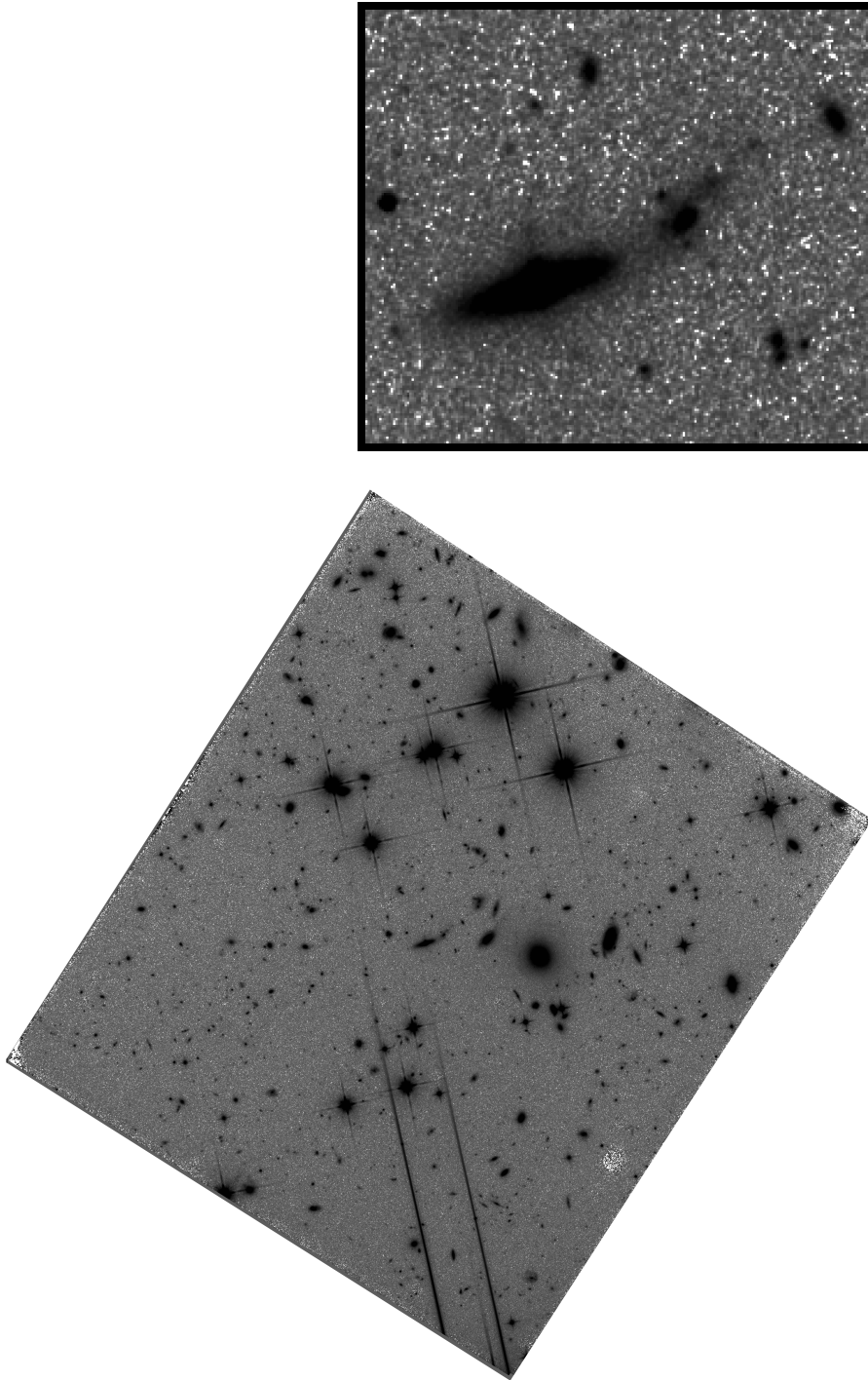


FIGURE 2.11: The final image produced by the drizzling process. A $final_scale$ of $0.06'' \text{ pixel}^{-1}$ and a $final_pixfrac$ of 0.8 were used to produce this image. North is up and east is to the left.

2.1.4 Fitting Objects with Galfit

In the exposure, the lensing galaxy is still present along with other galaxies in the field. The light from these objects will contaminate the image, making it harder to tell whether emission is coming from the source or from a nearby object. In an attempt to isolate the source we used the `GALFIT` software which allows us to fit and then subtract objects in the field with a variety of profiles, for example Gaussians, exponential profiles or Sérsic profiles. For this source there are two main sources of “light pollution” in the field: then lens itself and what appears to be an edge-on disk galaxy close by. Since we are only interested in a source at the center of the image, it is not necessary to keep the entire image. We therefore made a cutout containing only the source and a few sources around it. Figure 2.12 shows this cutout. Ultimately, we want to remove all sources except the source, but the process itself is an iterative procedure. We fit one component and look at the residuals. Then we either modify the values of a component or add another component to the fit and look at the residuals again. For example, once the fit converges to a correct position we lock these values and move to fit other galaxy parameters. This is repeated until all relevant sources are fitted to appreciable levels.

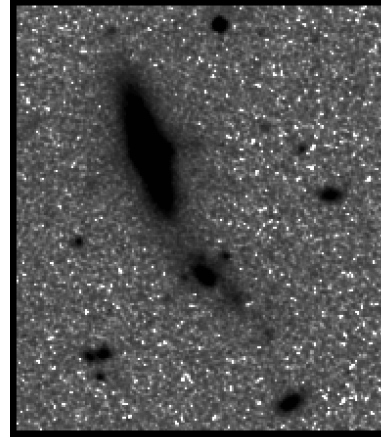


FIGURE 2.12: Isolating the target source is done using a small cutout of the total field. The main source to remove is the large galaxy to the top left of the image center. The blob near the center is the lens.

Two approaches were taken at isolating the source: using a large cutout containing the large galaxy nearby and using a small cutout containing only the target. The latter was chosen, because it turned out that fitting the large galaxy was harder than anticipated. For the first approach we tried to fit the lens galaxy and the large disk galaxy nearby. The initial guesses were Sérsic profiles described by

$$\Sigma(r) = \Sigma_e \exp \left[-\kappa \left(\left(\frac{r}{r_e} \right)^{1/n} - 1 \right) \right] \quad (2.5)$$

as listed in Peng et al. 2002. Free parameters for such a profile are the *total magnitude*, the *effective radius* r_e , the *sérsic exponent* n , the *axis ratio* b/a and the *position angle*. The *pixel surface brightness* at r_e , Σ_e , and the parameter κ are not independent and hence cannot be specified for fitting. Initial values for the parameters were determined based on the image where possible, but are nonetheless somewhat arbitrary. In the end they will not matter significantly, because `GALFIT` will converge to reasonable values through the iterative process described above. The most important difference will be the Sérsic index n . The lensing galaxy is an elliptical, while the nearby galaxy appears to be disk. Therefore, they will get indices of $n = 4$ and $n = 1$ respectively, corresponding to a de Vaucouleurs profile and an exponential profile. Attempts to fit both galaxies were largely unsuccessful. We were unable to get the χ^2/ν below 9.2 and the models did not fit the galaxies in a satisfactory way. The final parameters we settled on are listed in Tab. 2.4.

Closer inspection reveals that the lens galaxy itself does not appear to be a simple elliptical, displaying a slight asymmetry. Fitting a Sérsic profile to it clearly overfits the object, leaving two large black regions around it. The residuals in its center may

Fit Parameter		DISKY GALAXY	LENS GALAXY
Integrated magnitude	mag	21.97	24.25
Effective radius	arcsec	0.35	0.48
Sérsic index		2.00	6.23
Axis ratio		0.15	0.24
Position angle		20.43	44.79

TABLE 2.4: Final fitting parameters for GALFIT using the large cutout region. The resulting χ^2/ν is 9.2, which is readily explained by looking at the residuals in Fig. 2.13.

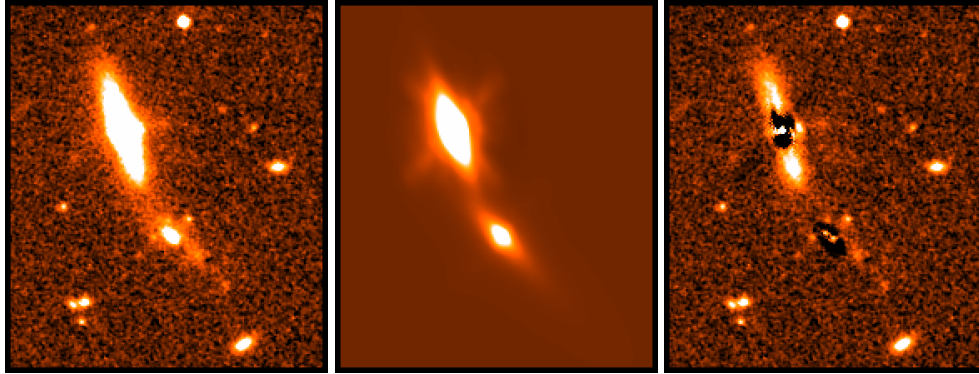


FIGURE 2.13: Results from the attempt to fit the lens and another galaxy in a large cutout containing the source. From left to right: the exposure, the model, the residuals. Both models are not a proper fit as they are clearly oversubtracting the light. There are indications however that this may be due to a more complex structure than these simple models. Attempts to add these however were fruitless.

indicate a second component to it and since the fit appears to have a tendency to go to an extended shape, there might be an extended component present as well. Adding such a component does not lower the χ^2/ν value significantly (0.1 at best) and the image does not display markedly different residuals. Residuals from the large galaxy are indications that this is possibly not a single galaxy, but multiple galaxies on top of each other. Most notably the component to the right of the center and in the lower right end. The field with the corresponding model and residuals are shown in Fig. 2.13.

The second approach was to try and fit only the lens galaxy in a smaller cutout. There will be some contamination due to the light of the large nearby object, which will probably show up as an increased sky background or a higher χ^2 for the fit, as the model cannot account for it. First, we tried a regular Sérsic profile as would be expected for an elliptical galaxy. This resulted in the values listed in Tab. 2.5 which gave a χ^2/ν of 1.10. Figure 2.14 shows the resulting model and residuals.

Fit Parameter		SÉRSIC COMPONENT
Integrated magnitude	mag	24.63
Effective radius	arcsec	0.29
Sérsic index		4.80
Axis ratio		0.14
Position angle		52.54

TABLE 2.5: Results from fitting a single Sérsic profile to the lens galaxy. The resulting χ^2/ν is 1.10.

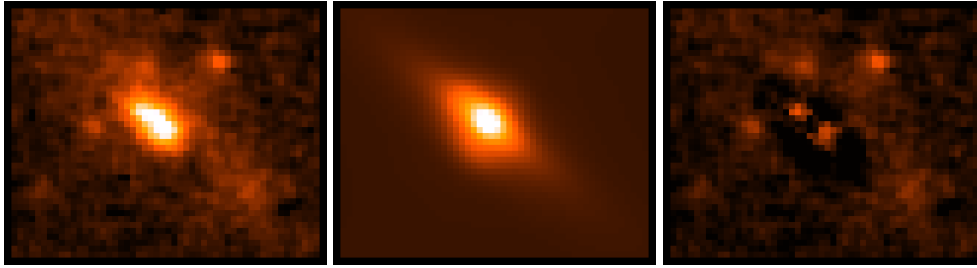


FIGURE 2.14: Results from a single Sérsic profile fit to the lens galaxy. From left to right: the exposure, the model and the residuals. The model tends to an extended galaxy with a large effective radius. This might be an indication for a second more extended, disk-like component.

Looking at the model, we see that it tries to fit an extended light profile to the galaxy. This might be a hint of a second more disk-like component in the galaxy. Adding such a component at the same position and position angle does return a more extended profile with $n = 0.79$ and an effective radius of 208 pixels for this component, corresponding to $12.5''$. Considering this is an elliptical galaxy at redshift 1, this seems unlikely. Therefore I decided to attribute the extended emission due to the excessive background emission present from the large and bright nearby object.

2.2 VLA

Radio astronomy with the VLA covers a range of centimeter wavelengths from 90 cm to 0.7 cm and a 4 m band. In total, the VLA has ten possible spectral windows listed in Tab. 2.6³ which can be used in four array setups listed in Tab. 2.7.

Band	Range [GHz]	Wavelength [cm]	Band	Range [GHz]	Wavelength [cm]
4	0.058-0.084	400	X	8.0 - 12.0	3
P	0.23 - 0.47	90	Ku	12.0 - 18.0	2
L	1.0 - 2.0	20	K	18.0 - 26.5	1.3
S	2.0 - 4.0	13	Ka	26.5 - 40.0	1
C	4.0 - 8.0	6	Q	40.0 - 50.0	0.7

TABLE 2.6: The frequency bands available to the VLA.

³<https://science.nrao.edu/facilities/vla/docs/manuals/oss2016A/performance/bands>

TABLE 2.7: VLA Configurations

Configuration	Min. Baseline [km]	Max. Baseline [km]
A	0.68	36.4
B	0.21	11.1
C	0.035	3.4
D	0.035	1.03

2.2.1 Observations

For this project, data from the VLA archive is used which can be found under the following project codes: 10B-245, 11B-002 and 11B-195. We used observations at 6, 1.3 and 0.7 cm that were made in the C, K and Q bands. The C-band observations (project code 11A-195; PI: McKean) were done to obtain a measurement of the 5 GHz continuum emission and to resolve the radio structure of the source. The K and Q-band observations (project codes 10B-245 and 11B-002; PI: Carilli) were done to probe the CO(1-0) and CO(2-1) molecular emission to study the molecular gas content. These transitions have rest-frame frequencies of $\nu_{\text{r.f.}}^{1-0} = 115.27120$ GHz and $\nu_{\text{r.f.}}^{2-1} = 230.153800$ GHz which are redshifted to $\nu^{1-0} = 23.38348$ GHz and $\nu^{2-1} = 46.76607$ GHz for MM18423.

C-band Observations

The observations at 5 GHz (or 6 cm) were made through the 25th of July to the 16th of August 2011. In total ten observations were carried out. During each observing run a phase reference source (J1849+6705) was frequently observed for approximately a minute followed by 5-6 minutes on target. At the end of each run a flux calibrator was observed for around 10 minutes to set an absolute flux scale. Depending on the specific run, this calibrator was either 3C48 or 3C286; two in a small list of well known calibrator sources for the VLA. Both objects are quasars with an accurate source model available as described in [Perley and Butler 2013](#). [Rothberg et al. 2013](#) and [Farnes et al. 2014](#) list their respective redshifts as $z = 0.367$ and $z = 0.848$. All in all, taking into account the calibration and data reduction, the total time on target was 6h48m43s.

During these observations the array was in its A configuration, having baselines up to 36.4 km. At this frequency the resulting field of view is 8.3' with an synthesized beam of 0.34". The receiver was operating with two spectral windows from 4.832 – 4.959 GHz and 4.960 – 5.023 GHz. Each spectral window consisted of 64 channels of 2 MHz bandwidth, resulting in a 256 MHz total bandwidth.

K-band & Q-band Observations

Various observations of the molecular gas in this galaxy have been made with the VLA:

- From the 21st of October 2010 to the 9th of January 2011 observations were made in the C configuration: four Q-band observations and one K-band observation (project code 10B-245). This data was previously published by [Lestrade et al. 2011](#).
- From the 30th of September 2011 to the 12th of November 2011, observations were made in the D configuration: three Q-band observations and one K-band observation (project code 11B-002). Two of the Q-band observations were found to be unsuitable for further analysis due to a missing flux calibrator (QD02) or significantly larger noise compared to the others (QD03).
- From the 24th of May 2012 to the 8th of August 2012 observations were made in the B configuration: six Q-band observations and three K-band observations (project code 11B-002). One of these observations (QB06) had no flux calibrator and was therefore not used in further analysis.

Data Set	Date	Start [UTC]	End [UTC]	Flux Calibrator	Time on Target
CA01	14-08-2011	07:40:56.0	09:10:41.0	3C48	59 ^m 40 ^s
CA02	25-07-2011	22:57:34.0	00:27:01.0	3C286	59 ^m 40 ^s
CA03	27-07-2011	10:51:30.0	11:51:12.0	3C48	32 ^m 48 ^s
CA04	05-08-2011	06:46:40.0	07:46:24.0	3C48	32 ^m 54 ^s
CA05	07-08-2011	08:08:39.0	09:08:19.0	3C48	32 ^m 48 ^s
CA06	08-08-2011	08:04:40.0	09:04:20.0	3C48	32 ^m 48 ^s
CA07	16-08-2011	04:04:58.0	05:04:39.0	3C48	32 ^m 48 ^s
CA08	30-07-2011	23:01:16.0	00:31:01.0	3C286	59 ^m 40 ^s
CA09	29-07-2011	10:43:39.0	11:43:20.0	3C48	32 ^m 49 ^s
CA10	30-07-2011	08:40:01.0	09:39:45.0	3C48	32 ^m 48 ^s

TABLE 2.8: Summary of the 11A-195 C-band observations in the A-array resulting in 6^h48^m43^s effectively on the target.

Data Set	Date	Start [UTC]	End [UTC]	Flux Calibrator	Time on Target
KD01	17-10-2011	23:12:56	04:11:46	3C286	3 ^h 30 ^m 55 ^s
QD01	30-09-2010	01:06:53	06:05:54	3C286	3 ^h 30 ^m 10 ^s
QD02	14-10-2011	00:29:40	05:10:50	-	3 ^h 09 ^m 20 ^s
QD03	15-12-2010	00:30:45	02:30:25	3C286	3 ^h 31 ^m 00 ^s

TABLE 2.9: Summary of the 11B-002 D-array observations resulting in 10^h10^m25^s effectively on the target for the Q-band and 3^h30^m55^s for the K-band. Datasets QD02 and QD03 however could not be used for analysis however due to missing flux calibrator observations. KD entries are K-band observations and QD entries are Q-band observations.

Data Set	Date	Start [UTC]	End [UTC]	Flux Calibrator	Time on Target
KB01	24-05-2012	05:31:44	10:30:47	3C286	3 ^h 27 ^m 25 ^s
KB02	27-05-2012	05:49:50	10:48:54	3C286	3 ^h 27 ^m 20 ^s
KB03	30-05-2012	06:23:07	11:22:18	3C286	3 ^h 28 ^m 55 ^s
QB01	23-07-2012	06:04:58	11:04:03	3C286	3 ^h 30 ^m 10 ^s
QB02	31-07-2012	04:59:59	09:59:04	3C286	3 ^h 30 ^m 10 ^s
QB03	01-08-2012	04:59:44	09:58:46	3C286	3 ^h 31 ^m 00 ^s
QB04	03-08-2012	01:52:29	06:51:27	3C286	3 ^h 31 ^m 00 ^s
QB05	06-08-2012	03:40:17	09:01:23	3C286	3 ^h 31 ^m 00 ^s
QB06	08-08-2012	04:02:17	09:01:23	3C286	3 ^h 31 ^m 00 ^s

TABLE 2.10: Summary of the 11B-002 B-array observations resulting in 10^h23^m40^s effectively on the target for the K-band and 3^h30^m55^s for the Q-band. KB entries are K-band observations and QB entries are Q-band observations.

Data Set	Date	Start [UTC]	End [UTC]	Flux Calibrator	Time on Target
QC01	31-10-2010	02:32:28	04:32:08	3C48	1 ^h 21 ^m 46 ^s
QC02	29-11-2010	23:05:35	01:05:15	3C48	1 ^h 21 ^m 47 ^s
QC03	15-12-2010	00:30:45	02:30:25	3C48	1 ^h 21 ^m 49 ^s
QC04	09-01-2011	23:53:48	01:53:28	3C48	1 ^h 21 ^m 49 ^s

TABLE 2.11: Summary of the 10B-245 C-array observations. A total time of 5^h26^m29^s was spend on target.

Band	Configuration	Resolution ["]	Scale [kpc]
C	A	0.36	2.58
K	B	0.24	1.72
	C	0.79	5.66
	D	2.6	18.6
Q	B	0.12	0.86
	C	0.39	2.80
	D	1.3	9.3

TABLE 2.12: The different array configurations for each band with their corresponding resolutions and the physical scale they probe at the distance of this galaxy, not taking into account lensing effects.

Tables 2.8, 2.9, 2.10 and 2.11 summarize the observations listing the flux calibrator and the total time spent on MM18423. With observations in different array configuration the interferometer is sensitive to radiation on various spatial scales. We can use these different measurements to extract different pieces of information. For example, since the source is likely to be largely unresolved in the D-array, this configuration will be most reliable to determine the total flux density of the line emission. The C and B-array data, with their higher resolution, can then be used to further determine the spatial distribution of the gas. The field of view is configuration independent, being set by the observing wavelength and the size of the dish. For the K-band, the field of view is $1.8'$ and for the Q-band it is $53''$. The resolution is set by the distribution of antennas and therefore does depend on the array configuration. For these observations, the resolutions were (in the order of D, C and B array) $2.6''$, $0.79''$ and $0.24''$ for the K-band. For the Q-band they were $1.3''$, $0.39''$ and $0.12''$, respectively. Table 2.12 summarizes the observations in resolution, spatial scales probed on the sky and total observing bandwidth.

2.2.2 Data Reduction

Data reduction for radio observations are drastically different from reducing data of optical instruments. One does not work with the images directly, but instead data is reduced in the *visibility space*. Because of this I will first explain the theory behind radio observations with interferometers. Afterwards I will describe the actual reduction and calibration.

Radio Astronomy: Observing with Interferometers

An interferometer measures a signal from a certain direction on the sky having an amplitude A and phase ϕ . The phase is not absolute (an interferometer always measures relative phase), but is measured with respect to a reference antenna which has its phase set to 0 and is usually chosen near the center of the array. Together these define *the complex visibility*

$$V_{ij} = A_{ij}e^{i\phi_{ij}} \quad (2.6)$$

where i is the imaginary unit and the subscript ij indicates the visibility measured by the baseline of antenna i and antenna j .

We can relate the measured visibilities to the source brightness by considering the simple case of a two-element interferometer; illustrated in Fig. 2.15. A baseline

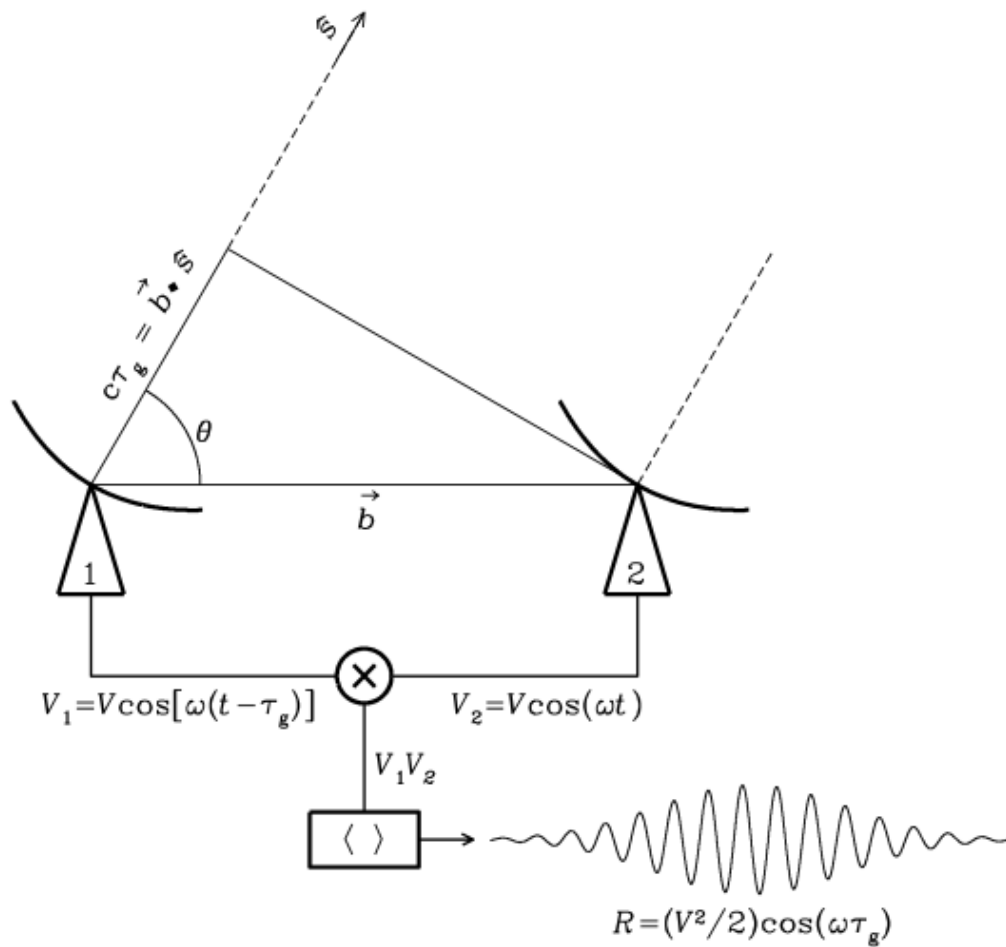


FIGURE 2.15: The simple case of a two-element interferometer. The baseline is given by the baseline vector \vec{b} and the source is located in a direction \hat{s} , a unit vector in the direction of the source. This introduces a time delay τ_g between the antennas with respect to when they receive the signal. The signals are then correlated and averaged to produce a response R .
Image credit: NRAO

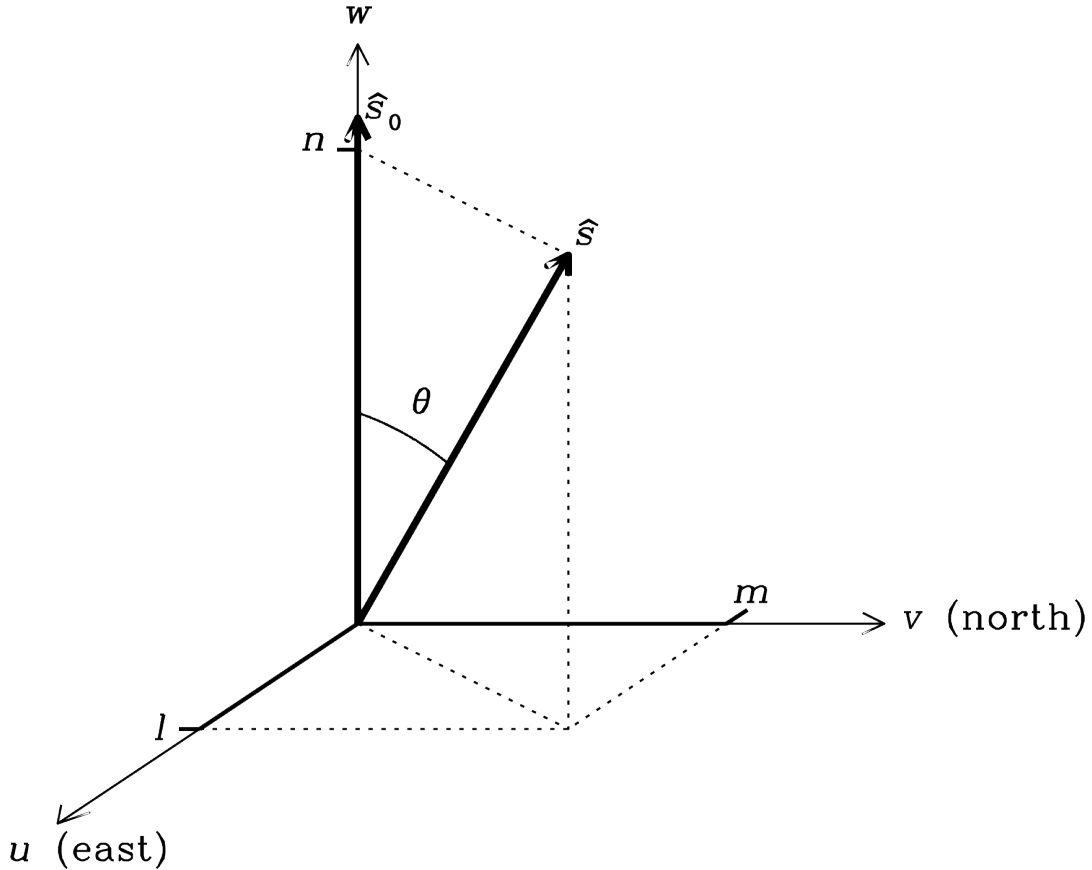


FIGURE 2.16

\vec{b} is formed by the two antennas pointing towards the source in the direction \hat{s} . These vectors live in two different coordinate systems. The baseline vector \vec{b} , i.e. the interferometer, lives in (u, v, w) space, while the direction vector \vec{s} lives in (l, m, n) space which are projections of \vec{s} onto the u, v, w axes. The coordinates u, v and w are expressed in units of wavelength, i.e. $\vec{b} = (\lambda u, \lambda v, \lambda w)$ is the physical length of the baseline. Figure 2.16 illustrates these two coordinate systems. With these quantities we can then introduce the *geometric delay*, which is the time difference by which a signal from a plane wave arrives at both antennas. This delay is given by

$$\tau_g = \frac{\vec{b} \cdot \vec{s}}{c} \quad (2.7)$$

where c is the speed of light. It can be shown (e.g. Taylor et al. 1999) that we can use these quantities to relate the intensity I_ν of the source to the measured visibilities V_ν as

$$V_\nu(\vec{b}) = \iint I_\nu(\vec{s}) e^{-2\pi i \nu \tau_g} d\Omega = \iint I_\nu(\vec{s}) e^{-2\pi i \nu \vec{b} \cdot \vec{s} / c} d\Omega \quad (2.8)$$

where the subscript ν indicates the frequency dependency. This is known as the *van Cittert-Zernike theorem*. It tells us that a measurement of the visibility by a given baseline is a superposition of sinusoidal waves with an amplitude determined by the observed source and a phase ϕ given by $2\pi \nu \tau_g = 2\pi \nu \vec{b} \cdot \vec{s} / c$. The dot product can

then be expanded as $v\vec{b} \cdot \vec{s}/c = \vec{b} \cdot \vec{s}/\lambda = ul + vm + wn$ giving

$$V_v(u, v, w) = \iiint \frac{I_v(l, m)}{\sqrt{1-l^2-m^2}} e^{-2\pi i(ul+vm+wn)} dl dm \quad (2.9)$$

where we have substituted the solid angle $d\Omega = \frac{dl dm}{\sqrt{1-l^2-m^2}}$. In the special case of $w = 0$, this relation turns into a two-dimensional Fourier Transform between the projected sky brightness and the visibilities:

$$V_v(u, v) = \iint \frac{I_v(l, m)}{\sqrt{1-l^2-m^2}} e^{-2\pi i(ul+vm)} dl dm \quad (2.10)$$

which can be inverted as

$$\frac{I_v(l, m)}{\sqrt{1-l^2-m^2}} = \iint V_v(u, v) e^{2\pi i(ul+vm)} du dv. \quad (2.11)$$

The basis of imaging with interferometry is based on the assumption that we can use this 2D Fourier Transform which can be solved (relatively) quickly on computers using FFTs. Doing the full integral with a w term is much more computationally intensive. Next we will see this assumption is generally valid.

Let us go back to Eqn. 2.9 and have w point towards the source. We can then substitute n in the exponential with $\cos \theta$ (see Fig. 2.16 and recall \vec{s} is a unit vector) where θ is the polar angle w.r.t the center. For small angles θ we can do the second order Taylor expansion $\cos \theta \approx 1 - \frac{\theta^2}{2}$. This changes the visibility equation into

$$\begin{aligned} V_v(u, v, w) &= \iint \frac{I_v(l, m)}{\sqrt{1-l^2-m^2}} e^{-2\pi i(ul+vm+w(1-\frac{\theta^2}{2}))} dl dm \\ &= e^{-2\pi iw} \iint \frac{I_v(l, m)}{\sqrt{1-l^2-m^2}} e^{-2\pi i(ul+vm-w\frac{\theta^2}{2})} dl dm \end{aligned} \quad (2.12)$$

which for $\frac{w\theta^2}{2} \ll 1$ becomes Eqn. 2.13.

$$V_v(u, v) = e^{-2\pi iw} \iint \frac{I_v(l, m)}{\sqrt{1-l^2-m^2}} e^{-2\pi i(ul+vm)} dl dm \quad (2.13)$$

$$\frac{I_v(l, m)}{\sqrt{1-l^2-m^2}} = e^{-2\pi iw} \iint V_v(u, v) e^{2\pi i(ul+vm)} du dv \quad (2.14)$$

Now instead of a complicated double integral we have reduced the problem to a two dimensional Fourier Transform relation with an extra phase rotation $e^{-2\pi iw}$. When pointing in the direction of the source we have $\vec{s} = (0, 0, 1)$ and we can see that

$$v\tau_g = v \frac{\vec{b} \cdot \vec{s}}{c} = w \quad (2.15)$$

and hence this phase rotation is effectively the geometric delay we introduced earlier. Equations 2.13 and 2.14 form the basis of making observations with interferometers: the (projected) sky brightness distribution and the measured visibilities are linked by a Fourier Transform.

Radio Astronomy: The Measurement Equation

Calibration of VLA Data

Before we can start recovering the actual sky brightness from the visibilities, the data first need to be processed to remove faulty measurements or otherwise unusable parts of the data. This is known as *flagging*. Subsequently, the data needs to be calibrated. The process of flagging and calibrating the data is essentially the same for all data sets. Therefore, in this section I will go through the reduction of one data set in detail only, QC01, describing step by step the process.

FLAGGING Flagging is a manual process in which you identify bad visibilities and “flag” them. This way the data points are not removed, but you just tell the software not to use them during e.g. calibration. The term bad visibilities is rather general and can be a bit subjective. There are the obvious cases in which visibilities are unusable:

- Near-zero amplitude because antennas were not fully online or on target.
- *Radio frequency interference* (RFI) where signals from satellites, radio stations or cell phones, for example, cause a spike in amplitude.
- Zero amplitude due to correlator errors.
- Random phases

There are also the more subjective cases where one may consider the visibilities to be acceptable, while someone else would consider them “bad”. This is usually when dealing with the spread in the visibilities. Certain baselines can be noisier than others. If this noise is not easily attributable to a single baseline or antenna, one needs to decide for themselves what to keep and what to flag.

CALIBRATION To calibrate the radio data, we used the *Common Astronomy Software Applications* package `CASA` version 4.6.0. This package provides commands for doing the various steps required to correctly calibrate a dataset. Because there were many datasets to be reduced and calibrated (23 in total) these steps were put together in a Python script to make them easier to execute multiple times. The base for this script was provided by my supervisor. I then expanded on this script to make it more automated and adaptive to measurements taken by the VLA in different arrays or in different bands. A complete calibration script is provided in Appendix A. I will now shortly introduce the steps taken in the calibration and I will describe them in detail next.

For a complete calibration, the following steps are done:

- | | |
|---------------------------------|----------------------------------|
| 0. Initial split | <code>split, listobs</code> |
| 1. A priori calibration | <code>plotweather, gencal</code> |
| 2. Flag bad data | <code>flagdata</code> |
| 3. Insert flux calibrator model | <code>setjy</code> |
| 4. Short phase correction | <code>gaincal</code> |
| 5. Delay correction | <code>gaincal</code> |
| 6. Bandpass calibration | <code>bandpass</code> |

7. Gain calibration	gaincal
8. Determine absolute fluxscale for calibrators	fluxscale
9. Apply calibration tables	applycal
10. Split target	split
11. Self calibrate	gaincal
12. Continuum subtraction	uvcontsub or imcontsub

The text on the right indicates the `CASA` task(s) used in that step. The last two steps are shown in grey, because they were not used for the calibration of these datasets. This will be explained in their respective sections. Calibration with `CASA` is done through calibration tables. Using a model, corrections are calculated and stored in these tables. The corrections are effectively determined “in reverse”. Instead of working out how to correct the data to best match the model, `CASA` works out how to distort the model to best match the data.

STEP 0: INITIAL SPLIT We will only be using two of the four polarisations in this project: RR and LL. We are only interested in the total intensity of the emission ($I = (RR + LL) / 2$) so the crosspolarisations RL and LR are not required. The `split` task is used to extract the RR and LL components into a new MS file. This reduces the size of the dataset as an added bonus. After splitting the `listobs` task is used to store information about the measurement set in a text file.

STEP 1: A PRIORI CALIBRATION This step contains calibrations that are independent of the data: antenna positions, atmospheric opacity and gain corrections. The VLA switches array configurations from time to time. Although the antennas have designated positions for each configuration, there may be slight errors when an antenna is moved. Therefore, their positions are regularly checked and corrections are made available if needed. This calibration is generated with the `gencal` task using `caltpe antpos`. This calibration queries the VLA database for corrections and thus requires an internet connection.

The second calibration we can make a priori is one for the atmospheric opacity. Radiative transfer theory tells us the opacity τ_ν affects the signal as

$$I_\nu(s) = I_\nu(0)e^{-\tau_\nu} \quad (2.16)$$

in the simplest case where I_ν is the intensity and s is the path length. The optical depth can possibly significantly attenuate the signal, so calibrating for it is useful. The optical depth is calibrated per spectral window. First an estimate of the mean zenith opacity τ_z is made with the `plotweather` task. This returns one estimate per spectral window along with a plot showing various weather statistics as shown in Fig. 2.17. These values are then passed to `gencal` to generate the actual calibration table.

The final calibration table made during this step is a correction to the gain using `caltpe gceff`. The antennas will distort slightly due to gravity, introducing an effect that is elevation dependent. Because the antenna changes slightly this means the gain will change with elevation. This step generates a correction for this effect.

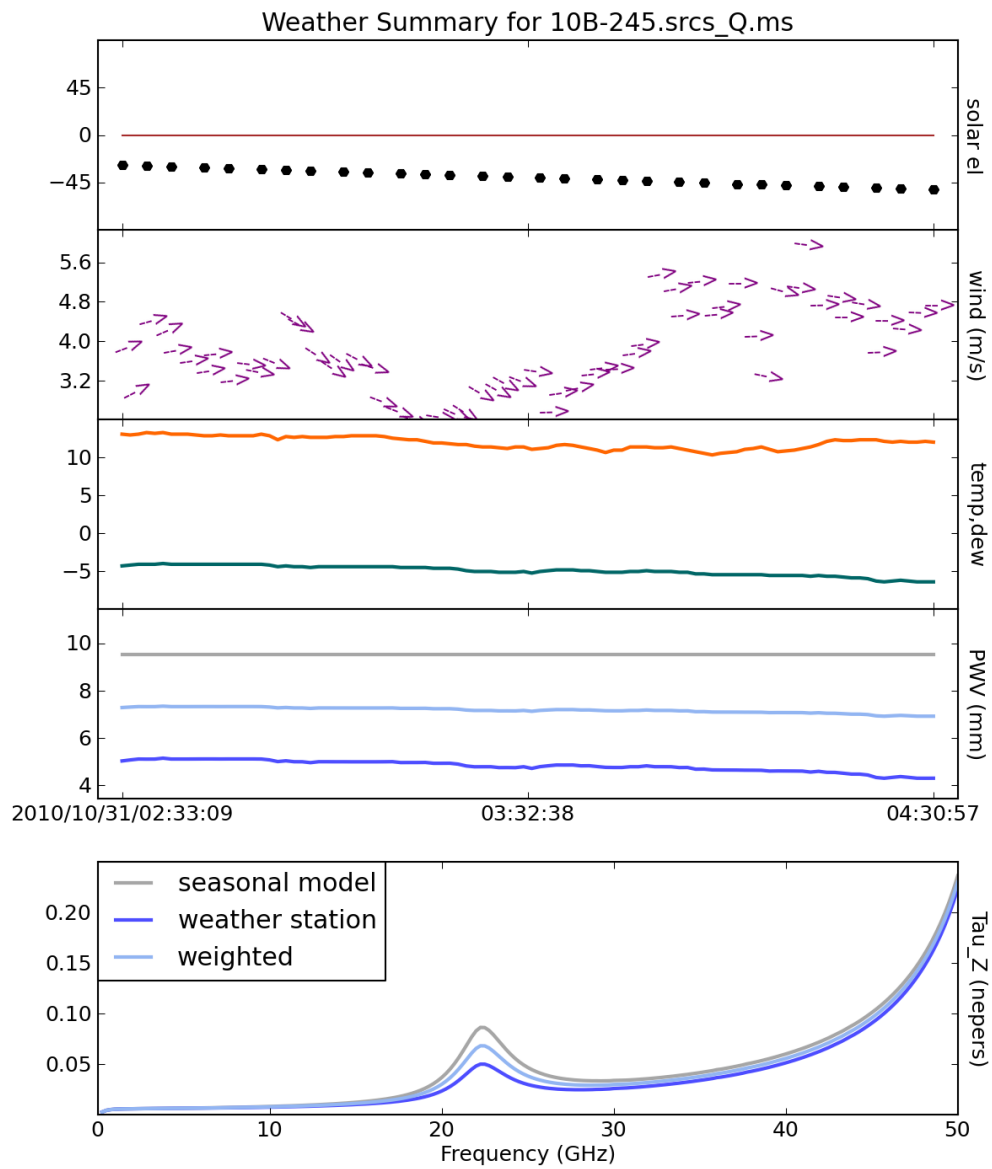


FIGURE 2.17: The weather plot generated by the `plotweather` task in `CASA`. From top panel: solar elevation in degrees, wind speed in m/s, dew temperature in $^{\circ}\text{C}$ and precipitable water vapor in mm. In the bottom panel: zenith opacity in Nepers from weather data, seasonal models and the weighted average.

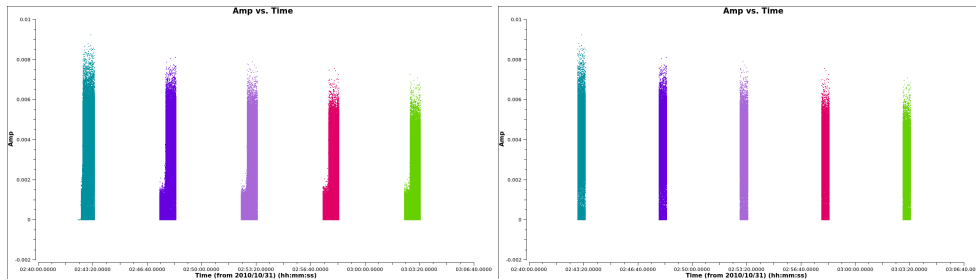


FIGURE 2.18: A comparison of amplitude vs. time for a couple of scans on the phase reference source before (*left*) and after (*right*) applying the flags. The small steps at the beginning are antennas caused by not having full signal yet due to antennas that are not on target. Data in the plot is averaged in 64 channel bins.

STEP 2: FLAGGING As explained above, flagging is done to mark visibilities that should not be used during calibration and imaging. Most of this has to be done by manually inspecting the data and then passing the relative settings to the `flagdata` task manual mode in order to flag them. There are two flags that can be applied automatically: flags for bad values and flags for timeranges at the start of each scan. Using the `clip` mode with no specified limits all values that are NaN or inf will be flagged. Using `quack`, one can flag the first X seconds of the beginning of each scan. For example, when not all antennas are on source yet. All datasets had a quack time range of the order of 25-30 seconds. Figure 2.18 shows an example of the amplitude plotted against time before and after running `quack`.

STEP 3: FLUX CALIBRATOR MODEL The power measured by the telescopes is arbitrary and does not hold meaning without a solid reference point. To convert measurements of the source into something physical, a flux calibrator is observed during the observation. To make this calibrator source physical, we insert an (accurately known) model of what the source looks like on all baselines in a given configuration using the `setjy` task. For these models, multiple standards are available. Here we used the models described by [Perley and Butler 2013](#) with the only difference being we used the slightly older models with the “Perley-Butler 2010” standard instead. The difference is that the former models are determined with EVLA (the current version) observations while the latter are old-VLA observations, though this will most likely have minimal impact on our results since we are observing close to the old K-band center frequency.

Different configurations and different bands will result in the array being sensitive to different physical scales. Hence the models will change for each combination. Figure 2.19 shows the model of 3C48 for a C-array, Q-band observation. At the shortest baselines the amplitude is constant, indicating an unresolved point source. At longer baselines, the amplitudes start to change. They drop and fill in a larger portion of the vertical scale, because structure is starting to be resolved out as we are probing the object at smaller physical scales.

STEP 4: SHORT PHASE CALIBRATION Here we will do a first calibration of the phases. The phase will change with both time and frequency. In this step we will assume the phases to be independent of frequency however and solve for changes on short timescales (every integration) first. We do this for both RR and LL separately by specifying `gaintype G` in `CASA's` `gaincal` task. Setting `calmode` to `p` makes it such that only phases are calibrated at this point. To make the assumption of frequency

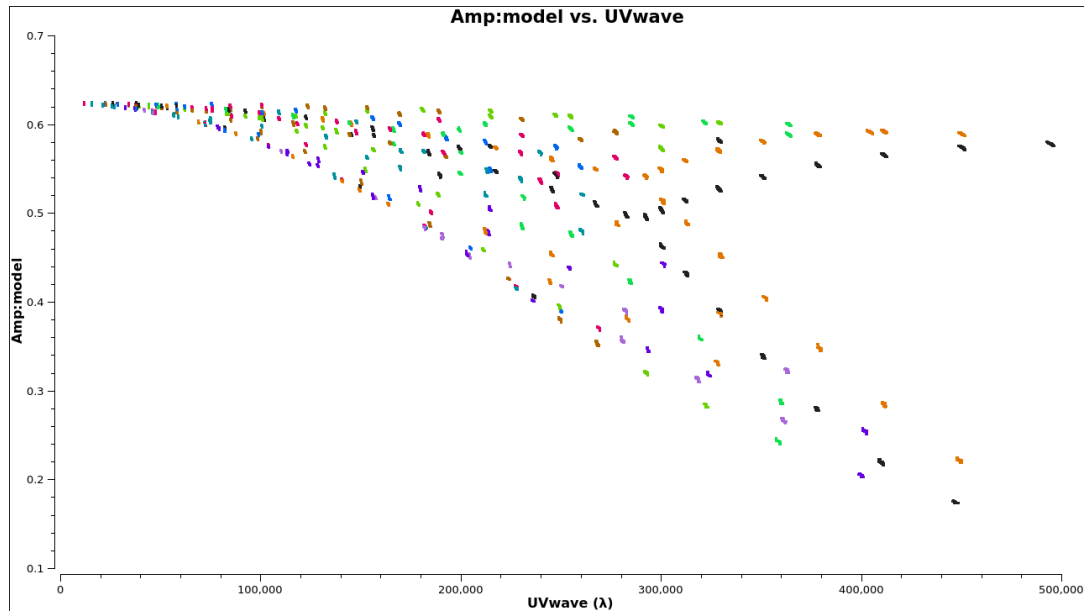


FIGURE 2.19: The inserted model for the flux calibrator source 3C48 in the C-array for the Q-band plotted as amplitude against UV distance in units of wavelength (i.e. b/λ). The colors indicate different baselines. As baseline length increases, we see the visibilities for 3C48 becoming more spread out. This indicates the source structure is being resolved differently by the array.

independent changes plausible we reduce the number of channels that are used from the full 64 down to the 8 central channels. In Fig. 2.20 we can see the phase plotted against time for the phase reference source. We see that the phase changes rapidly over short timescales. This is mostly due to atmospheric effects. Turbulence in the air for example causes the index of refraction to change slightly which changes the phase of the incoming signal. As the phases encode positional information about the source this will eventually manifest itself as the source appearing to move across the sky, smearing the image. The reason for calibrating this rapid phase change now is that in the next step (bandpass calibration) the data will be vector-averaged over time. This means the real and imaginary part (i.e. amplitude and phase) are averaged separately. If the atmospheric fluctuations could be considered to be random then they would average out to zero and this step would not be necessary. In principle this could be argued to be true for the sky above a single antenna, but since the antennas are separated by large distances, the sky above them is different. Therefore, on a global scale, we cannot assume the atmospheric fluctuations to be random and we need to calibrated for them. Figure 2.20 shows phase against time for the baseline between antennas ea02 and ea06. The slow change in phase over time can be seen with a faster scatter on top.

This is calibrated against the model phase against time shown in Fig. 2.21 which produces the corrections shown in Fig. 2.22. The result of applying the calibrations from this step is shown in Fig. 2.23.

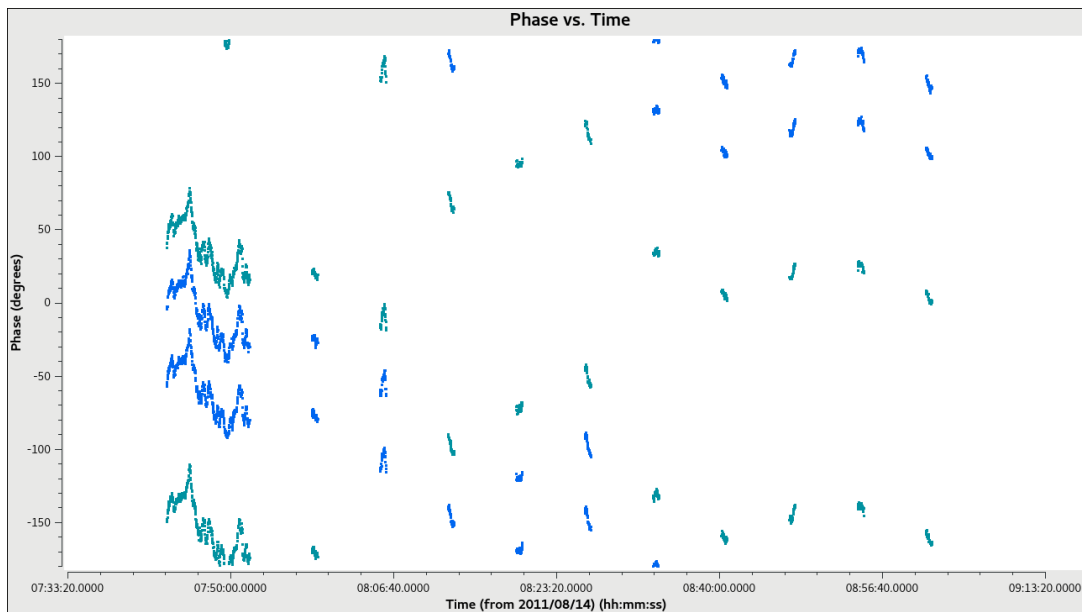


FIGURE 2.20: Phase against time on baseline ea02-ea06 before doing the phase calibration on short timescales. Rapid variations of the phase are visible on top of a slow variation on longer timescales. The colors indicate the correlations for both spws: RR (*teal*) and LL (*blue*).

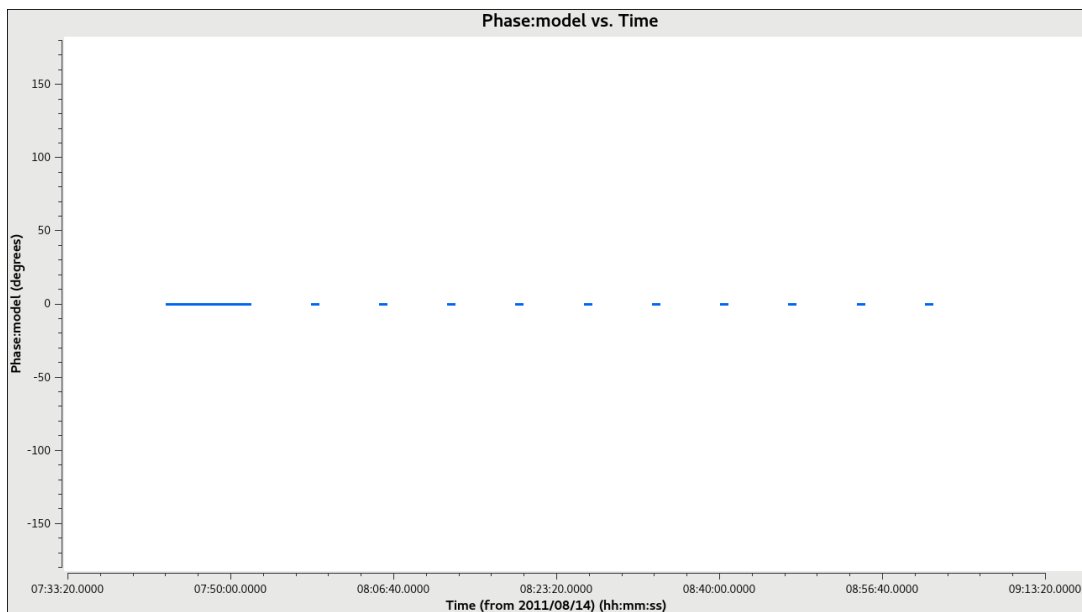


FIGURE 2.21: The model phase against time for the phase reference source on baseline ea02-ea06 against which the data will be calibrated. In the model the phase remains constant over time as would be the case without atmospheric interference and a point source model.

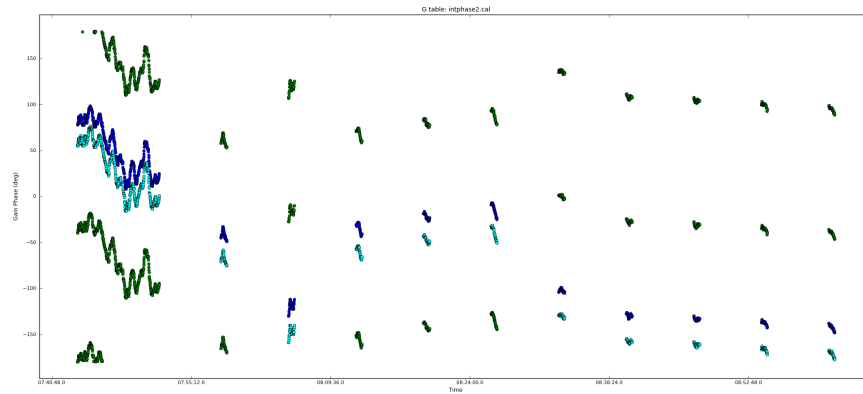


FIGURE 2.22: The corrections calculated by gaincal plotted as phase against time. They resemble the observed data because of the way CASA applies calibrations.

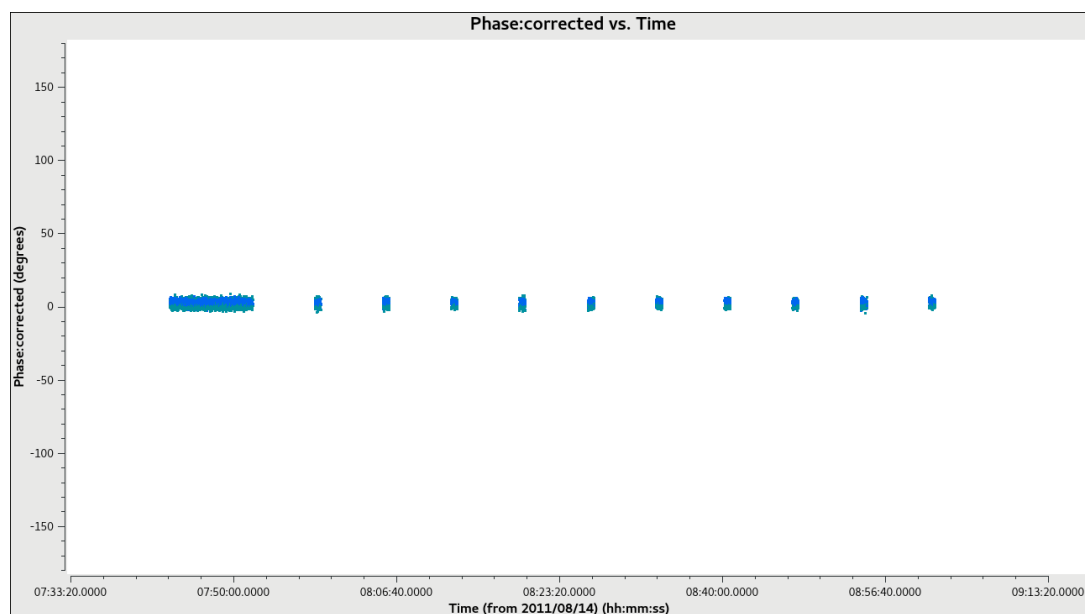


FIGURE 2.23: The corrected phase against time for the phase reference after applying the calibrations. Now the phases lie around zero and are constant over time.

STEP 5: DELAY CALIBRATION Having done a calibration for the phases as a function of time, we will now do the same as function of frequency. This now means our assumptions will be reversed with respect to the previous step. We will assume time independency and average all integrations while using the full range of channels (except a few edge channels). This step calibrates for the residual geometric delay (introduced at the beginning of this section) that has not been removed by the correlator. For each spectral window, the delay of an antenna with respect to the reference antenna will be determined. The different frequencies will all arrive with a different phase and hence there will be a slope in the phase as a function of frequency. This can be seen in Fig. 2.24, where the phases are plotted for the uncalibrated data. There is a clear slope in the phases. Model visibilities for this step are shown in Fig. 2.25 and result of applying this calibration is shown in Fig. 2.26: the phases are now flat with respect to the frequency.

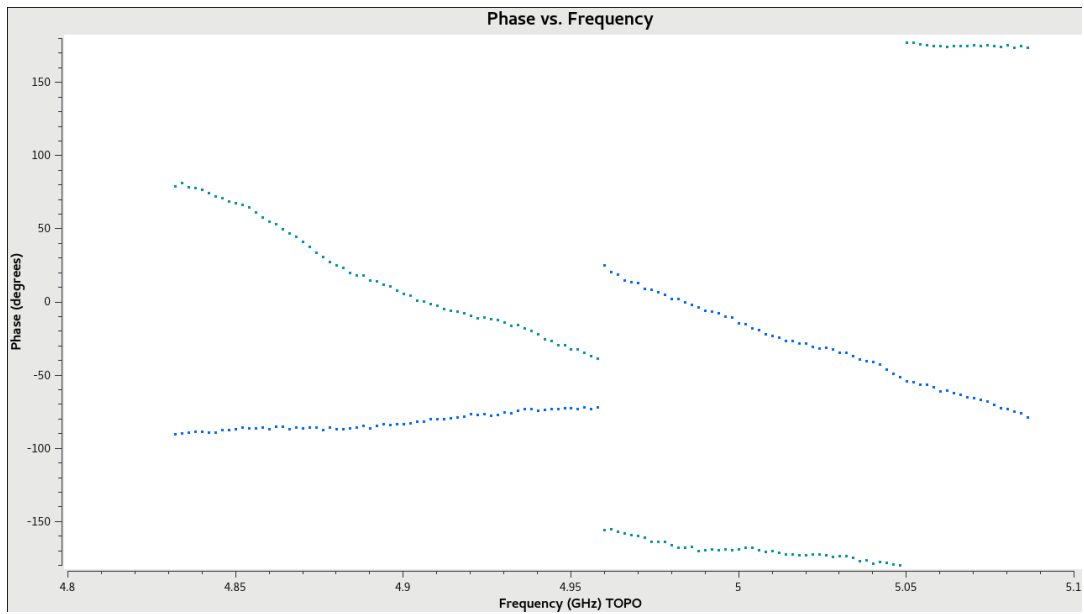


FIGURE 2.24: Phase against frequency on baseline ea02-ea06 for the raw data of the phase reference without any calibration applied. The phases are seen to wrap over 180° and also increase or decrease with frequency.

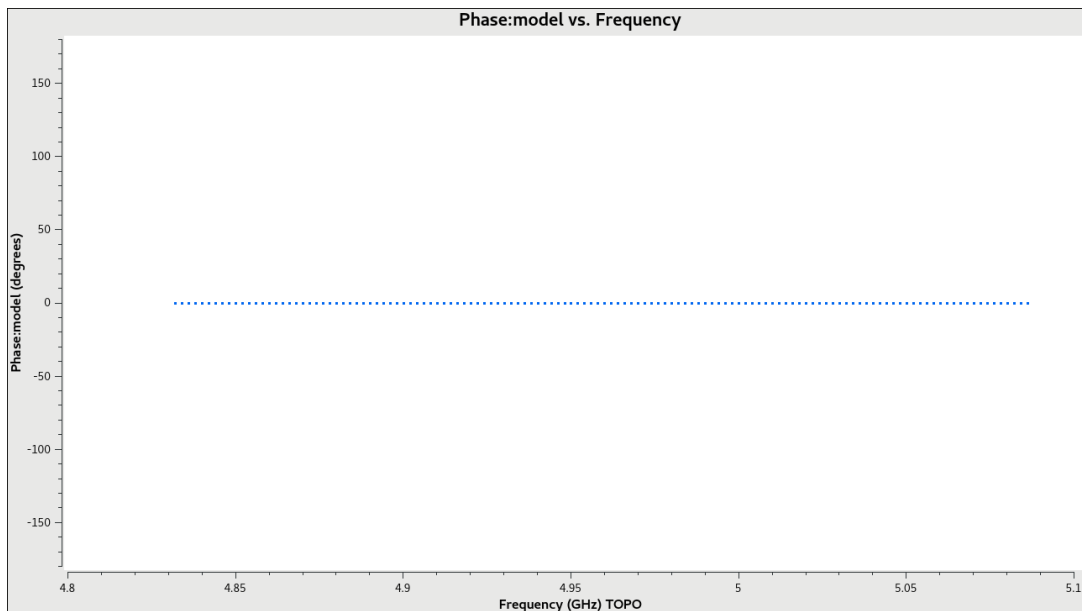


FIGURE 2.25: The model phase against frequency for the phase reference source on baseline ea02-ea06 against which the calibration is done.

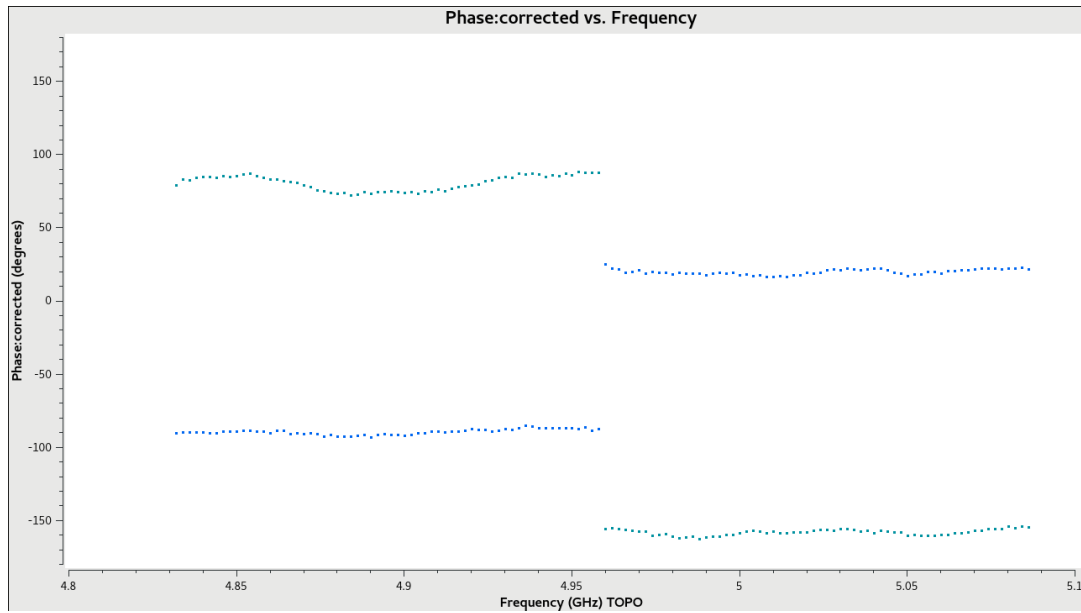


FIGURE 2.26: Corrected phase against frequency on baseline ea02-ea06 for the phase reference source, after applying the corrections for residual delays. The phases are now constant with respect to frequency as would be expected. As we now use the full range of channels and not just the center, the phases do not lie around zero yet. This is corrected in later stages.

STEP 6: BANDPASS CALIBRATION The delay calibration in the previous step only deals with residual delay on a spectral window basis. Now that the phases are flat, after bandpass calibration they will be calibrated to lie around zero.

Looking at the amplitude against frequency for uncalibrated data, reveals that the response is not uniform over a spectral window. Figure 2.27 shows uncalibrated data for the baseline ea02-ea06 as amplitude against frequency. The edge channels have a lower signal strength (which is why they are left out of the calibration process) and there is arguably some structure in the bandpass. The model visibilities for what the amplitude should look like as a function of frequency are shown in Fig. 2.28. After calibration, the visibilities look like as shown in Fig. 2.29. Most notable is the change in amplitude after the bandpass calibration is applied. Instead of arbitrary correlator units the amplitude is now expressed in physical units that can be used to measure the flux of the object.

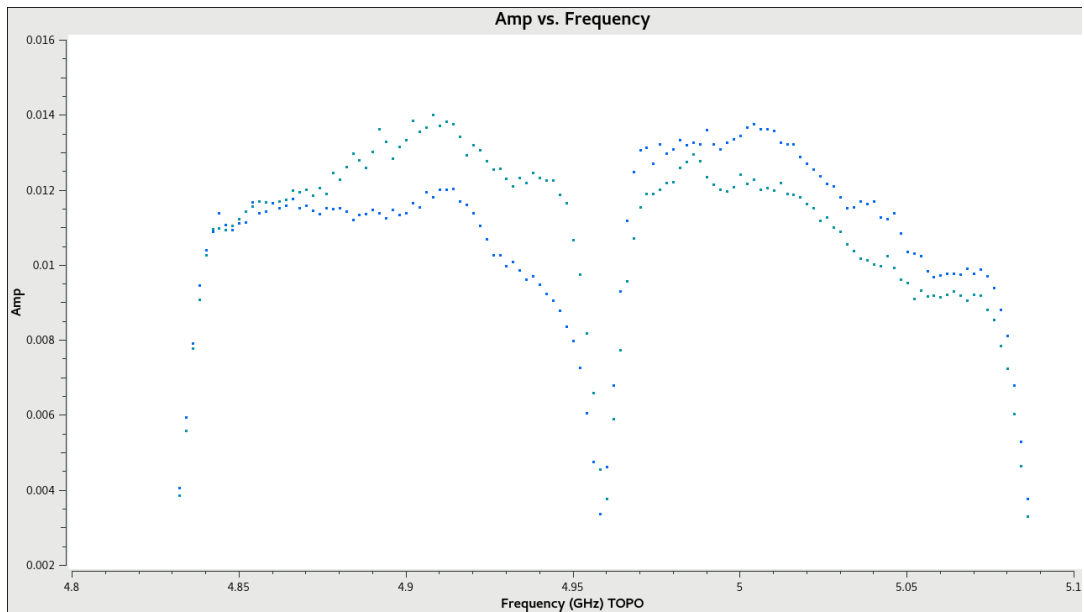


FIGURE 2.27: Amplitude against frequency for the raw data of the phase reference on baseline ea02-ea06. The edge channels have a lower response compared to the central channels and are therefore left out of the calibration steps.

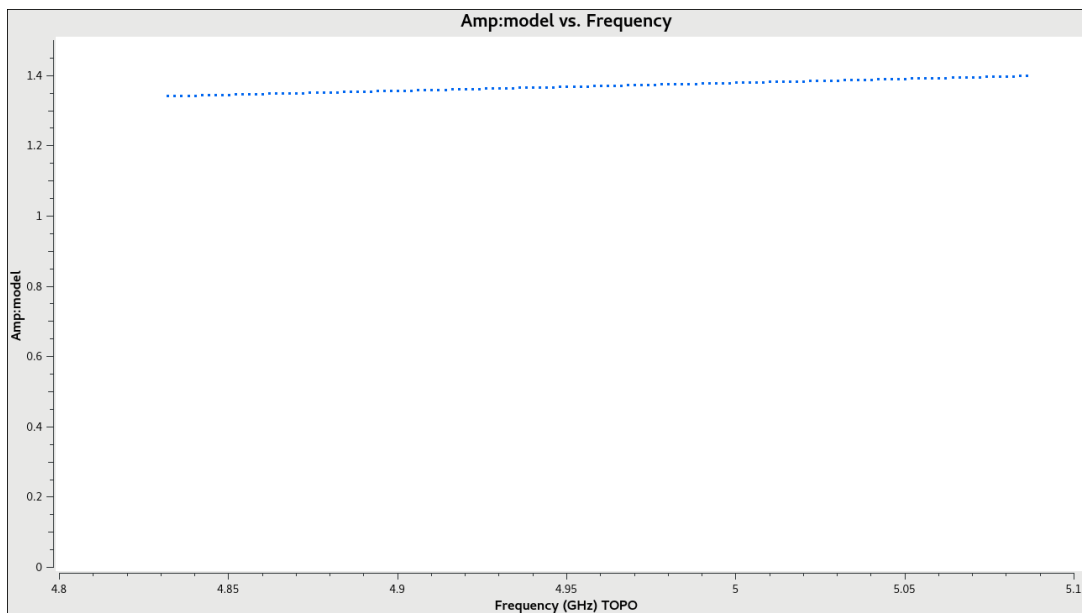


FIGURE 2.28: Model visibilities for the flux calibrator. The fluxscale task scales this model to the phase reference giving what the amplitude should look like on the baseline ea02-ea06. This is used as reference for the calibration. The slope is because of the spectral index of the source.

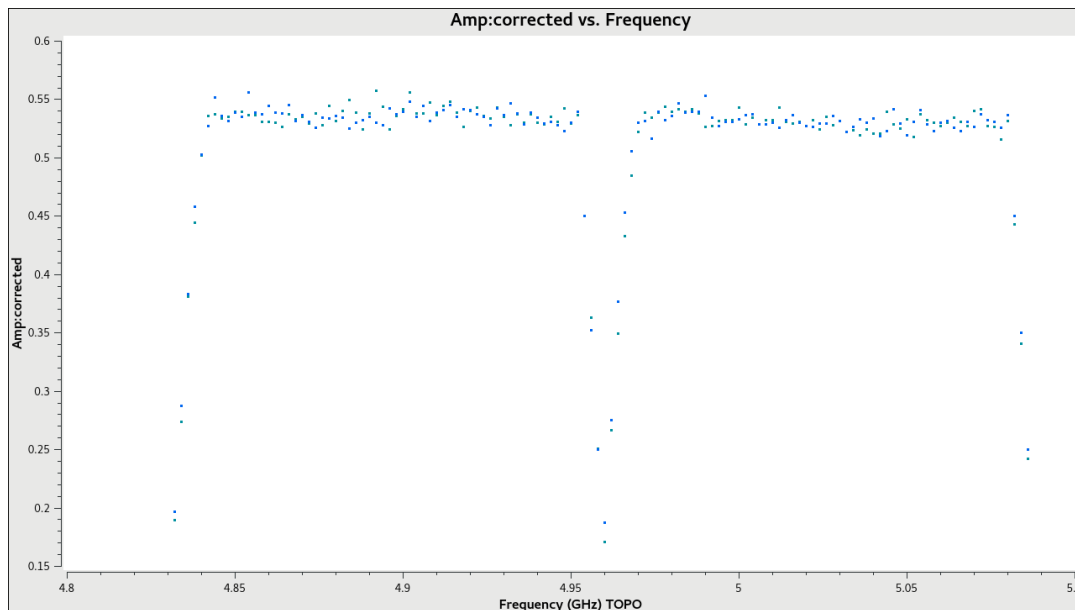


FIGURE 2.29: The corrected amplitude against frequency after applying the bandpass calibration. Notice that the scale of the amplitude has changed significantly.

STEP 7: GAIN CALIBRATION Up till now we have calibrated phase and amplitude separately. We will now use the previously determined calibrations as a function of frequency to solve for the gain as function of time. Another important point to realize is that we only solved for the gain of the *flux calibrator* in the previous steps. To calibrate the target it is necessary to use gain solutions for the phase reference as this is observed much closer to the target so the atmospheric conditions will better approximate those around the target. In effect the gain solutions for the phase reference source are closer to the actual solutions for the source than the solutions for the flux calibrator. Therefore, we now also solve for the gains of the phase reference source using the calibrations as a function of frequency determined for the flux calibrator. The `gaincal` task is run four times in this step. First the gain solutions for the phase are calculated for the flux calibrator and the phase reference source. After this, the gain amplitudes are calculated. For this step the calibration table from step 4 is no longer required, as we will be solving for the gain properly using the full frequency range.

STEP 8: ABSOLUTE FLUX SCALE PHASE REFERENCE We can transfer the flux scale, converting correlator units into physical units from the flux calibrator to the phase reference source using the `fluxscale` task. This is based on the assumption that the gain amplitudes on average will not differ significantly during the observation and between sources. After running `fluxscale` the entire calibration chain is run again, but this time for the phase reference.

STEP 9: APPLY CALIBRATION After each step, the respective calibrations are stored in calibration tables. Using `applycal` these calibrations are applied to the data set. This adds a new column `CORRECTED_DATA` to the MS file where the calibrated data is stored. In this step, the respective calibrators have their own calibrations applied. The only step left is now to calibrate the target. To do this, we apply the gain solutions found for the phase reference to the target. We cannot do the calibration on the source itself, because it is much weaker and has a lower signal-to-noise ratio.

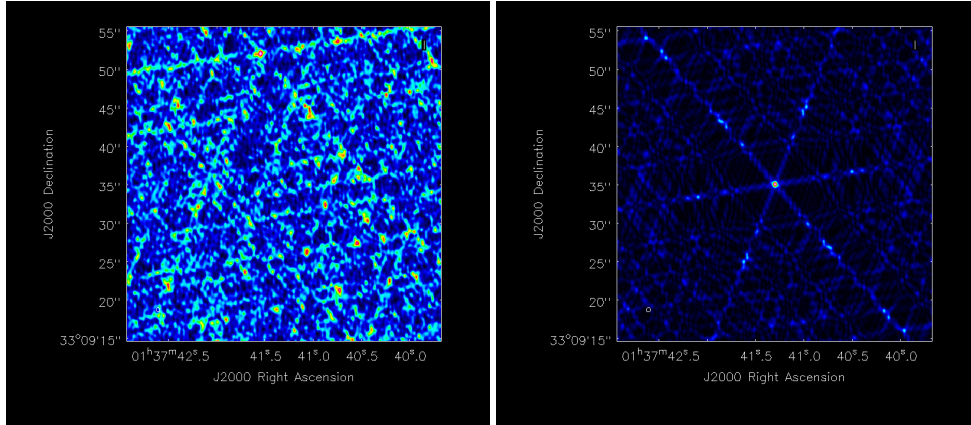


FIGURE 2.30: A comparison between data with only a priori corrections for opacity, gain-elevation dependency and antenna positions applied (*left*) and fully calibrated data (*right*) for the flux calibrator 3C48. Both are created by Fourier transforming the visibilities. The uncalibrated image shows little to no evidence of a source being present. After calibration there is a clear point source in the center.

Furthermore, we do not want to impose any assumptions on what the source looks like in order to do calibration as this is what we intend to find out. Therefore the best we can do is to transfer the calibrations from a nearby source to the target. The effect calibration has on the data is best seen when we Fourier transform the visibilities to create an image. Figure 2.30 shows a comparison between flagged but uncalibrated data (except for the a priori calibrator) and fully calibrated data. The difference is vast. Without calibration there is no indication of a source being there. After calibration, we can clearly see a point source in the middle. In this case it is the calibrator 3C48.

The uncertainties quoted for measurements indicates the true uncertainty from both calibration and map noise: $\sigma = \sqrt{\sigma_{\text{CAL}}^2 + \sigma_{\text{RMS}}^2}$. The calibration uncertainty σ_{cal} was determined by looking at the calibration table for the gain amplitude. The scatter in these solutions gives an estimate of the uncertainty in the calibration.

The CLEAN Algorithm

A final step in the data reduction of radio observations is to clean the images. The process of *cleaning* an image is applying the CLEAN algorithm to create a model of the source. Because we sample the uv -plane discretely during an observation, the measured visibilities $V^D(u, v)$ are given by

$$V^D(u, v) = S(u, v)V(u, v) \quad (2.17)$$

where $S(u, v)$ is the *sampling function*, which is either 1 or 0 depending on whether that uv coordinate had a measurement taken at its position. This is also called the uv coverage. In Fig. 2.31 and Fig. 2.32 the uv coverages of the observation are shown for the flux calibrator and the target source. The star pattern is typical for the VLA due to the Y-shape of the antenna configuration.

If we transform the visibilities we get

$$\mathcal{F}\{V^D(u, v)\} = \mathcal{F}\{S(u, v)V(u, v)\} \quad (2.18)$$

which can be written as

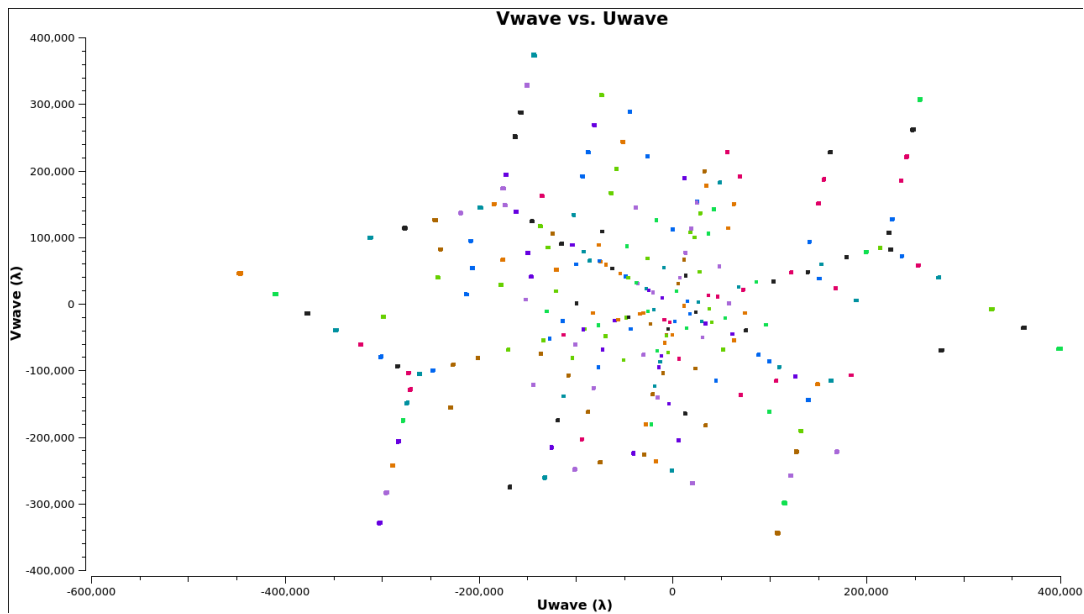


FIGURE 2.31: The uv coverage for dataset QC01 on the flux calibrator. Due to it being a bright source and because we have an accurate model available, not a lot of time was needed on source and as such the uv plane is hardly sampled. The colors indicate different baselines.

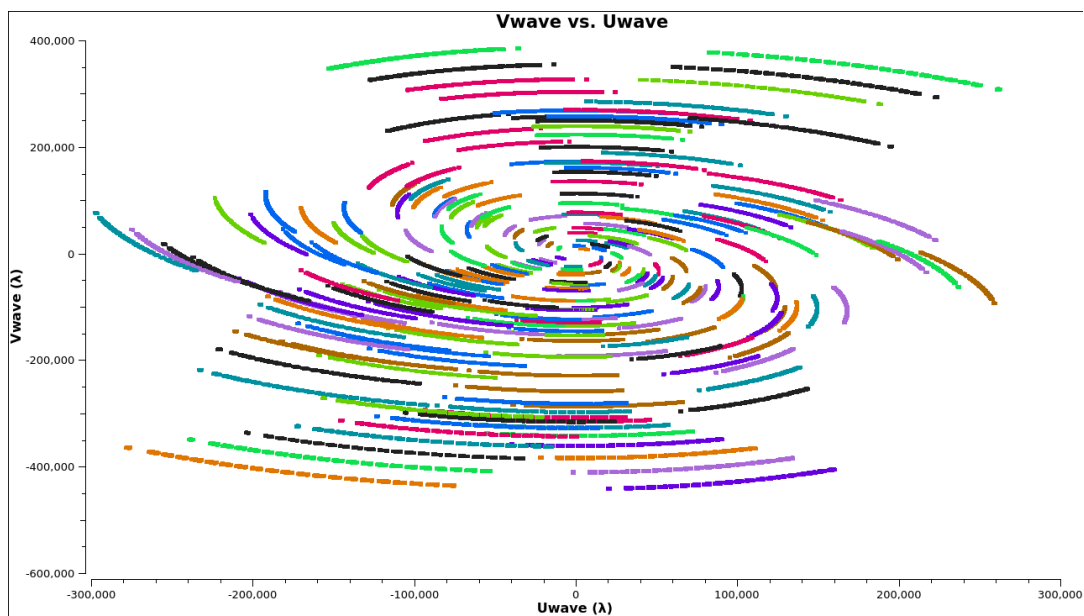


FIGURE 2.32: The uv coverage for dataset QC01 on the target source averaged by 30s intervals. Because of the long time spent on the target, the uv plane is filled in much better compared to the flux calibrator.

$$\mathcal{F}\{V^D(u, v)\} = \mathcal{F}\{S(u, v)\} * \mathcal{F}\{V(u, v)\}. \quad (2.19)$$

This gives us the *dirty image*

$$I^D(l, m) = B^D(l, m) * I(l, m) \quad (2.20)$$

where B^D is the dirty beam (which is the Fourier transform of the sampling function) and I is the sky brightness distribution. The artifacts in Fig. 2.30 are caused by the dirty beam due to incomplete coverage of the uv plane. The better the coverage, the better the dirty beam. With cleaning we get rid of these artifacts by first identifying source components and subsequently convolving these with the *clean beam*. The classic approach for cleaning is the Högbom algorithm described in Högbom 1974, but other versions are also used such as Clark or Cotton-Schwab, for example. By default, *CASA* uses the Clark algorithm, which is what we used throughout the analysis. The source components are identified by finding the maximum in the image or in a user identified search region. At this position, a delta function is added with some fraction of the peak surface brightness. The algorithm then subtracts a small fraction of the dirty beam convolved with this delta function from the data and searches for the next peak. This routine is repeated until either a threshold residual value is reached, the maximum number of iterations is reached or if the user stops cleaning. The subtraction is split up in two cycles. First, there are multiple *minor cycles* in which an approximate dirty beam is used to subtract in the image plane. After a certain number of minor cycles, the algorithm executes a *major cycle* where the model is first transformed from the image plane to the Fourier plane. It is then multiplied by the sampling function, transformed back to the image plane and subtracted. Once cleaning is completed, the model is convolved with the clean beam to create a clean image:

$$I^C(l, m) = B^C(l, m) * I^M(l, m) \quad (2.21)$$

where I^M represents the model components. The clean beam is the central lobe of the dirty beam, i.e. without the sidelobes, and is usually approximated as a two dimensional gaussian.

To stabilize the cleaning process, a loop gain g is set, which determines what fraction of the dirty beam is subtracted from the image. The region in which the algorithm searches for peaks is constrained as well with so-called *clean boxes*, further stabilizing the loop. These clean boxes can be created beforehand or during a cleaning session when in interactive mode. In both continuum studies and spectral line work the data is stored as a spectral cube. However, to study the spatial structure *clean* is used to create *multi-frequency synthesis* (MFS) maps which combines all channels into a single image taking into account properly the varying frequency.

Spectral Cubes

For the spectral line data, spectral cubes are created, which contain an image for every channel in the dataset. Measuring the flux density of each channel in a given region produces a spectrum, which allows us to determine channels containing line emission. The line channels are determined by first creating an approximate moment-0 map, by using the spectrum from a large aperture around the source. This moment-0 map is then used to create a new aperture and the spectrum is measured again. This dirty spectrum is then used to determine channels containing

line emission. We then cleaned these channels using the aperture as a mask to produce a clean cube.

To obtain line properties a profile was fitted to the spectrum. Line emission typically has a Voigt profile: the natural Gaussian profile caused by the fact that the velocity distribution is Maxwellian is convolved with a Lorentzian profile originating from collisions between the particles. Nonetheless, a simple Gaussian distribution will likely suffice as a first order approximation.

To fit the line, a simple Gaussian profile of the form

$$S(v) = A \exp \left[-\frac{1}{2} \left(\frac{v - \mu}{\sigma} \right)^2 \right] \quad (2.22)$$

was chosen. Using `scipy.optimize.curve_fit` a best fitting solution was found using the non-linear least squares method. From this fit we can determine a number of parameters. First of all the amplitude A of the fit is a measurement of the peak flux density of the line. The center and FWHM of the Gaussian give us the line's center velocity v_0 and linewidth Δv_{FWHM} . We can then use these parameters to obtain two other line related quantities: the line intensity and the line luminosity. The *line intensity* I_{CO} is measured in Jy km s^{-1} and is given by $A \times \Delta v_{\text{FWHM}}$. From the intensity we can then determine the *luminosity* in two ways as defined in [Solomon et al. 1992](#):

$$L'_{\text{CO}} = 3.25 \times 10^7 \times S_v \Delta v_{\text{FWHM}} \frac{D_L^2}{(1+z)^3 v_{\text{obs}}^2} [\text{K km s}^{-1} \text{ pc}^2] \quad (2.23)$$

and

$$L_{\text{CO}} = 1.04 \times 10^{-3} \times S_v \Delta v_{\text{FWHM}} D_L^2 v_{\text{obs}} [\text{L}_{\odot}]. \quad (2.24)$$

The former is used when estimating H_2 masses from CO emission, while the latter is a classical measure in solar luminosities of how strong the line is.

Besides MFS maps, the gas can also be studied using *moment maps*. Moment maps represent different quantities associated with the line emission. A moment-0 map is a velocity-weighted intensity map. Mathematically this would be expressed as an integral over velocity v :

$$M_0 = \int S(v) dv. \quad (2.25)$$

This give the line intensity I_{CO} . For the discrete channelized data, the integral changes into a sum. Each channel width Δv is converted into a velocity width Δv which is multiplied by the intensity in that channel. This is a way of determining I_{CO} directly from the data. Second and third order moments can also be taken to create velocity maps and dispersion maps. They are calculated by the following equations:

$$M_1 = \frac{\int v S(v) dv}{\int S(v) dv} \quad (2.26)$$

and

$$M_2 = \frac{\int (v - \langle v \rangle) S(v) dv}{\int S(v) dv}, \quad (2.27)$$

respectively. For higher order moments the signal-to-noise ratio needs to be higher as well.

Imaging and Visibility weighting

A measurement set contains SIGMA and WEIGHT columns

$$\text{SIGMA} = \begin{cases} \frac{1}{\sqrt{2\Delta\nu\Delta t}}, & \text{autocorrelations} \\ \frac{1}{\sqrt{\Delta\nu\Delta t}}, & \text{cross correlations} \end{cases} \quad (2.28)$$

where $\Delta\nu$ is the channel bandwidth and Δt the sample integration time. The WEIGHT is then determined as SIGMA^{-2} . Weights are used when averaging visibilities in either time or frequency or when creating an image, for example. This method results in equal weights for all visibilities as the sample time is usually the same throughout the entire observation. Instead, we chose to determine the weights differently based on the visibilities themselves. A script was made that looks at the variation in the visibilities of one baseline over the entire length of the observation. The spread in visibilities determined with `numpy.std` are then used as the SIGMA value and written back to the MS file with their corresponding WEIGHT values.

2.3 Herschel

Finally, we have used archival data from the Herschel Space Observatory. With its launch in 2009 we gained a new space observatory dedicated to infrared and sub-mm observations. The Herschel telescope comes with three instruments:

- The *Photodetector Array Camera and Spectrometer* (PACS) operating between 55 and 210 μm .
- The *Spectral and Photometric Imaging REceiver* (SPIRE) operating between 194 and 672 μm .
- The *Heterodyne Instrument for the Far Infrared* (HIFI) operating between 157-212 and 240-611 μm .

Its helium tanks has been depleted since 2013, but there is still work being done on reducing data and refining calibration⁴. Data collected with the Herschel telescope is still a wealth of information.

2.3.1 Observations and Data Reduction

Herschel observations were taken on June 03, 2011 with the SPIRE instrument at three different wavelengths, 250 μm , 350 μm and 500 μm , as part of a survey for debris disks around stars [Matthews 2007]. At these wavelengths, the 3.5 m dish achieves resolutions of 14.7", 20.6" and 29.5", respectively. These low resolutions mean our target is completely unresolved and possibly confused with other sources in the field. The total exposure time was 721 seconds. It was not necessary to reduce the Herschel data manually as everything is processed to good quality by the *Herschel Data Processing System*. Figure 2.33 shows one of the outputs by this system, showing

⁴<http://www.mpia.de/IRSPACE/herschel/>

the maps of the data. Our target is just to the right of the image center seen as a relatively bright blob. It is most apparent in the 500 μm image.

Herschel images are made from so called “timelines”. The detectors make scans across the target producing measurements of flux density as a function of time. These timelines correspond to what is called “level 1” data and is what is used to determine the flux density of the source. Using the `sourceExtractorTimeline` task in the *Herschel Interactive Processing Environment* (HIPE), a circular, two-dimensional Gaussian is fitted to the source. This fit is used to do photometry to obtain the flux-density. An additional uncertainty is introduced by the confusion limit, determined by [Nguyen et al. 2010](#) to be

$$\begin{cases} 5.8 \text{ mJy beam}^{-1}, 250 \mu\text{m} \\ 6.3 \text{ mJy beam}^{-1}, 350 \mu\text{m} \\ 6.8 \text{ mJy beam}^{-1}, 500 \mu\text{m} \end{cases} \quad (2.29)$$

for the SPIRE bands. MM18423+5938 fits in one beam, so these values correspond directly to the added uncertainty.

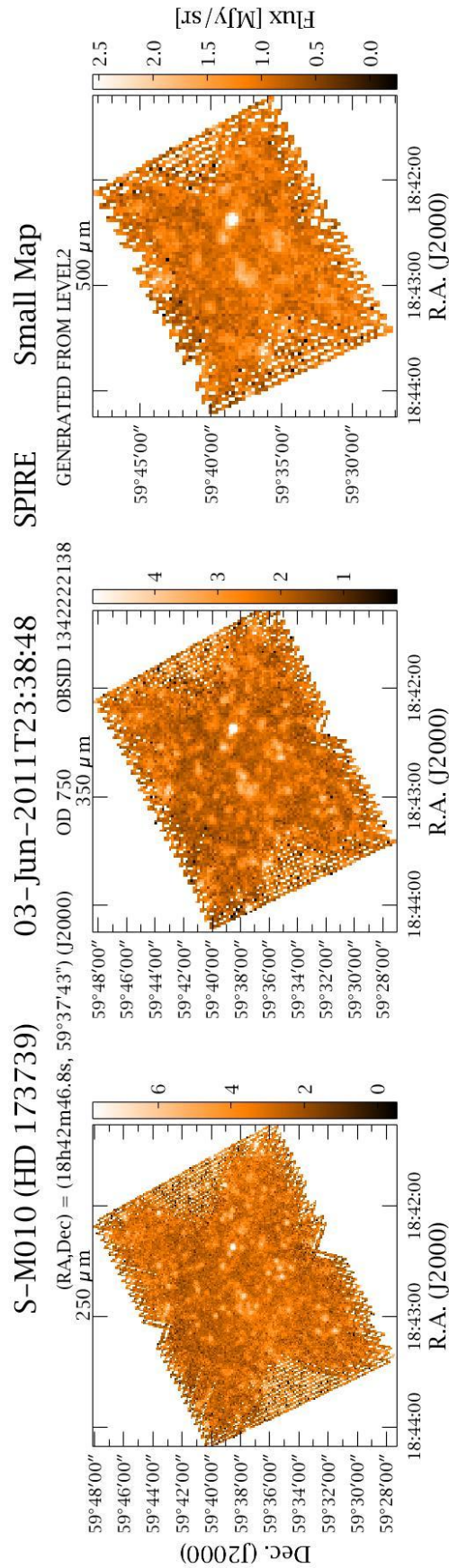


FIGURE 2.33: From left to right the 250 μm , 350 μm and 500 μm images as generated by the Herschel pipeline. MM18423 is the relatively bright blob just to the right of the image center. The 500 μm looks confused.

Chapter 3

Results

This chapter presents the results from the data reduction. The measurements of, for example, flux densities that will be presented in this chapter are lensed values. They are thus magnified by the lens. Despite this fact, it is still useful to do this analysis for multiple reasons. Measuring the flux density will give a rough idea of how bright the source is compared to other sources on the sky, for example. By looking at the shape of the lensed images we can get a preliminary idea of the structure of the object and the lens as well. There can be hints present on whether we are looking at extended structure or compact structure.

3.1 1.1 μm Emission

From the HST data the system can be identified as having an elliptical galaxy as the lens with three relatively easily identified possible images around it and possibly a fourth image on the lower right. The odd number theorem in gravitational lensing dictates that above two the number of images must be odd. Also expected is a central strongly demagnified image that is typically not observable. One would thus expect to observe either two, four or more images. Figure 3.1 shows a zoomed-in view of the source region. Analyzing this image has proven to be difficult. At first glance the lensing galaxy appears to be an elliptical.

Using the CASA viewer, we put the scaling power cycles to -5 (more power to low brightness structure) and started stretching the colorscale and contrast of the image in different ways. First we focussed on the lensing galaxy. It has an angle of

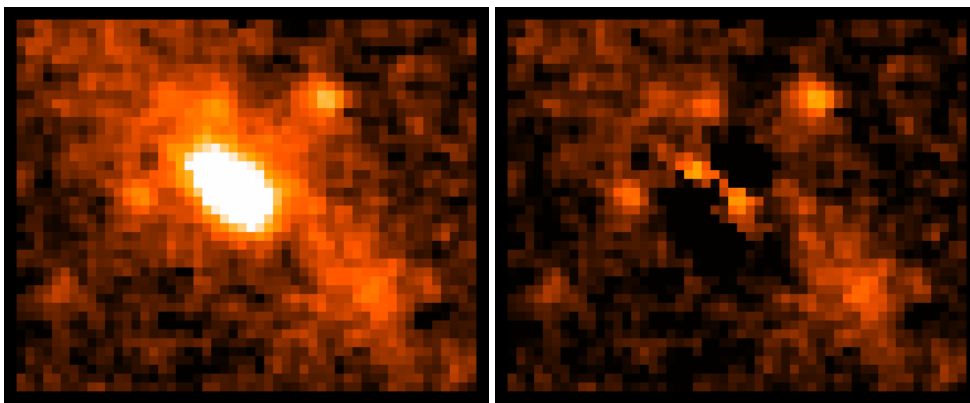


FIGURE 3.1: A zoomed in view of the target (*left*) and residuals after fitting for the central galaxy (*right*).

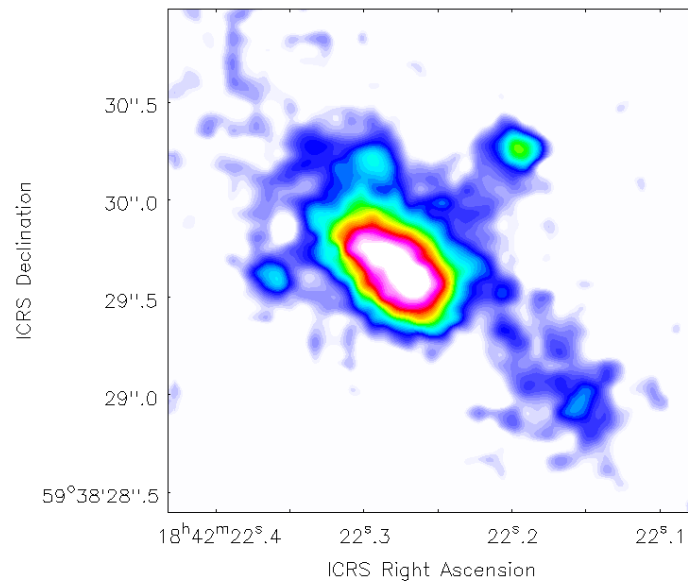


FIGURE 3.2: A view of the lens system with colors and contrast stretched to better see details. North is up, with east to the left. The lensing galaxy in the center shows evidence of consisting of two components. Possibly, the source is quadruply imaged. Only the east and north-west images are confirmed on radio maps from continuum and CO emission however.

49.74° east of north. In Fig. 3.2, we see evidence that this is not a simple elliptical galaxy. It is asymmetric with two components, possibly two galaxies interacting with each other. Such an interaction would disturb the dark matter halo which will make a lens model more complex. There is also a hint of diffuse extended emission around the object, which due to the interacting nature of the lens makes interpreting whether this emission is in the lens plane or source plane difficult.

Looking at this image, it is also difficult to assess what kind of image formation we are looking at, depending on how much one believes the possible images. Four possible images can be identified. Their distances from the center of the lensing galaxies are 1.19'', 0.87'', 0.56'' and 0.63'' for the south-west, north-west, north and east image, respectively.

It could be argued that we are seeing a quadruply imaged source if we believe the top three images to be real. The east and north-west images are both separated by 0.77'' from the north image, while the east and north-west images themselves are separated by 1.4''. If these are indeed three images, then a fourth counter image would be expected, which might be the emission seen south-west of the lensing galaxy. It is located at 1.7'', 1.66'' and 1.34'' from the east, north and north-west images, respectively. Despite being difficult to assess the situation, this can be tested with lens modeling.

Another possibility is that the north and south-west emission is associated with the lensing galaxies. They could be remnants from an interaction between two galaxies. Comparing the HST imaging with radio data at 5 GHz and CO emission (see the coming sections), gives further indication that the system may just be doubly imaged. We can only confirm the image pair formed by the east and north-west images. The other two spots do not show up on the radio maps.

3.2 5 GHz Radio Continuum Emission

With 5 GHz observations we are tracing the ~ 25 GHz rest-frame emission. This is likely synchrotron emission produced by electrons accelerated by supernova explosions [Casey et al. 2014; Harwit and Pacini 1975]. Synchrotron emission follows a powerlaw relation

$$S_\nu \propto \nu^\alpha \quad (3.1)$$

where α is the *spectral index*. Measuring the 5 GHz flux will add a second point to the SED of this power law allowing us to determine the spectral index. Currently only one measurement for this is available, made by McKean et al. 2011. Different weightings were tried for imaging: natural weighting, robust weighting (with robust=1 and 0) and uniform weighting. Natural weighting at one end gives the highest sensitivity while uniform weighting at the other end gives somewhat higher resolution at the cost of sensitivity. Using robust=0 or uniform weighting does not yield useable results. Figure 3.3 shows the dirty and clean images. Natural weighting gives a dirty image with an image noise of $\sigma_{\text{RMS}} = 4.4 \mu\text{Jy beam}^{-1}$ and a beam size of $0.65'' \times 0.45''$ with a position angle of -79.76° . Robust=1 gives $\sigma_{\text{RMS}} = 4.4 \mu\text{Jy beam}^{-1}$ and a beam size of $0.60'' \times 0.41''$ with a position angle of -80.24° . In the proposal the expected map noise using natural weighting is $\sim 3.2 \mu\text{Jy}$ (i.e. the thermal noise). We have not reached the thermal noise in our images, but we are close. This is likely the result of some remaining calibration errors attributable to the fact that self calibration was not done. We will now continue with natural weighting as this most likely catches more of the emission.

We measured the flux density in the images by creating a mask in CASA and selecting only data above a certain multiple of the map noise. These masks were made for the $2\sigma_{\text{RMS}}$ and $3\sigma_{\text{RMS}}$ levels. After applying the masks only emission brighter than this is left; this is shown in Fig. 3.4. Measuring the flux density we find

$$S_{5\text{GHz}}^{2\sigma_{\text{RMS}}} = 58.9 \pm 15.2 \mu\text{Jy} \quad \text{and} \quad S_{5\text{GHz}}^{3\sigma_{\text{RMS}}} = 23.9 \pm 7.1 \mu\text{Jy}. \quad (3.2)$$

The calibration uncertainty was determined from the gain solutions. For each observation, the resulting calibration table is shown in Fig. 3.5. The extreme outliers aside, the largest scatter is seen in the 8th observation ranging between 1.1 and 1.35. This is 0.25 scatter on an average of 1.225, giving a calibration uncertainty of 20%.

Next, the data was tapered to $0.5''$ and $1.0''$, to test if we are resolving out flux. Tapering will sacrifice resolution, in order to become more sensitive to extended emission, because more weight is given to the shorter baselines. Going to higher tapers will push the weighting more and more to shorter baselines. The difference in flux density from $0.5''$ to $1.0''$ is within each other's uncertainties and hence not significant. The resulting maps and their corresponding 2 and $3\sigma_{\text{RMS}}$ regions are shown in Fig. 3.6. Table 3.1 summarizes the measured flux densities for untapered, a $0.5''$ taper and a $1.0''$ taper. I will take the $2\sigma_{\text{RMS}}$ measurement of the image with a $0.5''$ taper, finding

$$S_{5\text{GHz}} = 74.2 \pm 18.8 \text{ mJy} \quad (3.3)$$

as the most reliable measure of the flux density as it contains most of the source's emission. Tapering the data increases the flux density. From this we can tell that most of the emission comes from a compact region, but there is an extended component to the radio emission that is resolved out at higher resolution.

Interestingly and contrary to the $1.1 \mu\text{m}$ emission, we identify only two images in the radio continuum emission. This could indicate that the radio emission is spatially

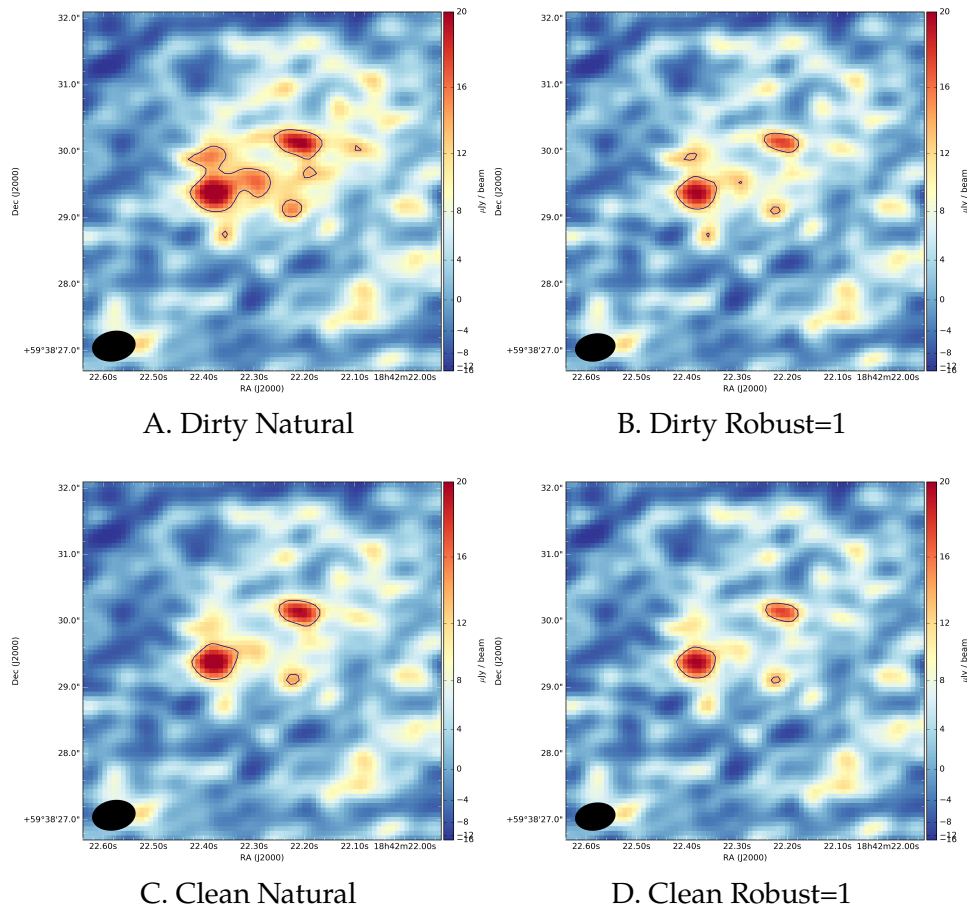


FIGURE 3.3: Dirty (*top row*) and cleaned (*bottom row*) images using natural (*left*) and robust=1 (*right* weighting). A color scale with a power law stretch ranging from $-16 \mu\text{Jy beam}^{-1}$ (*blue*) to $20 \mu\text{Jy beam}^{-1}$ (*red*) is used. The black ellipse represents the beam and solid black lines are $3\sigma_{\text{RMS}}$ contours with $\sigma_{\text{RMS}} = 4.4 \mu\text{Jy beam}^{-1}$. The images are 256×256 pixels with a scale of $0.07'' \text{ pixel}^{-1}$.

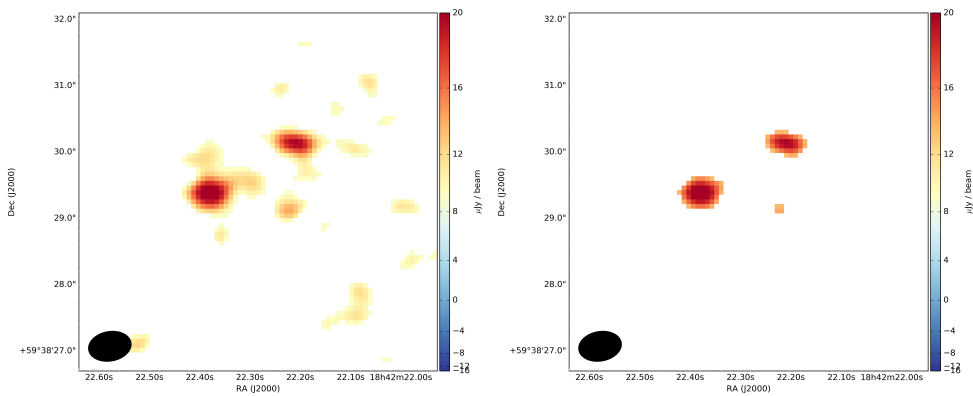


FIGURE 3.4: The natural weighted 5 GHz maps after applying the $2\sigma_{\text{RMS}}$ and $3\sigma_{\text{RMS}}$ masks (*left and right* respectively).

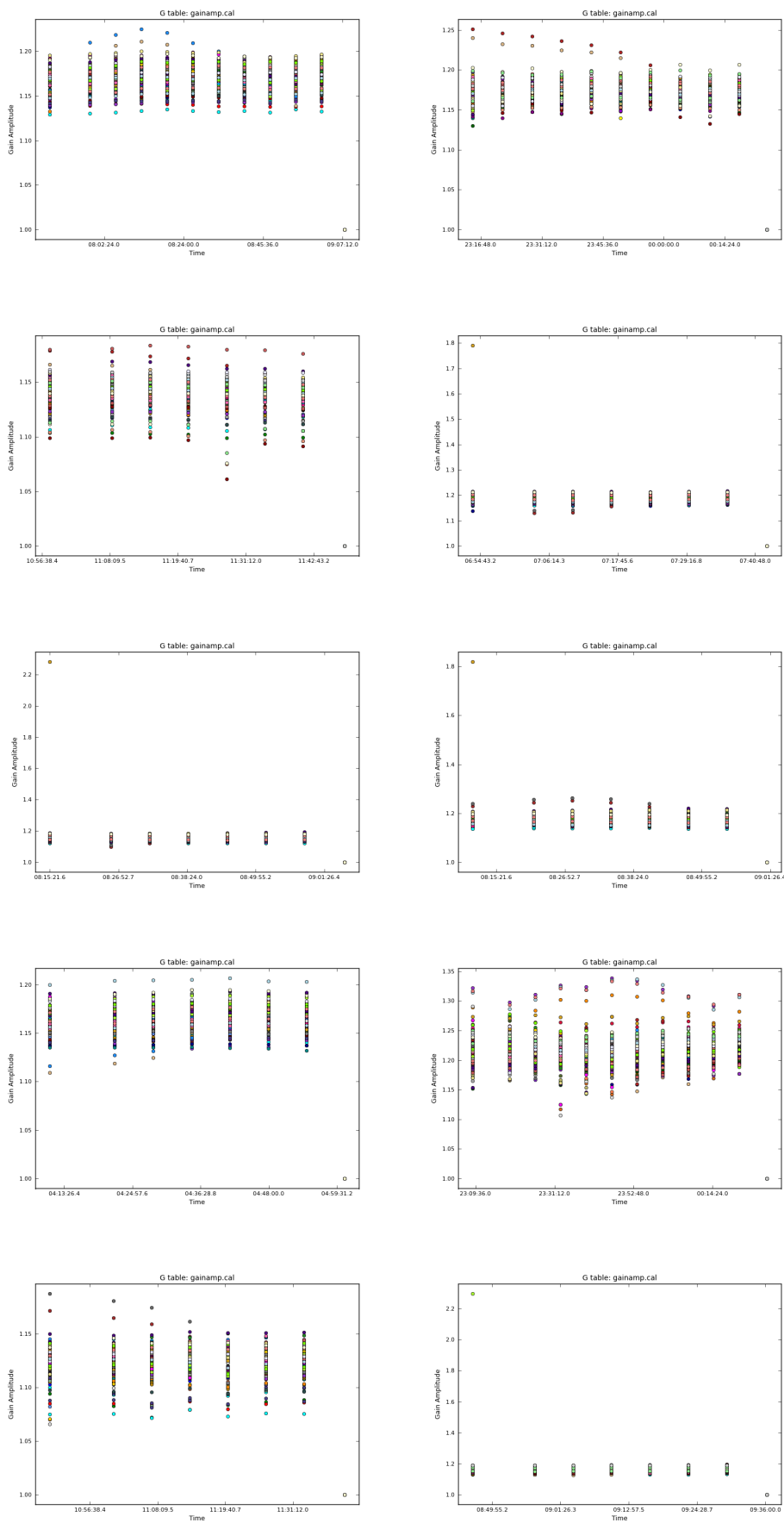


FIGURE 3.5: The gain amplitude calibration tables of the flux calibrator for each of the ten observations. Plotted in each plot is amplitude vs. time for each antenna.

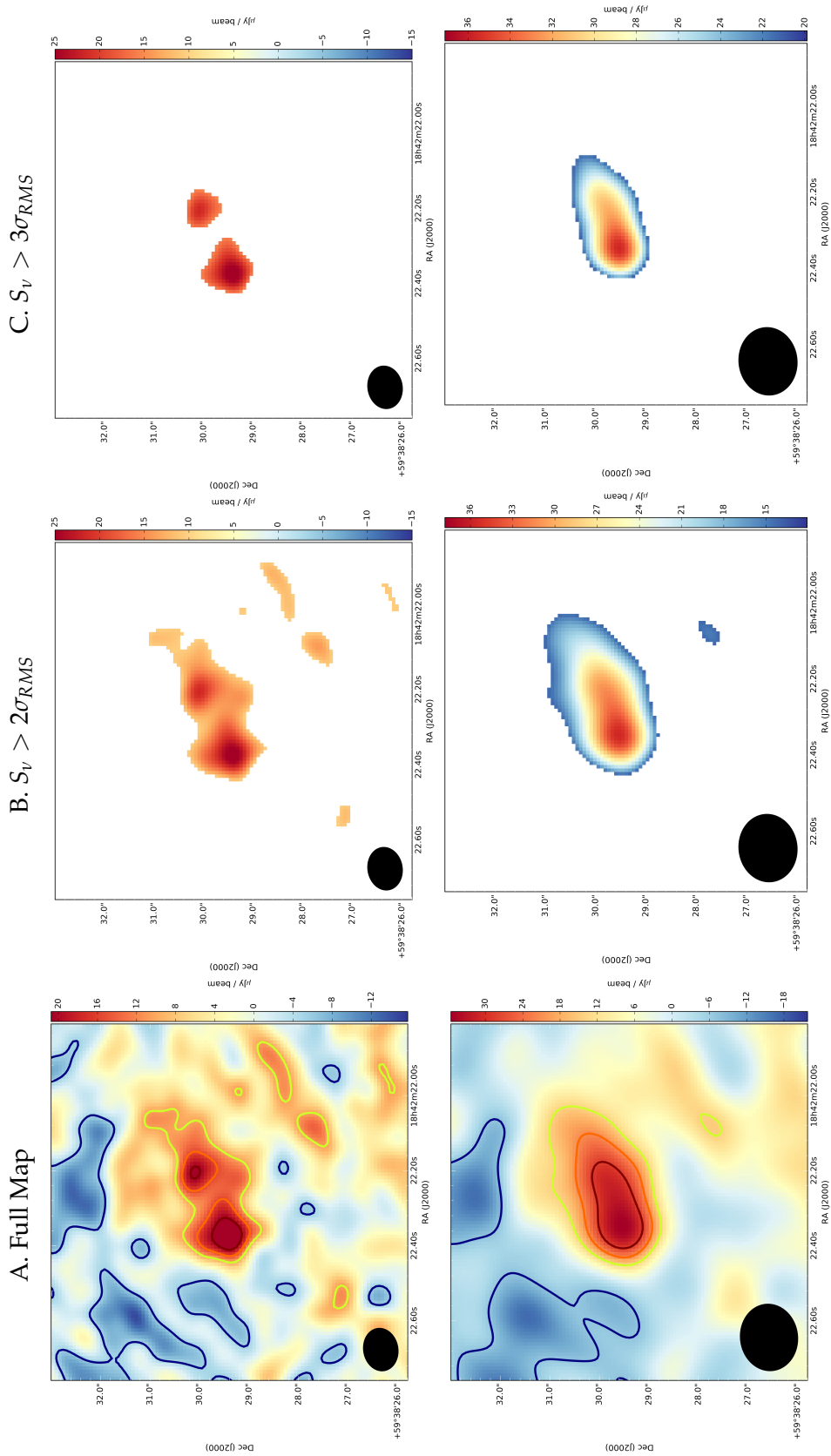


FIGURE 3.6: *Top row*: 5 GHz emission maps with a $0.5''$ taper applied, giving a beam of $0.87'' \times 0.70''$; -80.22° and a map noise of $\sigma_{RMS} = 5.2 \mu\text{Jy beam}^{-1}$. *Bottom row*: 5 GHz emission maps with a $1''$ taper applied, giving a beam of $1.35'' \times 1.16''$; -83.19° and a map noise of $\sigma_{RMS} = 7.1 \mu\text{Jy beam}^{-1}$. The contours are $-\sigma_{RMS}$ (black), $2\sigma_{RMS}$ (green), $3\sigma_{RMS}$ (red) and $4\sigma_{RMS}$ (brown) levels.

		No taper	0.5'' taper	1.0'' taper
Flux Density ($2\sigma_{RMS}$)	[μJy]	58.9 ± 15.2	74.2 ± 18.8	65.5 ± 17.7
Flux Density ($3\sigma_{RMS}$)	[μJy]	23.9 ± 7.1	34.0 ± 9.7	43.0 ± 12.3

TABLE 3.1: Measured flux densities and spectral indices for different tapers at $2\sigma_{RMS}$ and $3\sigma_{RMS}$ confidence. The value in bold indicates the measurement assumed to be most accurate physically.

at a different location in the galaxy than the NIR emission and located outside a cusp. It could also mean that the system as a whole is only doubly imaged. Measuring the flux density within the $3\sigma_{RMS}$ contours in the *untapered* MFS map, we measure $S_E = 14.1 \pm 4.9 \mu\text{Jy}$ and $S_{NW} = 9.7 \pm 3.9 \mu\text{Jy}$ for the north-west and east images, respectively. This gives a flux ratio of $\frac{S_{NW}}{S_E} = 0.77$. Doing the same for the 0.5'' tapered image yields $S_E = 24.4 \pm 7.6 \mu\text{Jy}$ and $S_{NW} = 11.1 \pm 4.6 \mu\text{Jy}$, giving a flux ratio of $\frac{S_{NW}}{S_E} = 0.45$. Lensing conserves surface brightness, hence the east image is more strongly magnified than the south-west image. The two images are separated by $\sim 1.4''$.

3.3 Molecular Line Emission

Observations with the K and Q bands of the VLA trace molecular emission of CO in this object, specifically the CO(1-0) and CO(2-1) transitions where the molecule de-excites from the $J = 1$ to $J = 0$ or $J = 2$ to $J = 1$ rotational levels, respectively. The $J = 1$ state is a low excitation state having an excitation potential of 5.5 K while the $J = 2$ has a slightly higher excitation potential of 16.6 K [Carilli and Walter 2013]. These states are mainly populated by collisional excitation through collisions between CO and H_2 and therefore emission from this molecule is a good tracer for molecular hydrogen (H_2) gas used to form stars. With CO(1-0) cold, extended gas reservoirs are traced while CO(2-1) traces somewhat warmer, more compact gas reservoirs. In Tab. 3.2 the line channels in which the CO transitions were detected is listed for the different array-configurations.

3.3.1 The CO(1-0) Transition

We show data from B-array and D-array observations of this line. The resolutions (λ/D) are $0.23''$ and $2.57''$, respectively. Imaging cell sizes were therefore chosen to be $0.05''$ and $0.5''$ in order to properly sample the psf. The calibration uncertainty for the K-band was determined to be on the order of 1%. There is no evidence for significant continuum emission in either the B-array or D-array observations. Furthermore, continuum emission is estimated to be $S_{23.4\text{GHz}} = 22.6 \mu\text{Jy}$, based on

Project Code	Array	Band	Line Channels	Velocity
11B-002	D	Q	5:16~46	$115.8 \sim -140.6 \text{ km s}^{-1}$
11B-002	B	Q	5:20~38	$154.3 \sim -76.5 \text{ km s}^{-1}$
10B-245	C	Q	0:47~63, 1:0~15 ^a	$190.8 \sim -181.0 \text{ km s}^{-1}$
11B-002	B,D	K	5:27~37	$129.2 \sim -127.2 \text{ km s}^{-1}$

TABLE 3.2: A summary of the line channels in each array configuration. (a): in this case the spectral windows had a 4 channel overlap, i.e. channels 0 : 60 ~ 63 overlap with 1 : 0 ~ 3.

Parameter		D-ARRAY	B-ARRAY	B-ARRAY+D-ARRAY
A	[mJy]	2.8 ± 0.3	2.9 ± 0.3	2.7 ± 0.3
v_0	[km s ⁻¹]	0.5 ± 9.9	-25.4 ± 5.1	-19.7 ± 8.7
σ_v	[km s ⁻¹]	74.3 ± 11.1	79.0 ± 11.5	79.1 ± 10.1
Δv_{FWHM}	[km s ⁻¹]	175.0 ± 26.1	186.0 ± 27.1	186.3 ± 23.8
I_{CO}	[Jy km s ⁻¹]	0.5 ± 0.1	0.5 ± 0.1	0.5 ± 0.1
L'_{CO}	[10 ¹¹ K km s ⁻¹ pc ²]	3.2 ± 0.6	3.2 ± 0.6	3.2 ± 0.6
L_{CO}	[10 ⁷ L _⊙]	1.6 ± 0.3	1.6 ± 0.3	1.6 ± 0.3

TABLE 3.3: Fit parameters for a Gaussian fit to the cleaned CO(1-0) emission line as seen in the D-array, B-array and combined data. The uncertainties are statistical uncertainties from the fit.

the radio spectral index. This is almost three times below the RMS in our channels, and hence will not influence the result.

D-array

For the D-array only one dataset was available. The spectrum from the clean cube is shown in Fig. 3.8 from which we determined channels 27~37 to contain line emission. Figure 3.9 shows the line channels with a Gaussian fit to the emission. The fit parameters are summarized in Tab. 3.3. We measure a total flux density in the D-array of

$$S_{(1-0)}^D = 1.6 \pm 0.2 \text{ mJy} \quad (3.4)$$

from the clean MFS map shown in Fig. 3.10. The synthesized beam is $3.19'' \times 2.58''$ with a position angle of -47.03° . Hence, with the D-array the source is an unresolved point source. A fit to the spectrum gives a line peak strength of

$$A^D = 2.8 \pm 0.3 \text{ mJy}. \quad (3.5)$$

This is higher than what is found by [Lestrade et al. 2011](#).

B-array

Figure 3.8 shows the spectrum obtained from the clean B-array cube. A Gaussian fit to the line is shown in Fig. 3.9 with the resulting line parameters listed in Tab. 3.3. Using $2\sigma_{\text{RMS}}$ contours as a guide (these follow the model best), we measure a flux density of

$$S_{(1-0)}^B = 1.6 \pm 0.1 \text{ mJy} \quad (3.6)$$

from the cleaned MFS map shown in Fig. 3.10. This is consistent with the measurement from the D-array. This time, the synthesized beam is $0.36'' \times 0.32''$ with a position angle of -36.22° , allowing us to resolve the system. Two, possibly three, compact components are identified to the east, north-west and south-west. The eastern image looks like it may be two merging images. In this case the CO would be quadruply imaged. There is also evidence some extended structure around the compact components. This can be seen around the merging images and to the south-east where there is a “tail” of emission. Seeing merging images tells us a more compact part is located near a fold, on the caustic.

Parameter		COMPONENT 1	COMPONENT 2
A	[mJy]	2.7 ± 0.3	0.8 ± 0.2
v_0	[km s ⁻¹]	-19.7 ± 8.7	-251.9 ± 16.7
σ_v	[km s ⁻¹]	79 ± 10	45 ± 27
Δv_{FWHM}	[km s ⁻¹]	186 ± 24	94 ± 64
I_{CO}	[Jy km s ⁻¹]	0.5 ± 0.1	0.08 ± 0.06
L'_{CO}	[10 ¹¹ K km s ⁻¹ pc ² μ ⁻¹]	3.2 ± 0.6	0.5 ± 0.4
L_{CO}	[10 ⁷ L _⊙ μ ⁻¹]	1.6 ± 0.3	0.3 ± 0.2

TABLE 3.4: Fit parameters for the two components identified in the clean cube, from combining B-array and D-array data.

Combining B-array and D-array

To get the most out of the data we also attempted to combine the B-array and D-array data in order to obtain a better spectrum. To this all datasets were passed along to CASA's clean task at the same time. We chose a *cell* parameter of 0.05'' to have proper sampling of the B-array data. To not resolve out too much of the D-array data we also tapered the data slightly to 0.3''. Combining B-array and D-array data covers the *uv*-plane on small and large scales, but not on intermediate scales. Although the combined *uv*-coverage is overall good (see Fig. 3.7A) the PSF resulting from this combination has strong sidelobes (see Fig. 3.7B) which is why cleaning is so important.

The synthesized beam is now 0.53'' × 0.48'', with a position angle of −48.05°. From the clean MFS map in Fig. 3.10 the additional data from the D-array observations reveals the CO to be in two arcs that comprise two compact components and a more diffuse component. Next the spectrum was cleaned, first by hand to create an initial clean moment-0. From this map a mask was made to cover the area in only the line channels. The cube was then cleaned non-interactively with a threshold of 80 μJy beam⁻¹, a little above the RMS noise. The resulting spectrum is shown in Fig. 3.8. Interestingly, a second component that [Lestrade et al. 2011](#) identified around −200 km s⁻¹, is possibly identified here as well, spanning four channels. Cleaning in these channels as well yields a result similar to that of [Lestrade et al.](#) for this component. A slightly higher amplitude was found, but overall it is consistent within the error bars. The results are listed in Tab. 3.4. We find a higher amplitude for the main emission line however.

Looking at the clean spectrum, we may even speculate the presence of a doubly peaked profile, which would indicate a rotating structure. Figure 3.11 shows the moment-0 map from the clean cube. Finally in Fig. 3.12 we show the channel maps of the clean cube with the moment-0 map contours overlaid.

Molecular Gas Mass

Having the luminosity L'_{CO} of the line emission we can make an estimate of the H₂ reservoir in MM18423+5938. The CO(1-0) emission and gas mass are linked by a conversion factor α_{CO}

$$M_{\text{gas}} = \alpha_{\text{CO}} L'_{\text{CO}}. \quad (3.7)$$

For the Milky Way this conversion factor has a value of $\alpha_{\text{CO}} = 4 M_{\odot} \text{ K}^{-1} \text{ km}^{-1} \text{ s pc}^{-2}$, but for starbursting systems such as ULIRGS this value drops to about 0.8 [[Carilli and Walter 2013](#); [Downes and Solomon 1998](#)]. Because DSFGs are intense star forming

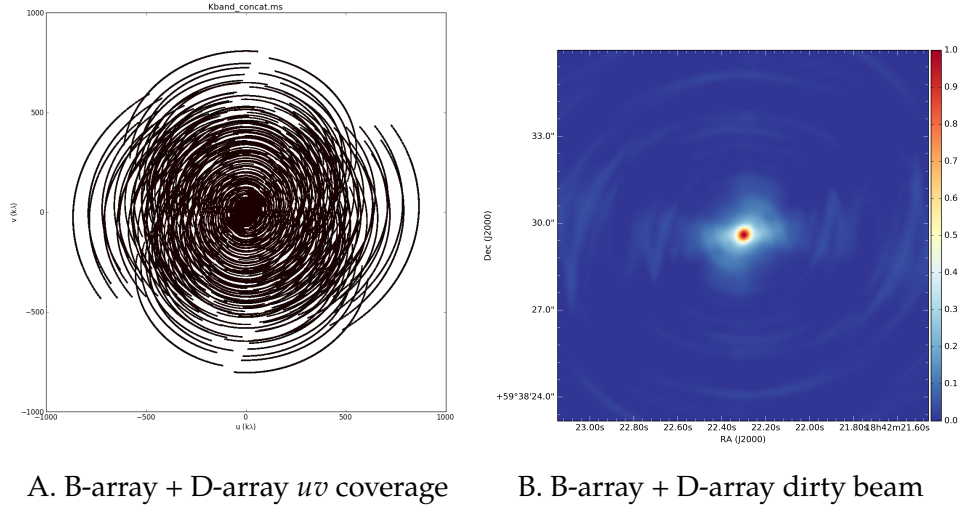


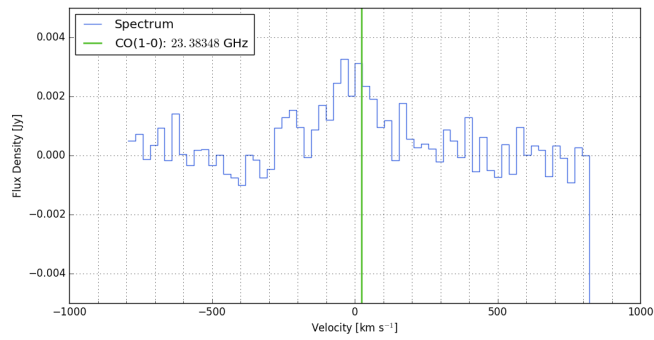
FIGURE 3.7: The uv coverage and dirty beam resulting from combining B-array and D-array data into a single data cube.

regions this conversion factor for them is also often assumed to be 0.8. From the clean spectrum we measure a line luminosity of $3.2 \pm 0.6 \times 10^{11} \text{ K km s}^{-1} \text{ pc}^2 \mu^{-1}$, where μ is the magnification. Using the above relation assuming $\alpha_{\text{CO}} = 0.8$ this implies a gas mass of

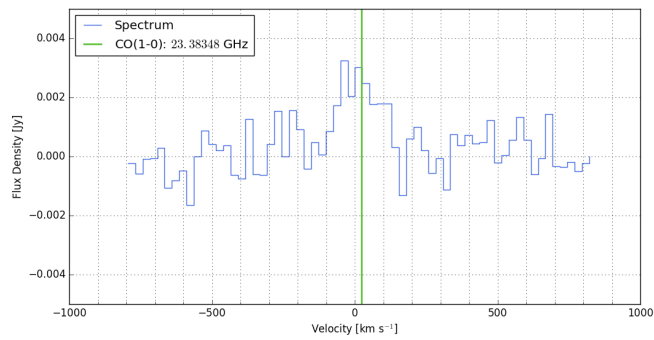
$$M_{\text{gas}} = 2.6 \pm 0.5 \times 10^{11} M_{\odot} \mu^{-1} \quad (3.8)$$

not yet corrected for magnification effects, consistent with [Lestrade et al. 2011](#), within the error bars. Assuming their magnification of $\mu \sim 12$ this comes down to

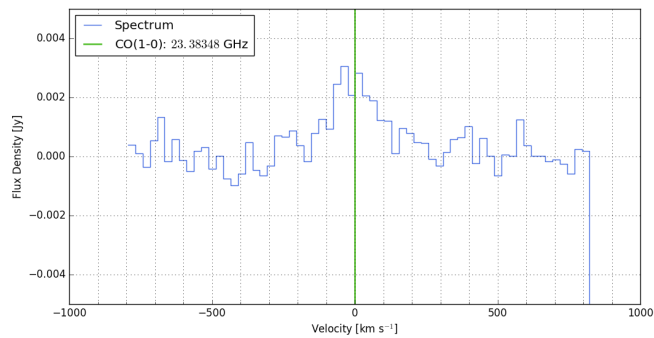
$$M_{\text{gas}} = 2.2 \pm 0.4 \frac{12}{\mu_{\text{CO}(1-0)}} \times 10^{10} M_{\odot}. \quad (3.9)$$



A. B-array

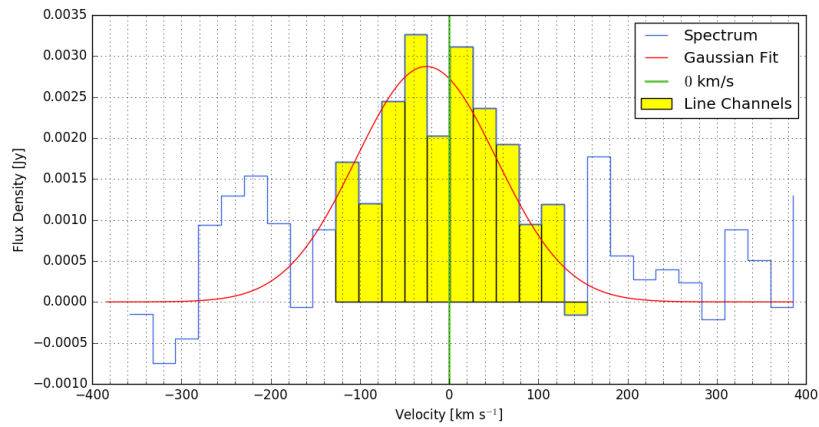


B. D-array

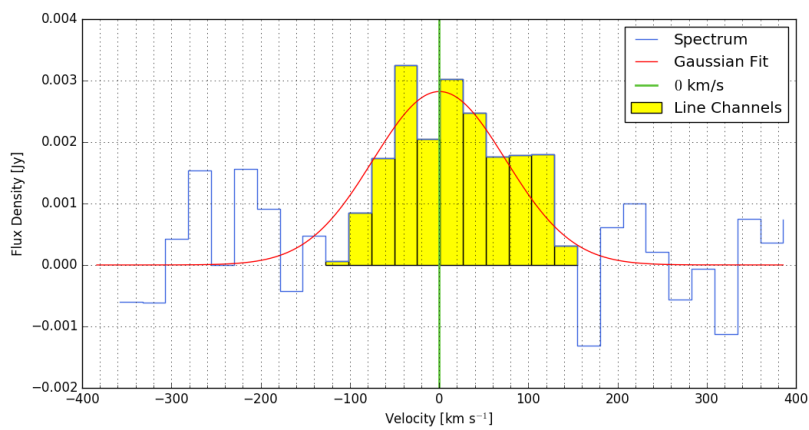


C. B-array + D-array; Cleaned

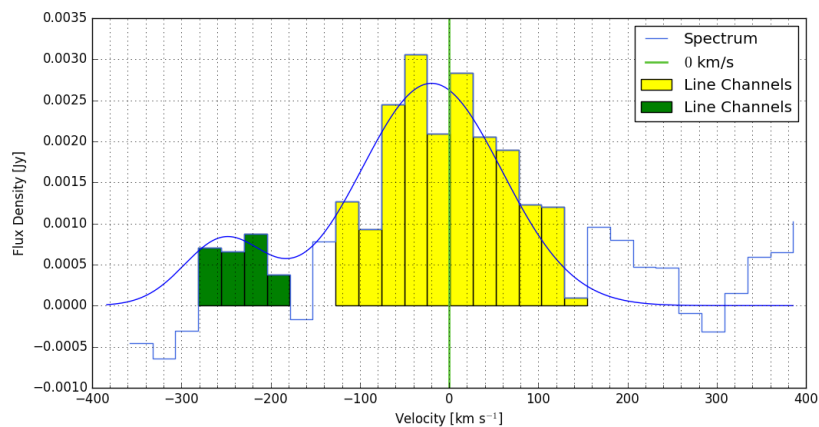
FIGURE 3.8: A B-array (*top*), D-array spectra (*middle*) and a stacked spectrum (*bottom*) of the CO(1-0) transition. The spectrum was taken from an aperture determined from the moment-0 maps. The green line indicates the rest frequency at the source's redshift.



A. B-array



B. D-array



C. B-array + D-array

FIGURE 3.9: The CO(1-0) emission line in the clean cubes, as detected in the B and D configurations of the VLA (*top two panels*). Yellow shading indicates the channels which were determined to contain line emission. The green line denotes the CO(1-0) rest frequency of 23.8348GHz corresponding to 0 km s^{-1} . Finally the red line is the best fitting Gaussian found from a least-squared fit to the data. The final panel shows the spectrum obtained from the clean cube combining B-array and D-array data.

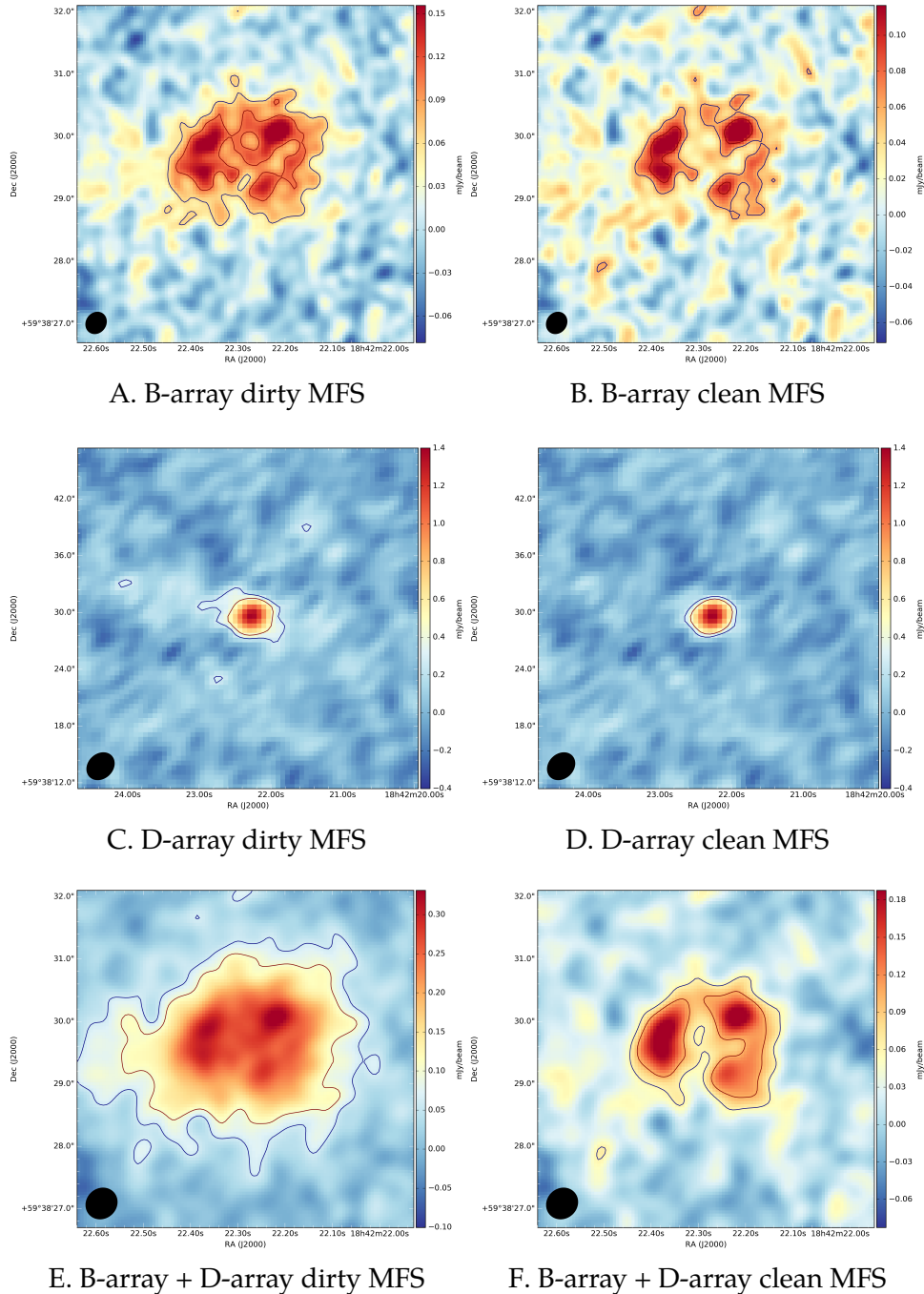


FIGURE 3.10: Dirty (*left*) and clean (*right*) MFS maps of the B-array (*top*) and D-array (*bottom*) data. The contours indicate the $3\sigma_{\text{RMS}}$ and $5\sigma_{\text{RMS}}$ levels which are (left to right, top to bottom) 20.9, 19.6, 90.5, 90.2, 20.7 and 20.8 $\mu\text{Jy beam}^{-1}$ respectively.

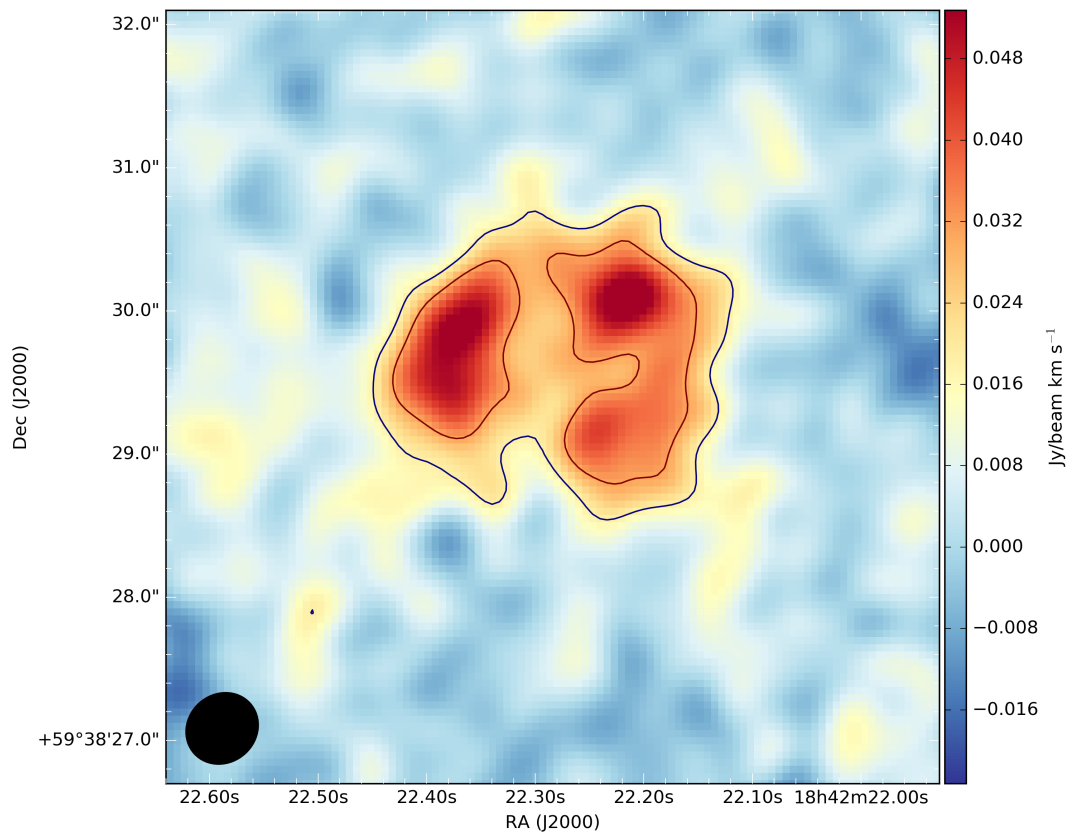


FIGURE 3.11: The velocity-weighted intensity map obtained from the clean cube combining B-array and C-array data. The contours indicate 3 and $5\sigma_{\text{RMS}}$ levels with $\sigma_{\text{RMS}} = 6.2 \text{ mJy km s}^{-1} \text{ beam}^{-1}$. The colorscale is in units of $\text{Jy km s}^{-1} \text{ beam}^{-1}$.

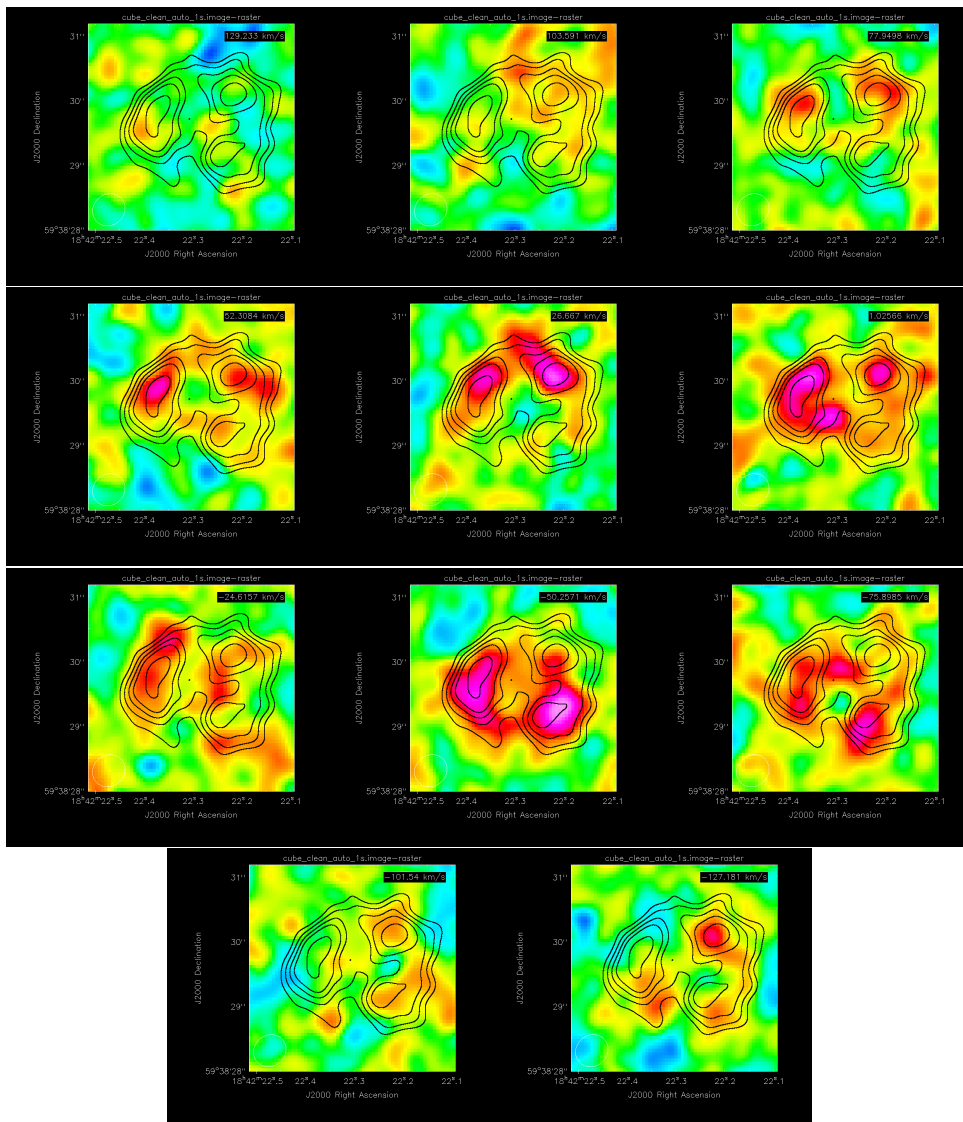


FIGURE 3.12: Channel maps from the clean cube combining B-array and D-array data. The channels run from 129.2 km s^{-1} (top left) to -127.2 km s^{-1} (bottom right), with a channel width of 25.6 km s^{-1} . In black, 3, 4, 5, 6 and $8\sigma_{\text{RMS}}$ contours of the moment-0 map are shown.

3.3.2 The CO(2-1) Transition

For the CO(2-1) transition, the data for three array configurations were analyzed: D-array, C-array and B-array. This results in spatial resolutions of 0.12", 0.39" and 1.28", respectively. For imaging the cell sizes were 0.03" pixel⁻¹, 0.08" pixel⁻¹ and 0.3" pixel⁻¹, respectively. For determining the flux density of the line, in principle the D-array data is most useful as this is where the source is least resolved spatially. In this case however this data had the shortest effective observation time due to not being able to use two of the three datasets. The 2 MHz channels result in a velocity resolution of 12.8 km s⁻¹. The calibration uncertainty was determined to be 2%, 5% and 5% for the D, C, and B-array, respectively.

D-array

Comparing the D-array data to the other datasets we notice an additional offset from the phase center. This is probably a pointing error. Without knowing an accurate shift to compensate this error the D-array data cannot be combined with the other datasets.

The cube was cleaned with a threshold of 2 mJy beam⁻¹, slightly above the RMS channel noise. Figure 3.19 shows the spectra obtained from the clean cube. The D-array data was both analyzed at its native resolution of 2 MHz (12.8 km s⁻¹) and binned, by 3 channels (38.4 km s⁻¹). From the unbinned spectrum 31 channels (16 through 46) were selected as being "line channels" spanning a total of 62 MHz or 396.8 km s⁻¹. From the binned spectrum, 20 channels (5 through 24) were selected as being line channels spanning a total of 80 MHz or 512.8 km s⁻¹. The per-channel noise was 2 mJy beam⁻¹ and 1 mJy beam⁻¹, respectively.

There is no indication for significant continuum emission coming from the source at this frequency. We estimate $S_{46.7\text{GHz}} = 13.0 \mu\text{Jy}$, using the radio spectral index. Hence, if there is continuum emission it is expected around the $\sim 10 \mu\text{Jy}$ level, which is not detectable nor influential given our noise floor.

The results of fitting a Gaussian profile to the line are shown in Fig. 3.20. Table 3.5 summarizes the line parameters obtained from the fit. Binning channels yields results that are consistent with the unbinned data. We measure a higher amplitude, but both are consistent with the measurement by [Lestrade et al. 2011](#) within 1.5σ . It is likely that we have not cleaned deep enough as the RMS noise in the channels is of the order of 10% of the line's peak flux density.

C-array

These data are the same as presented in [Lestrade et al. 2011](#). We reduced it ourselves to have it be consistent with the other datasets and to give us a starting point for the lens modeling. Figure 3.19 shows the spectra of the unbinned and binned data respectively. Due to more time on target compared to the D-array data, the signal-to-noise ratio is much higher. The line is clearly detected. A clean MFS map of the line channels is shown in Fig. 3.21. We see the emission forms an Einstein ring, with two brighter spots to the south-west and north-east. They are separated by about 1.5".

For the C-array we find the line spanning 31 channels (46 \sim 76; 397.4 km s⁻¹) in the unbinned case and 19 channels (22 \sim 40; 487.2 km s⁻¹) in the binned case. Gaussian fits to both spectra are shown in Fig. 3.20. Interestingly the detection in the C-array shows a hint of a doubly peaked profile. This double peak was not reported by [Lestrade et al. 2011](#). Even if we bin the data by two channels (to match their spectrum) we still see the doubly peaked profile. Since we are using the same

Parameter		D-array	C-array	B-array
<i>Unbinned</i>				
A	[mJy]	12.4 ± 1.5	8.0 ± 0.7	7.6 ± 1.1
v_0	[km s ⁻¹]	-6.7 ± 13.1	-11.2 ± 9.3	12.5 ± 12.6
σ_v	[km s ⁻¹]	94.8 ± 12.4	92.3 ± 9.8	71.8 ± 14.9
Δv_{FWHM}	[km s ⁻¹]	223.3 ± 29.2	222.0 ± 23.2	169.2 ± 35.1
I_{CO}	[Jy km s ⁻¹]	2.8 ± 0.5	1.7 ± 0.3	1.3 ± 0.3
L'_{CO}	[10 ¹¹ K km s ⁻¹ pc ⁻²]	4.5 ± 0.8	2.7 ± 0.5	2.1 ± 0.5
L_{CO}	[10 ⁸ L _☉]	1.8 ± 0.3	1.1 ± 0.2	0.8 ± 0.2
<i>Binned</i>				
A	[mJy]	11.9 ± 1.8	7.6 ± 1.0	7.9 ± 1.4
v_0	[km s ⁻¹]	-5.9 ± 16.9	-8.6 ± 13.8	14.4 ± 14.2
σ_v	[km s ⁻¹]	97.5 ± 17.8	93.9 ± 14.0	66.8 ± 15.9
Δv_{FWHM}	[km s ⁻¹]	229.6 ± 41.9	221.1 ± 33.0	157.3 ± 37.4
I_{CO}	[Jy km s ⁻¹]	2.7 ± 0.6	1.7 ± 0.3	1.2 ± 0.3
L'_{CO}	[10 ¹¹ K km s ⁻¹ pc ⁻²]	4.3 ± 1.0	2.7 ± 0.5	1.9 ± 0.5
L_{CO}	[10 ⁸ L _☉]	1.7 ± 0.4	1.1 ± 0.1	0.8 ± 0.2

TABLE 3.5: Fit parameters and derived quantities obtained from the clean spectra of the D-array, C-array and B-array. Uncertainties indicate statistical uncertainties of the fit. The D-array flux densities are likely overestimated due to high channel noise.

data this only leaves the calibration and cleaning as differences. We also do not identify a second component to the line. Our per-channel rms noise is slightly lower, $0.3 \text{ mJy beam}^{-1}$ against $0.48 \text{ mJy beam}^{-1}$.

As the line is well detected in this case we, attempted to see if there is velocity structure by separately imaging the “red” and “blue” part of the line. If they are spatially different from each other, that might be an indication for rotation. In this context this means the lower frequency peak for the red part and the higher frequency peak for the blue part. For the C-array data we could split the data with $0 : 47 \sim 63$; $190.8 \sim -14.3 \text{ km s}^{-1}$ as the red part and $1 : 0 \sim 15$; $-27.1 \sim -168.1 \text{ km s}^{-1}$ as the blue part each being approximately 200 km s^{-1} . The respective channels were first split into separate MS files. These were then imaged and cleaned before being exported to FITS files. Using DS9 they were assigned to red and blue respectively to create a composite image. The resulting image is shown in Fig. 3.13. Where for the display settings a contrast of 5 and a bias of 0.75 was chosen. It can be seen that we can identify an approaching and a receding part of the source, indicating there may be rotation present in MM18423. An attempt was made to fit this double horn profile with two Gaussians, but this was unsuccessful, which is not surprising as a double horn profile generally is not simply two gaussians. To go one step further we split the line in three parts: red ($0 : 47 \sim 57$; $190.8 \sim 62.2 \text{ km s}^{-1}$), green ($0 : 57 \sim 63$, $1 : 0 \sim 4$; $62.2 \sim -65.6 \text{ km s}^{-1}$) and blue ($1 : 5 \sim 15$; $-78.4 \sim -168.1 \text{ km s}^{-1}$) each containing 11 channels of line emission translating to approximately 120 km s^{-1} . We show the result in Fig. 3.14. Again, this is a hint for a rotating structure as they are spatially offset. The red part would have a velocity moving away from us along our line of sight, the green part a velocity roughly perpendicular to our line of sight and the blue part a velocity towards us along our line of sight.

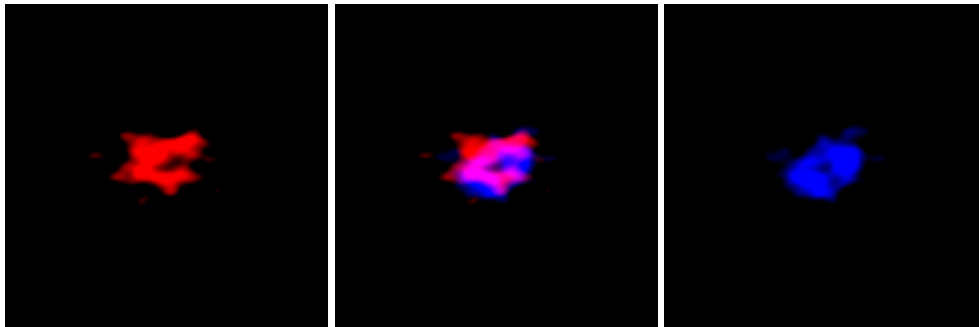


FIGURE 3.13: The red and blue parts of the line imaged separately and color coded to their respective regime. *Left*: channels 0 : 47 ~ 63 representing the “red” part of the spectrum. *Middle*: the red and blue parts overlaid on top of each other. *Right*: channels 1 : 0 15 the “blue” part of the line.

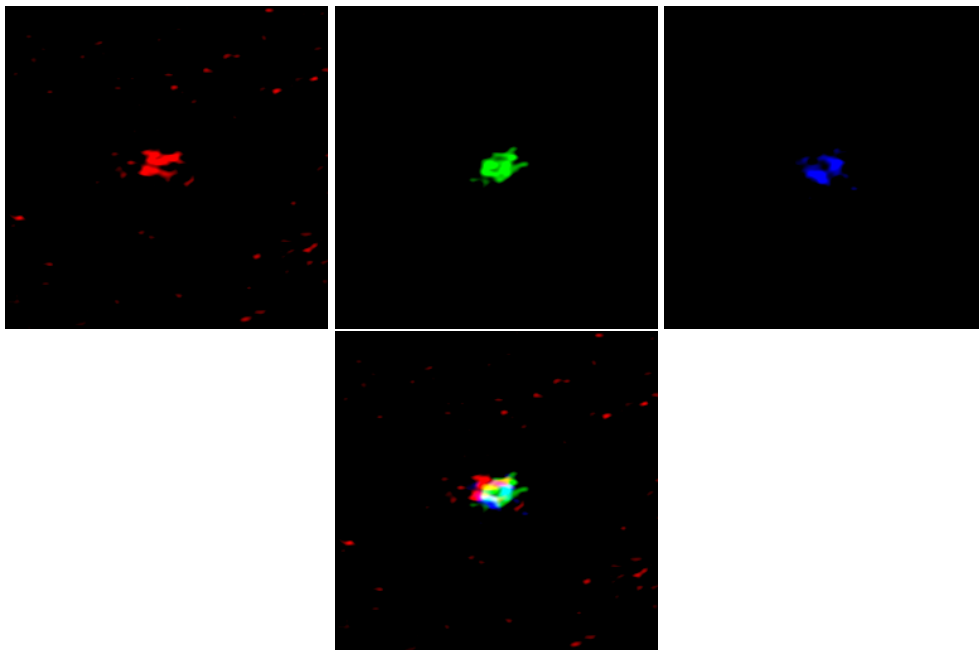


FIGURE 3.14: The CO(2-1) emission line as observed in the C-array split into red, green and blue (*top row*) and displayed on top of each other (*bottom*). This may be evidence for a rotating structure.

B-array

Finally we analyze the highest resolution data from B-array observations. The targeted emission line is marginally detected just above the noise level. Figure 3.19 shows the spectra obtained from the unbinned cube and a spectrum obtained by binning every 2 channels. From these spectra we identify channels 20 \sim 38 (243.6 km s⁻¹) and 10 \sim 19 (256.4 km s⁻¹) to contain line emission in the unbinned and binned case respectively. We then again attempted to fit a Gaussian line profile to the emission. The resulting fits are shown in Figures 3.20 with the corresponding fit parameters being summarized in Tab. 3.5. The linewidth is significantly smaller, because the diffuse emission is significantly resolved out.

In the individual channels, it is difficult to identify any source components and this remains the case even for the MFS and moment-0 maps which average all line channels together. In Fig. 3.21 we show a clean MFS map of the unbinned data. All but the most compact of the emission is resolved out.

Combining B-array and C-array

Due to the misalignment of the D-array data, they cannot be combined with the other datasets. We can, however, combine the B-array and C-array data. The spectrum was cleaned non-interactively by setting a mask determined from a dirty moment-0 map, using a threshold of 0.50 mJy beam⁻¹ (a little above the RMS noise) and with a 0.3'' taper to conserve the extended emission picked up in the C-array. The resulting beam was 0.65'' \times 0.51'' with a position angle of -85.16° . This resulted in the clean spectrum presented in Fig. 3.15. We continue to see the double peak profile. In Fig. 3.18 we show channel maps for the line channels. They do not show evidence of ordered rotation, with structure appearing and disappearing irregularly. A Gaussian fit to the emission is shown in Fig. 3.16. The emission was determined to span channels 47 \sim 76, i.e. 190.8 \sim -180.9 km s⁻¹. The resulting fit parameters are shown in Tab. 3.6. They do not agree with the findings by [Lestrade et al. 2011](#), being significantly lower.

In Fig. 3.17 we see the moment-0 map from this clean cube. An almost complete Einstein ring can be identified, with two bright spots separated by 1.6''. Seeing such an arc indicates that the CO is extended. The two peaks are more compact regions of gas.

Tapering to 0.1'' lowers the peak flux density of the line even further, resolving out much of the diffuse emission with a beam of 0.34'' \times 0.31'', having a position angle of -65.70° . A moment-0 map is presented in Fig. 3.17, where we see most of the diffuse emission is resolved out.

Parameter		Value
A	[mJy]	7.8 ± 0.6
v_0	[km s ⁻¹]	-6.8 ± 8.1
σ_v	[km s ⁻¹]	91.3 ± 8.6
Δv_{FWHM}	[km s ⁻¹]	215.0 ± 20.3
I_{CO}	[Jy km s ⁻¹]	1.7 ± 0.2
L'_{CO}	[10 ¹¹ K km s ⁻¹ pc ²]	2.7 ± 0.3
L_{CO}	[10 ⁸ L _⊙]	1.1 ± 0.1

TABLE 3.6: Fit parameters obtained from a Gaussian fit to the clean spectrum.

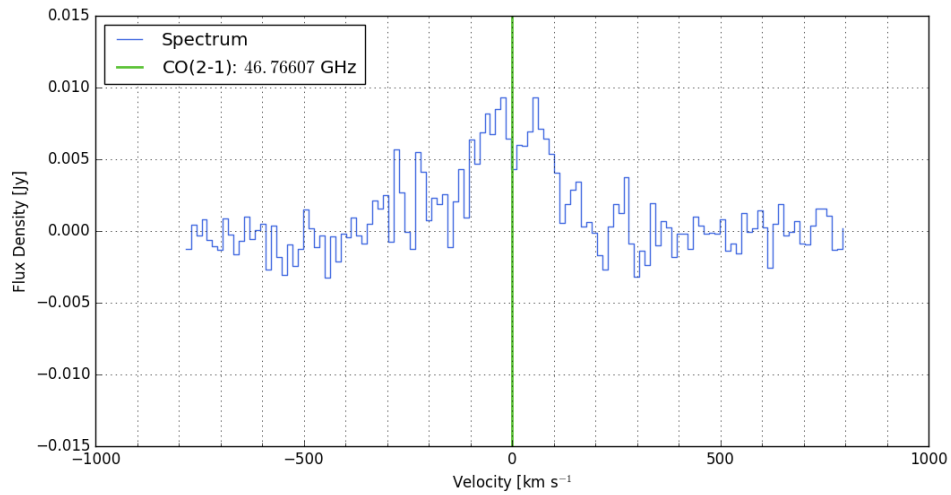


FIGURE 3.15: The spectrum obtained from the clean cube, combining B-array and C-array data. The spectrum was taken from an aperture based on the moment-0 map.

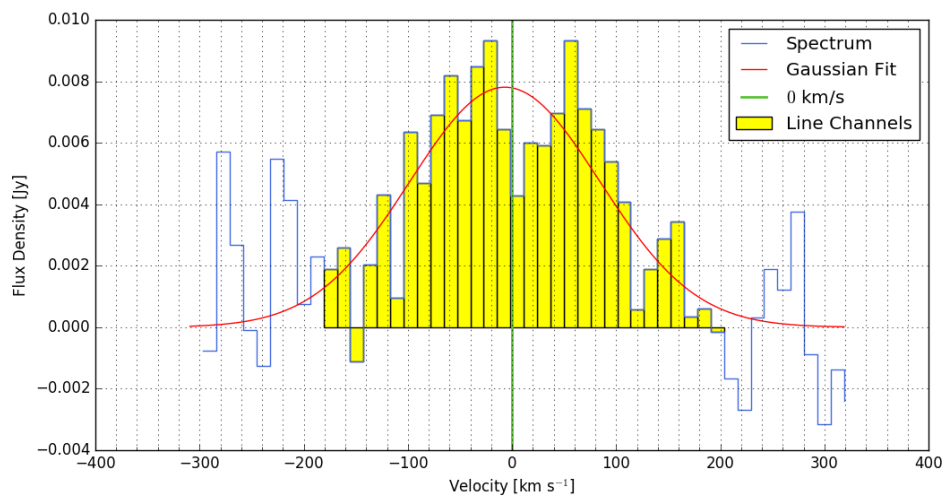


FIGURE 3.16: A fit to the clean spectrum from B-array and C-array combined. The spectrum was taken from an aperture based on the moment-0 map.

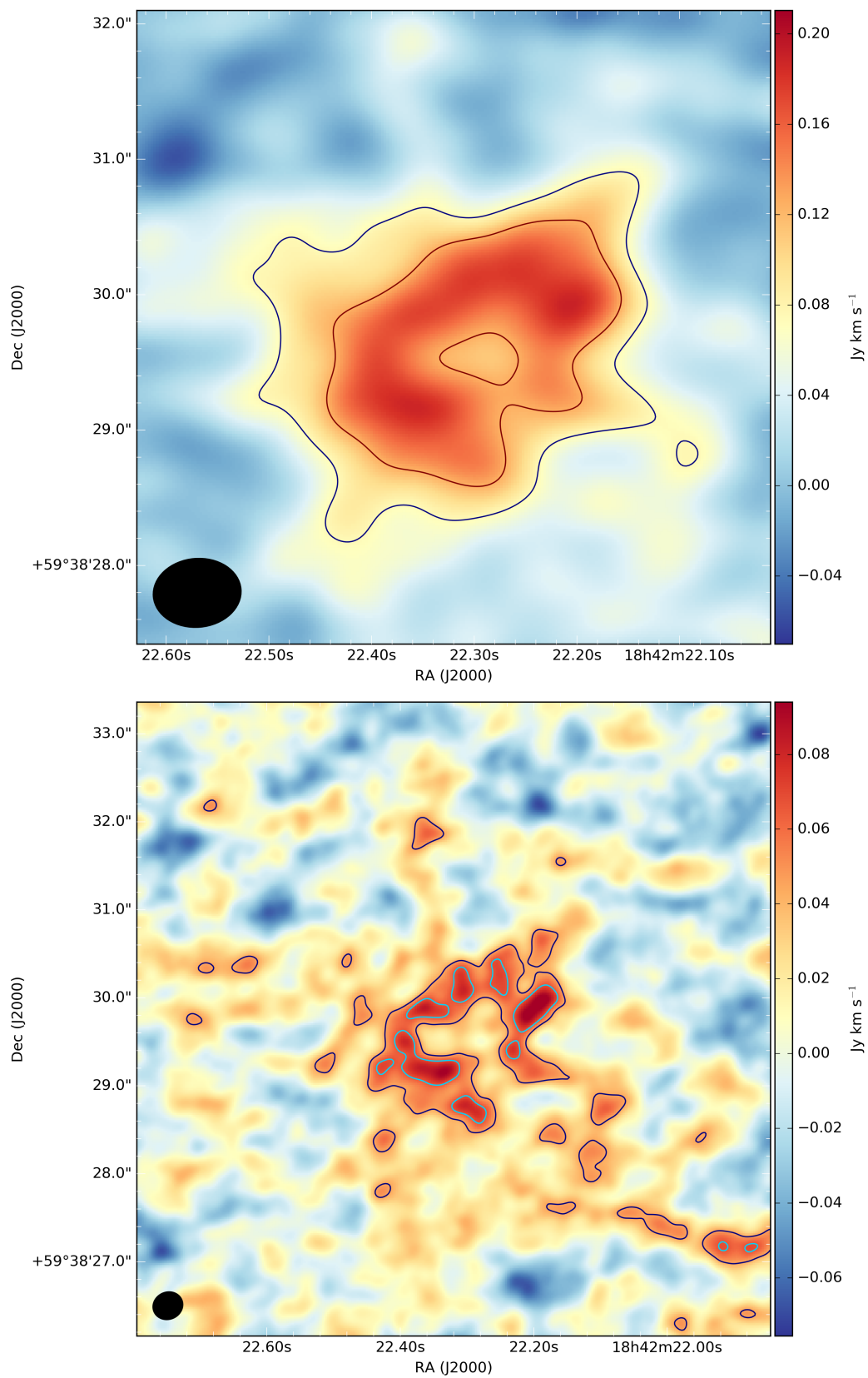


FIGURE 3.17: A velocity weighted intensity map obtained from the clean cube, combining B-array and C-array data with a $0.3''$ taper (*top*) and a $0.1''$ taper (*bottom*). Contours indicate the 3 and $5\sigma_{\text{RMS}}$ levels, where $\sigma_{\text{RMS}} = 0.025 \text{ Jy beam}^{-1} \text{ km s}^{-1}$ for the left image. For the right image the contours indicate 2 and $3\sigma_{\text{RMS}}$ levels with $\sigma_{\text{RMS}} = 22.2 \text{ mJy beam}^{-1} \text{ km s}^{-1}$.

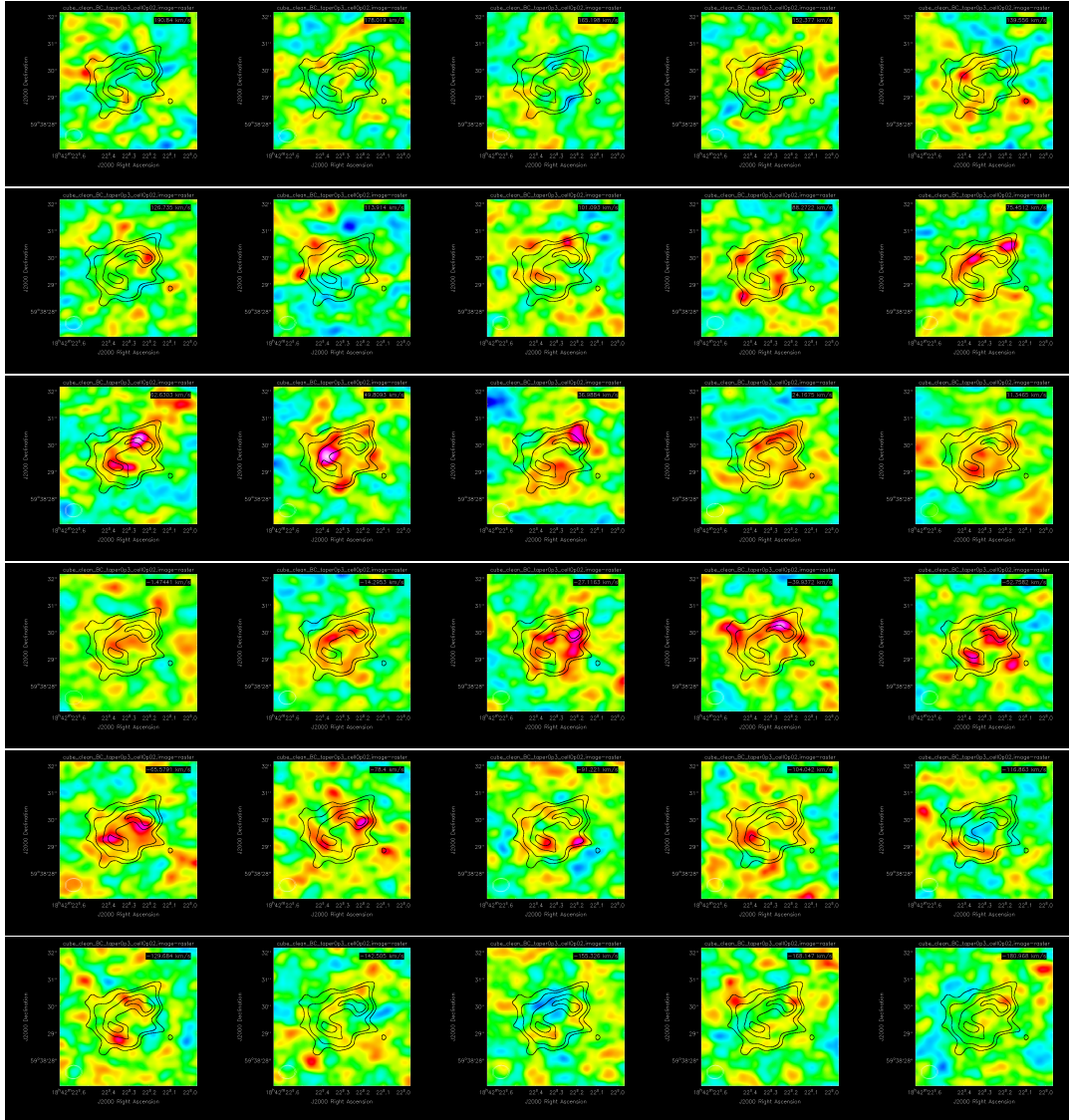


FIGURE 3.18: Channel maps for the CO(2-1) transition from combining the B-array and C-array data. Each channel is 12.8 km s^{-1} wide starting at 190.84 km s^{-1} at the top left to -181.0 km s^{-1} at the bottom right. Overlaid are the 3, 4, 6 and $7\sigma_{\text{RMS}}$ contours of the moment-0 map.

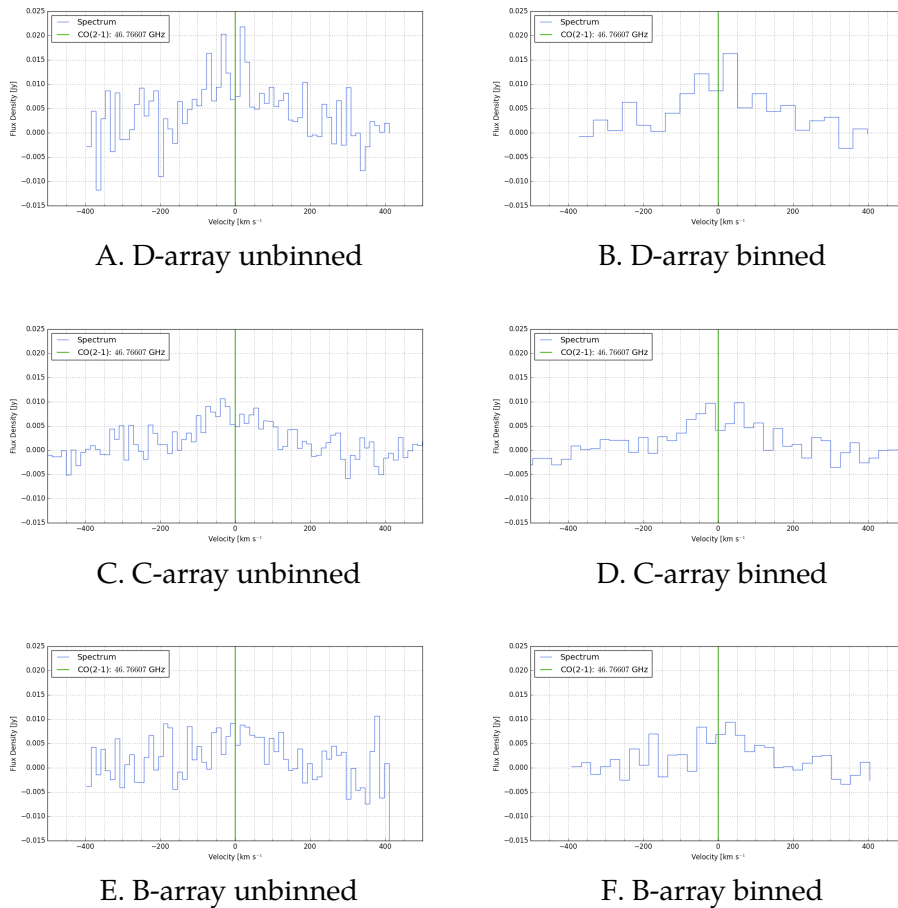


FIGURE 3.19: Spectra of the CO(2-1) emission taken through apertures determined through the moment-0 maps. The green line indicates the rest frequency of the transition at $z = 3.9296$ which is $\nu = 46.76607\text{GHz}$. In the *left* column unbinned spectra are shown ($\Delta v_{\text{chan}} = 12.82 \text{ km s}^{-1}$) and in the *right* column the spectrum is binned by two channels ($\Delta v_{\text{chan}} = 25.64 \text{ km s}^{-1}$) to match the CO(1-0) observations in terms of velocity width per channel. The C-array data shows a possible double-horn profile which would indicate a disk structure of the gas.

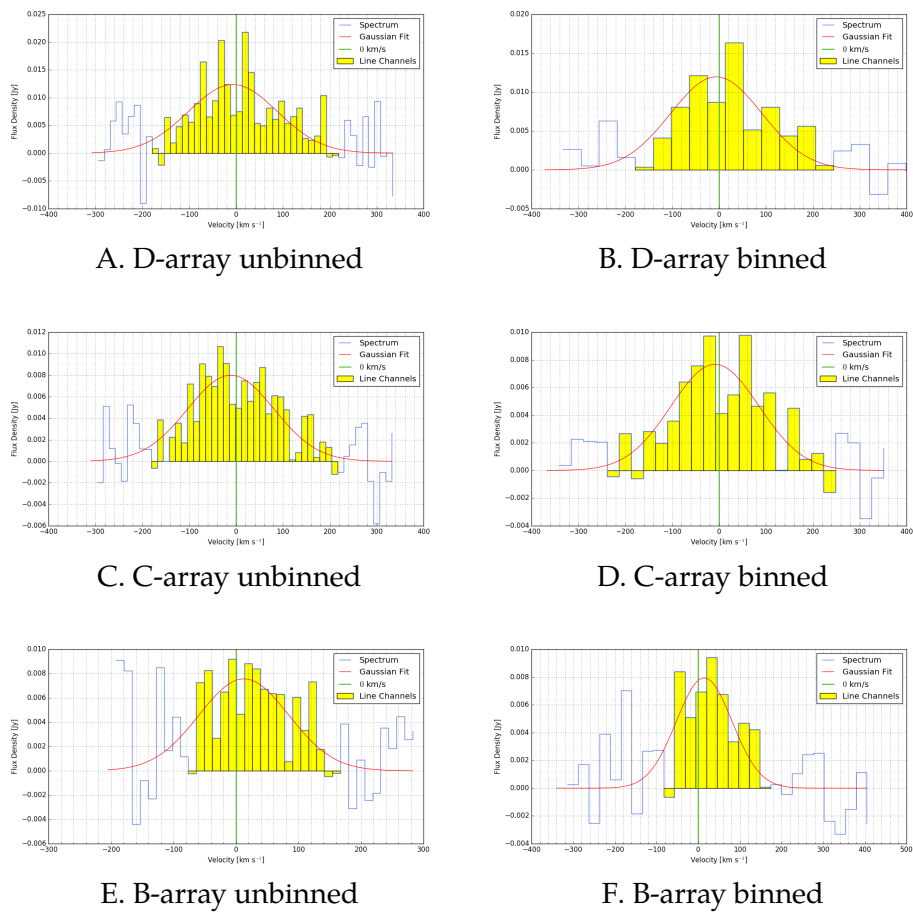
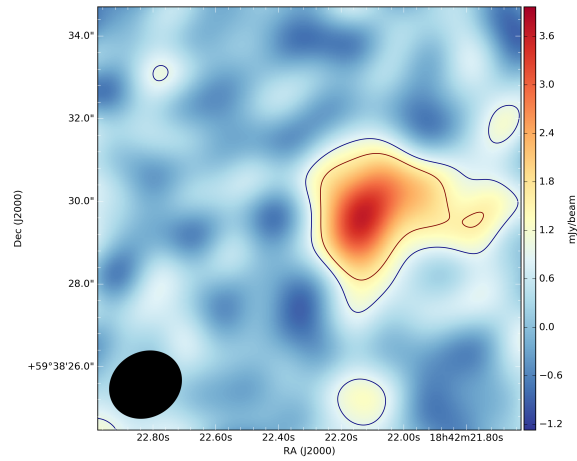
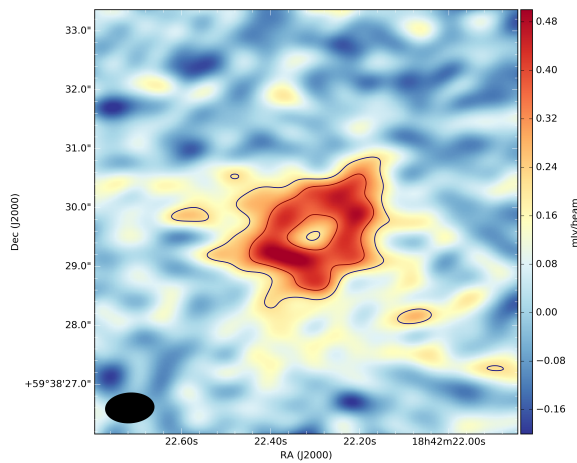


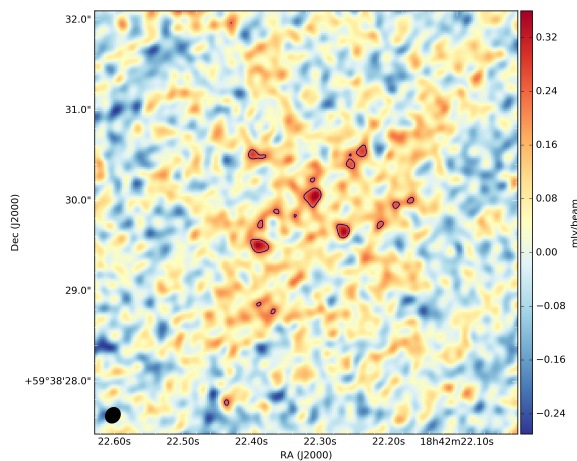
FIGURE 3.20: The CO(2-1) emission line as detected in the B, C and D configurations of the VLA. The *green* line indicates the transition's rest frequency $\nu = 46.76607$ GHz. Channels with *yellow* shading indicate channels considered to have line emission. Finally the *red* line is the Gaussian fit to the data.



A. D-array



B. C-array



C. B-array

FIGURE 3.21: Clean MFS maps obtained from the D (*top*), C (*middle*) and B (*bottom*) array observations of the CO(2-1) emission obtained by cleaning an MFS map of the line channels. In the B-array the source is mostly resolved out. The C-array shows an Einstein ring in CO emission. In case of the D-array there is an additional offset mostly to the right with respect to the radio position determined by [McKean et al. 2011](#) possibly due to pointing errors as all the other emission lines up. The map uncertainties are $\sigma_{\text{RMS}} = 0.32 \text{ mJy beam}^{-1}$, $70.1 \mu\text{Jy beam}^{-1}$ and $76.0 \mu\text{Jy beam}^{-1}$ respectively. The contours indicate 3 and $5\sigma_{\text{RMS}}$ levels. The colorbar is in mJy km s^{-1} .

3.4 250, 350 and 500 μm Sub-mm Emission and SED Fitting

Figure 2.33 shows the maps obtained from the Herschel data. Doing photometry yields the flux densities listed in Tab. 3.7.

Wavelength [μm]	Flux Density [mJy]
250	$105.1 \pm 6.4(2.65)$
350	$166.5 \pm 6.9(2.90)$
500	$176.2 \pm 7.6(3.39)$

TABLE 3.7: Herschel 250, 350 and 500 μm flux densities measured by the timeline fitter in HIPE. Reported are the full uncertainties of both fit and confusion noise. Uncertainties in parentheses indicate the statistical uncertainty.

3.4.1 SED Fitting

Figure 3.23 shows the most complete SED of MM18423 at the moment including existing measurements and measurements presented in this work. With the added Herschel measurements we can constrain the peak of the heated dust emission. Constraining this peak is most important as this is essential to determining the dust temperature responsible. Note that in [Lestrade et al. 2010](#) the 3 mm measurement has asymmetric error bars measuring $2_{-1.5}^{+2.0}$ mJy. For the fitting process we reduce this to a single errorbar as $\frac{\sigma_+ + \sigma_-}{2}$ giving $\sigma_{3\text{mm}} = 1.75$ mJy. When plotting we adopt the proper error bars.

To fit the SED a two component model was adopted consisting of a modified black body for the dust emission plus a power law component for the synchrotron emission. These profiles are given in Eqn. 3.10 and Eqn 3.11

$$S_\nu^{\text{MBB}} \propto \frac{\nu^{3+\beta}}{\exp\left(\frac{h\nu}{kT_d}\right) - 1} \quad (3.10)$$

$$S_\nu^{\text{PL}} \propto \nu^\alpha \quad (3.11)$$

where ν is the frequency, h is Planck's constant, k is Boltzmann's constant, β is the dust emissivity, T_d is the dust temperature and α is the power law index. For fitting these equations were rewritten as

$$S_\nu^{\text{MBB}}(\nu, T_d, \beta, B) = B \times T_d^3 \frac{x^{3+\beta}}{\exp(x) - 1} \quad (3.12)$$

with

$$x \equiv \frac{h\nu}{kT_d}$$

and

$$S_\nu^{\text{PL}}(\nu, \alpha, A) = A \times \left(\frac{\nu}{1 \text{ GHz}}\right)^\alpha \quad (3.13)$$

Please note that the x notation is only introduced to have the function return values of manageable magnitude. As x incorporates T_d (one of the free parameters)

we can not actually fit as function of x . Therefore the modified black body spectrum is still fitted *as function of frequency*. The modified black body and power law were fitted separately. To find the parameters for the modified black body part of the spectrum we used the `emcee` Python module to do an MCMC fit to the data. The power law part of the spectrum was fit with a least squares method using `scipy.optimize.curvefit`.

Using Bayesian statistics we explore the parameter space trying to find a combination of parameters that maximizes the probability of a certain model given the data, which is proportional to a likelihood times a prior. This is called *Bayes' theorem*:

$$p(\text{model}|\text{data}) = \frac{p(\text{data}|\text{model}) \times p(\text{model})}{p(\text{data})} \quad (3.14)$$

where $p(\text{data}|\text{model})$ is called the *likelihood* L , $p(\text{model})$ the *prior* and $p(\text{data})$ the evidence. In this case we work with the log-likelihood which is simply the natural logarithm of the likelihood: $\mathcal{L} = \ln L$. Starting from a normal Gaussian likelihood

$$L = \prod_n \frac{1}{\sqrt{2\pi\sigma^2}} e^{-\frac{(y_n - y_{\text{model}})^2}{\sigma^2}} \quad (3.15)$$

we can write

$$L = \prod_n \exp\left(-\frac{(y_n - y_{\text{model}})^2}{\sigma^2} - \frac{1}{2} \ln 2\pi\sigma^2\right) \quad (3.16)$$

A product of exponentials can be written as the exponential of a sum, so we get

$$L = \exp\left(\sum_n -\frac{(y_n - y_{\text{model}})^2}{\sigma^2} - \frac{1}{2} \ln 2\pi\sigma^2\right) \quad (3.17)$$

which after taking the natural logarithm gives us our log-likelihood:

$$\mathcal{L} = -\frac{1}{2} \sum_n \left(\frac{(y_n - y_{\text{model}})^2}{\sigma^2} + \ln 2\pi\sigma^2 \right) \quad (3.18)$$

The prior contains information about how much we believe in a certain model. In this prior we put constraints on the values of the parameter. These constraints were set as uniform priors within a certain region as shown in Eqn. 3.19.

$$\ln[p_{\text{MBB}}(\text{data}|T_d, \beta, B)] = \begin{cases} 0.0, & 0 < T_d < 100 \text{ K and } 0.5 < \beta < 2.5 \\ -\infty, & \text{otherwise} \end{cases} \quad (3.19)$$

For determining initial conditions we first minimized the negative log-likelihood using `scipy.optimize.minimize`. From this starting positions for each walker were then chosen randomly in a tiny Gaussian sphere around these values. With this an MCMC was started using 48 walkers and 10000 iterations. Uncertainties were then determined using the 16th, 50th and 84th percentiles of the samples. We summarize our results obtained from this procedure in Tab. 3.8. Figure 3.22 shows the covariance maps for all parameters in the fit. In Fig. 3.23 both components are evaluated over a selected wavelength range with their optimal parameters and added together to produce a global SED fit. Together with the fit random realizations are also drawn to give an indication of the uncertainty in the fit.

Parameter	Value
B	0.036 ± 0.004
$T_d/(1+z)$	$7.66^{+0.41}_{-0.38}$
β	1.68 ± 0.17
A	0.28 ± 0.07
α	-0.83 ± 0.34

TABLE 3.8: Parameter values as they are obtained from the MCMC chains and the least squares fit. For the parameters obtained using MCMC uncertainties were derived using the 16th, 50th and 84th percentiles.

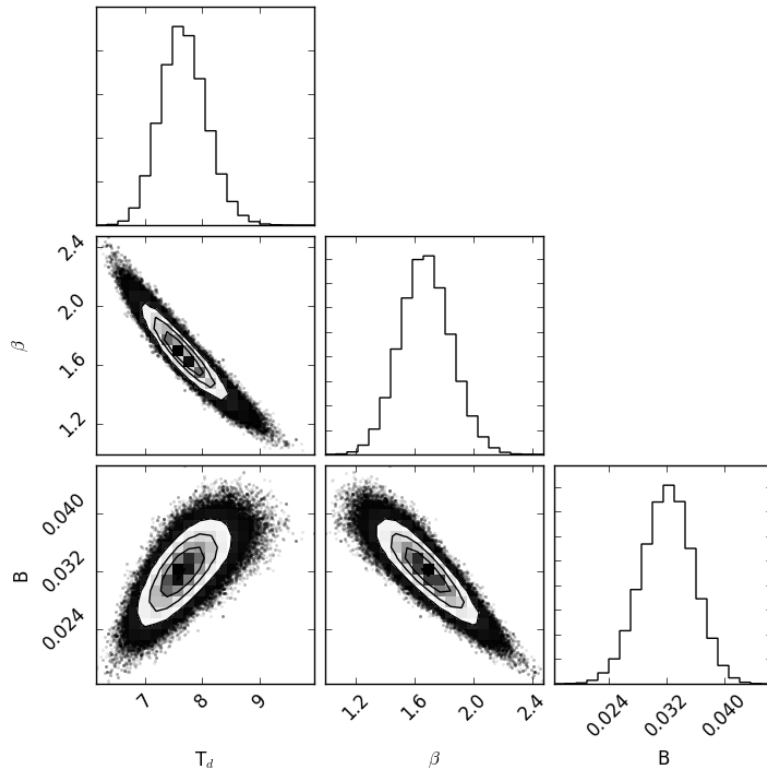


FIGURE 3.22: Corner plots produced with the Python corner module using data returned by emcee. The distributions and covariances between all parameters used to fit the modified black body component are shown. The contours indicate levels of sigma.

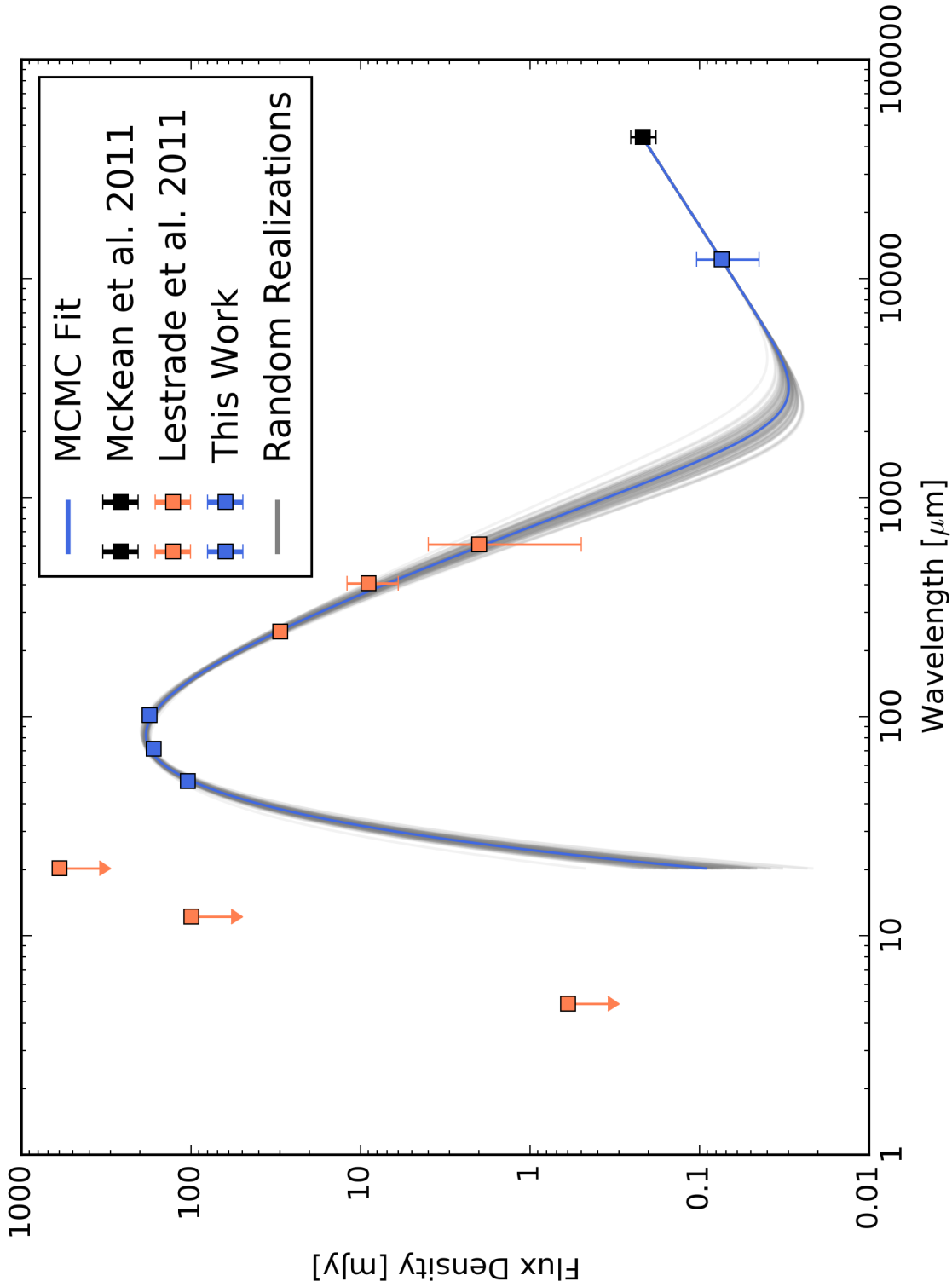


FIGURE 3.23: An MCMC fit to the SED of MM18423. The data points are the same as in Fig. ???. The *blue line* is the fit obtained by evaluating both components over a selected frequency range with the fitted parameters. Finally the *grey lines* are 100 random samples from each component added together to give an idea of the uncertainty in the fit. A peak wavelength of 82 μm is found.

Chapter 4

Interpretation

INTERPRETING the results will give insight in how MM18423 itself is structured and how it compares to other DSFGs. We compare the various maps to see if there are any correlations and we compare measurements to other DSFGs. Such a comparison has to be done with care though. One has to keep in mind that we are looking at a strongly lensed, $z \cong 4$ galaxy. The unlensed DSFGs that are selected are naturally biased towards the brighter end of this population. This is one pitfall comparing high and low(er) redshift DSFGs. There is also the fact that the star formation rate density evolves significantly from redshift 4 to 2 (see Fig. 1.2). As we go down from 4 to 2, the star formation rate density increases and hence the molecular gas reservoirs will deplete faster. Consequently, finding an unlensed DSFG with the same gas mass as a lensed DSFG, for example, does not necessarily imply they belong to the same population, given the vastly different epochs they spend their time in.

4.1 Continuum

In Fig. 4.1 and Fig. 4.2 the 5 GHz emission is overlaid on the HST observation. Only contours from the untapered data and the $0.5''$ tapered data are shown, as tapering to $1''$ loses just about all spatial information. No astrometric calibration has been applied, so we have to be somewhat careful with the interpretation. Looking at the contours of the continuum emission it is possible to line up the peaks in the radio with the east and north-west images in the NIR, with a translation and rotation. Based on this we believe the west and north-east blobs seen in the HST image to be true lensed images. Seeing both the NIR images and the radio images having a separation of $\sim 1.4''$, further leads us to believe they are indeed associated with each other. If we assume the NIR and radio emission to be co-spatial, the peaks in the images could be used to derive an astrometric calibration. This is highly uncertain however, as DSFGs are typically extremely dusty galaxies, strongly attenuating emission at short wavelengths.

At $z = 3.9296$ we are probing physical scales the size of $7.2 \text{ kpc}/''$. With a beam of $0.60'' \times 0.41''$ for robust=1 weighting, we can resolve structures down to 2.9 kpc . Apart from resolving out a significant amount of diffuse emission, there is no structure to be seen in the images; they remain point sources. Tapering the data and using natural weighting resulted in a beam of $0.87'' \times 0.70''$, resolving up to 5 kpc structures. The flux density roughly doubles doing this. A significant amount of emission is therefore emitted both from a compact region and a somewhat more extended component, with most of the emission coming from the more extended component. We can thus estimate that the continuum emitting region of the source

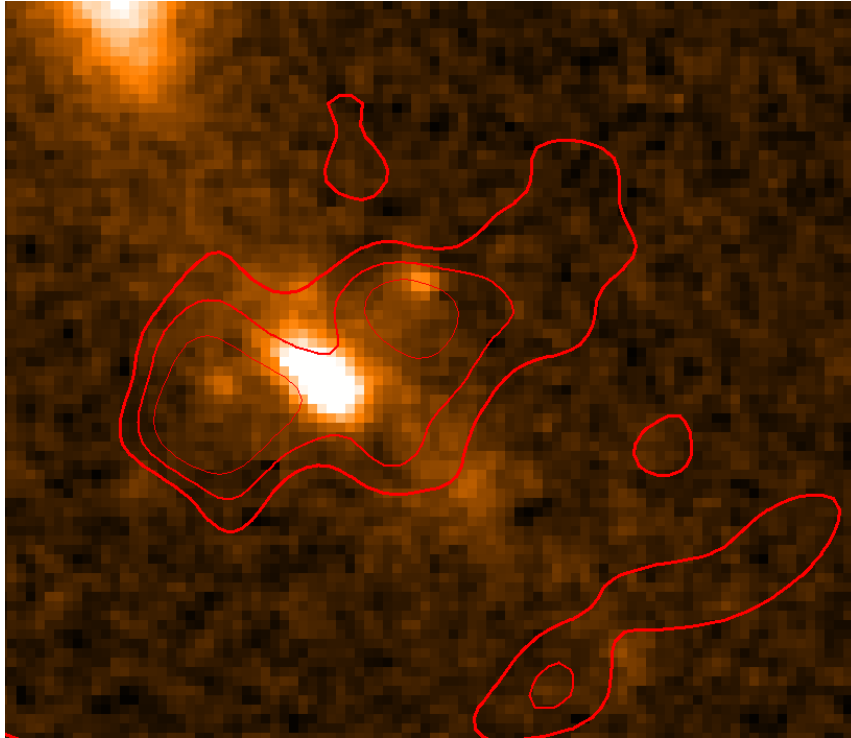


FIGURE 4.1: Continuum emission contours of the untapered data overlaid on HST 1.1 μm imaging. The contours are drawn at the 2, 3 and $4\sigma_{\text{RMS}}$ levels with decreasing line thickness.

is possibly within a < 5 kpc region. Higher resolution observations at 1.4 GHz, where the source is brighter, will help confirming this.

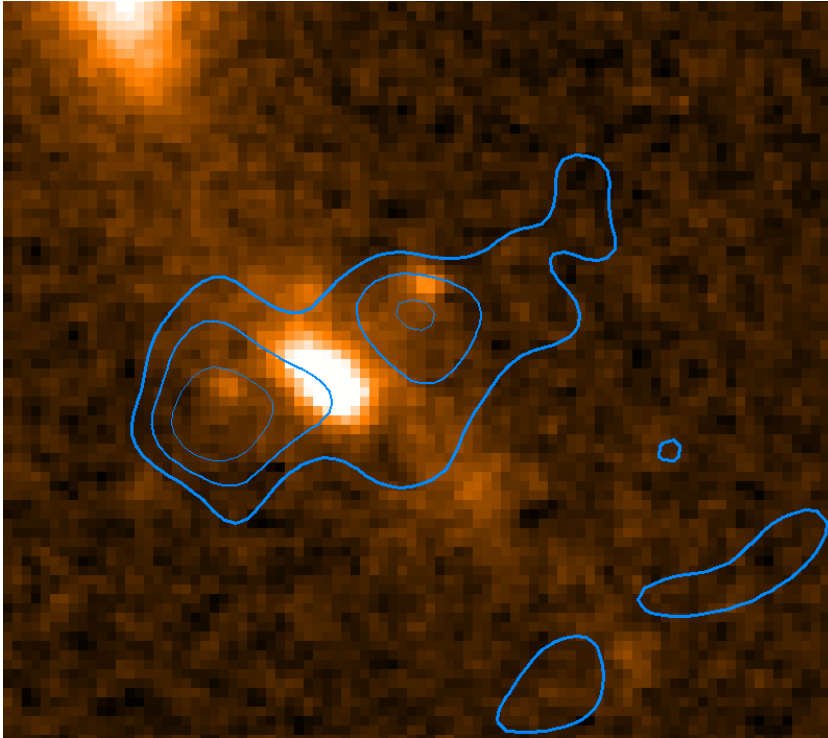


FIGURE 4.2: Continuum emission contours of the $0.5''$ tapered data overlaid on HST $1.1 \mu\text{m}$ imaging. The contours are drawn at the 2, 3 and $4\sigma_{\text{RMS}}$ levels with decreasing line thickness.

4.2 The Molecular Gas

While comparing the VLA data with the HST data is speculative, the various observations of radio continuum and CO can be compared directly, as both are phase referenced. The VLA Calibrator List contains positional accuracies for the phase reference source. This means they have a positional accuracy of $0.002'' - 0.01''$. This makes for a reliable comparison of spatial distribution.

Morphology

In Fig. 4.3 we compare the observed CO emission to the rest-frame UV and radio continuum emission. Clearly the CO is extended, forming two arcs in low excited gas and one larger arc in the higher excitation mode. The CO(1-0) looks to be doubly imaged, with three peaks, two of which seem coincident with the east and north-west images seen on the HST exposure. The eastern image appears to be a merging of the two compact images. Interestingly we see no evidence for the CO to be associated with the northern blob in the rest-frame UV. To the south-west however the CO seems to be possibly associated with the diffuse emission, which would indicate that it is in the source plane rather than in the lens plane. Speculatively, we could be looking at either infalling gas, or material from a merger event. It is impossible to tell at this moment however. Peaks of CO(2-1) shows possible correspondence between the east and north-western images, as well. There is no clear evidence for more images to the north and south-west or any association between the gas traced by this transition and the diffuse emission seen on the HST exposure. In fact, shifting the CO upwards and to the right (we are being hypothetical here with respect to the astrometry), there seems to be no association at all between the CO(2-1) and the diffuse emission seen in

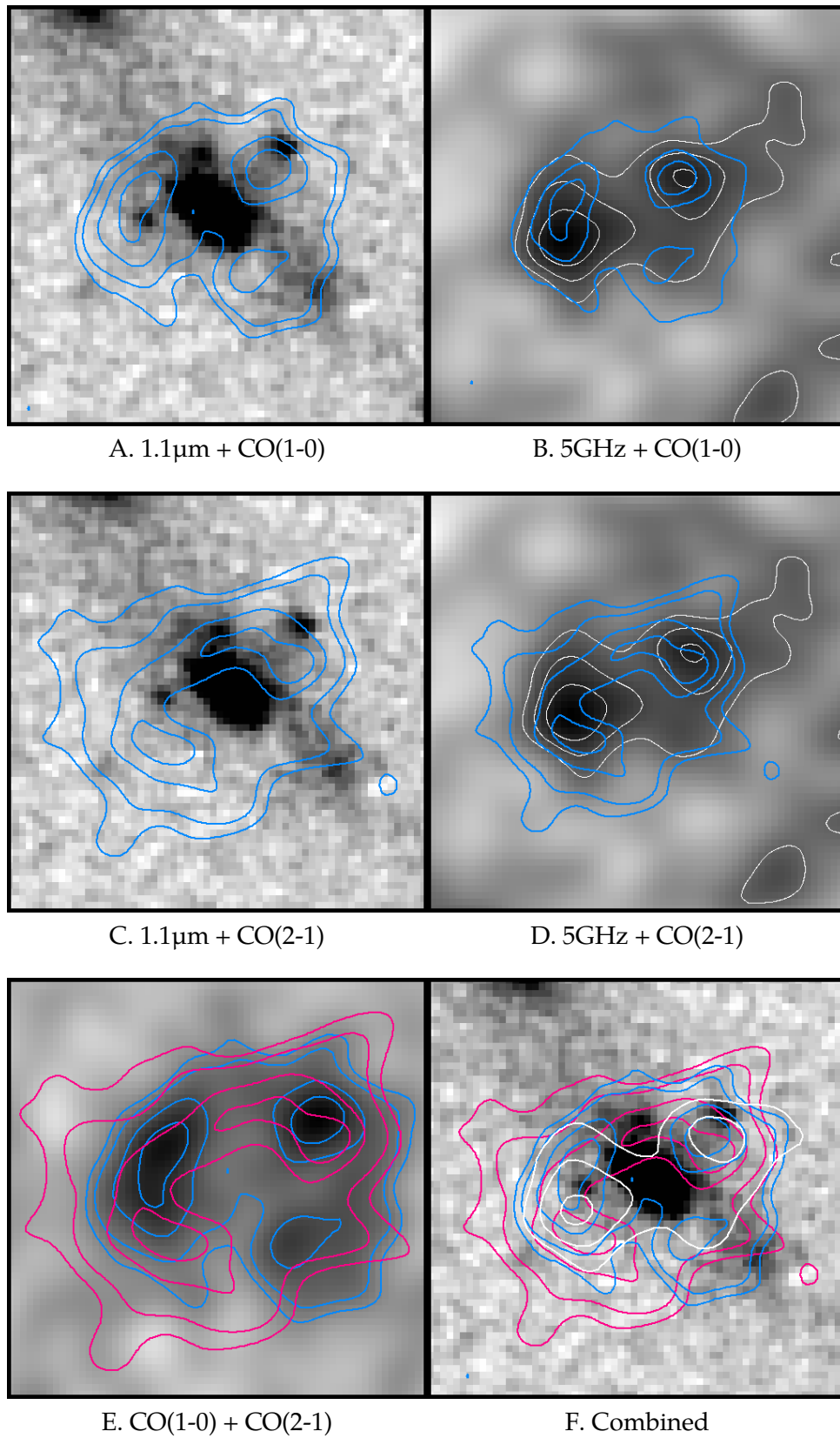


FIGURE 4.3: A summary plot comparing all emissions with each other. The contours are made using the moment-0 maps. *Top*: $\text{CO}(1-0)$ emission compared to $1.1\mu\text{m}$ and 5GHz emission. 5GHz contours are shown at $2, 3$ and 4σ levels. Contours indicate $2, 4, 6$ and 8σ levels. *Middle*: $\text{CO}(2-1)$ emission compared to $1.1\mu\text{m}$ and 5GHz emission. Contours indicate $3, 4, 6$ and 7σ levels. *Bottom*: $\text{CO}(2-1)$ emission compared to $\text{CO}(1-0)$ emission. Contours are the same as for the middle plots.

the rest-frame UV. This is further exemplified when comparing the CO(1-0) with the CO(2-1) emission. They broadly agree with each other, being mostly co-spatial, but peak at slightly different locations. More importantly, there is little to no association between the south-west emission seen in the CO(1-0) with the CO(2-1).

Comparing the molecular emission to the radio continuum emission we find their peaks coincide in the north-western image, but are offset in the eastern image. Interestingly, no continuum emission is significantly detected in the extended south-west tail. The apparent lack of both continuum and higher-order CO emission of this region is thought-provoking as in whether this emission is coming from a star forming region, the galaxy's outskirts or is associated with the galaxy in some other way.

Spectral Structure

Looking at the spectra, the CO emission appears to be doubly peaked. While not so clear in the CO(1-0) spectrum, the CO(2-1) spectrum clearly shows two components. Seeing a doubly peaked profile is a hint of velocity structure in the source, possibly a rotating disk, which has been seen before in DSFGs. See for example [Hodge et al. 2012](#) for GN20, a DSFG with an extended 14 kpc disk with ordered rotation, or [Engel et al. 2010](#), who find double peaked profiles as well. It is difficult to say however, because detailed dynamical modeling to the lensing corrected data needs to be done to see if the spectrum is consistent with a disk.

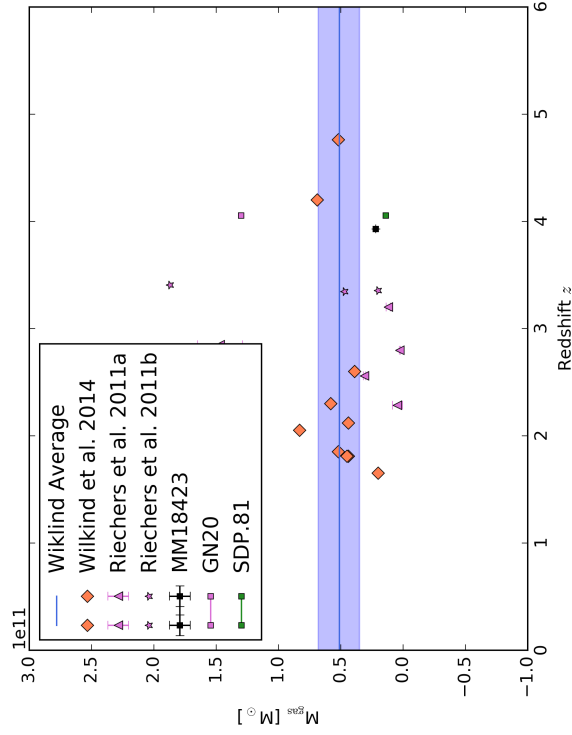
The individual channel maps of the gas do not show evidence for ordered rotation being present. Structure does not appear and disappear gradually over the arc or images, but are in arbitrary positions instead. This could be due to MM18423+5938 being disturbed from a merger event, but without proper velocity maps it is difficult to say. The south-west tail of CO(1-0) emission only shows up significantly at -50 km s^{-1} and -75 km s^{-1} . As this region appears to be lacking in either CO(2-1) or radio continuum emission, this might be outflowing gas.

Molecular Gas Mass

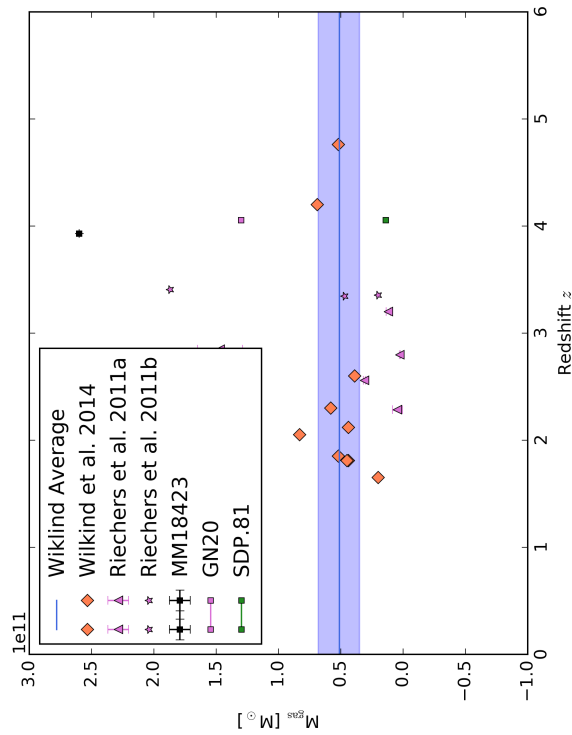
We estimate an H₂ gas mass of

$$2.6 \pm 0.5 \times 10^{11} \times \frac{\alpha_{\text{CO}}}{0.8} M_{\odot} \mu^{-1} \quad (4.1)$$

or $2.2 \pm 0.4 \times 10^{10} M_{\odot} \frac{12}{\mu}$ assuming the magnification by [Lestrade et al. 2011](#). In [Fig. 4.4A](#) and [4.4B](#) we have plotted this measurement both uncorrected and corrected with this magnification factor. Also plotted are measurements from ten DSFGs in the GOODS-S field, as presented in [Wiklind et al. 2014](#). After correcting for the lensing magnification factor, MM18423+5938 agrees with the other measurements, being relatively light in terms of molecular gas content compared to the GOODS-S sample. We have to keep in mind however that the DSFGs in that sample are not lensed, and hence is biased towards the brighter, more extreme end of the population, whereas MM18423+5938 is a more typical DSFG that would not be observable without the aid of lensing. Plotted as well, are a sample of lensed quasars and a sample of lensed DSFGs presented by [Riechers 2011](#) and [Riechers et al. 2011a](#).



A. The gas mass for MM18423 as measured from the CO(1-0) data compared to a GOODS-S sample of DSFGs presented in Wiklind et al. 2014. Also plotted are the gas masses measured for GN20 (*pink square*; Carilli et al. 2011) and SDP.81 (*green*; Frayer et al. 2011). Also plotted are the masses from a sample of lensed quasar host galaxies from Riechers 2011 (*pink triangles*) and three lensed DSFGs from (*pink stars*).

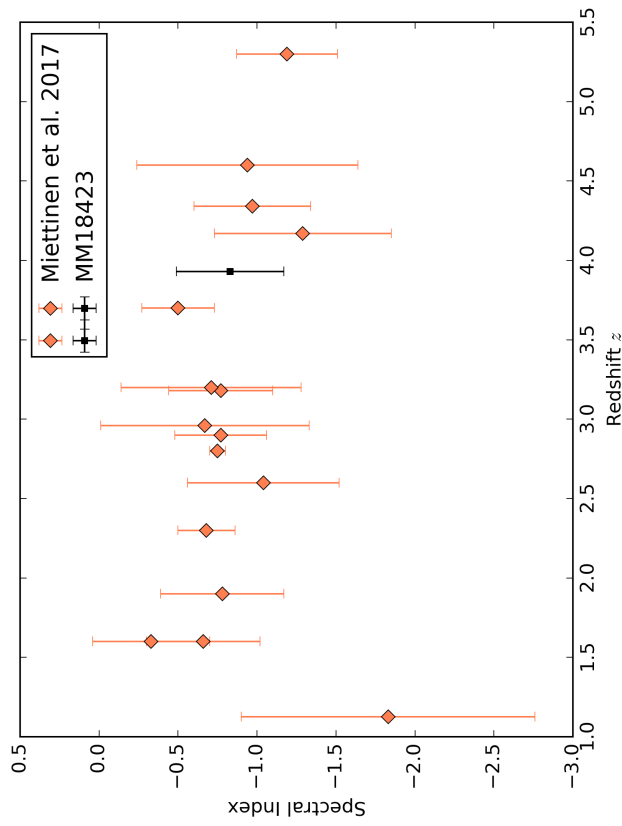


B. The gas mass for MM18423 corrected for lensing, with $\mu = 12$, compared to a GOODS-S sample of DSFGs presented in Wiklind et al. 2014. Also plotted are the gas masses measured for GN20 (*pink*; Carilli et al. 2011) and SDP.81 (*green*; Frayer et al. 2011). Also plotted are the masses from a sample of lensed quasar host galaxies from Riechers 2011 (*pink triangles*) and three lensed DSFGs from (*pink stars*).

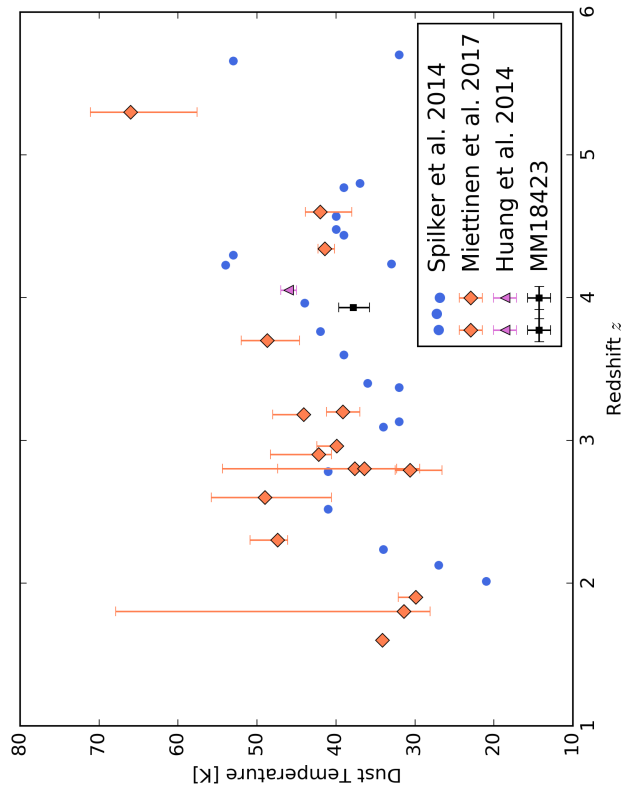
4.3 Heated Dust Emission

Dust Temperature and Spectral Index

For MM18423 we derive a dust temperature of $T_d = 37.8^{+2.0}_{-1.9}$ K (after converting back to the rest frame), with a peak rest-frame wavelength of 82 μm and a dust emissivity of $\beta = 1.7 \pm 0.2$. For the power law we find a spectral index of $\alpha = -0.83 \pm 0.34$. These values are consistent with what has been found previously for DSFGs. For example [Miettinen et al. 2017](#) report on a sample of AzTEC DSFGs with redshifts between roughly 1 and 5 for which they find a median dust temperature of $T_d = 40.6^{+7.5}_{-8.1}$ K and a median spectral index of $\alpha = -0.77^{+0.28}_{-0.42}$. [Spilker et al. 2014](#) find $T_d = 44$ K for SPT 0125-50, an DSFG with $z = 3.9592$ nearly identical to MM18423. We have plotted the SPT and AzTEC samples in Fig. 4.4A along with MM18423, clearly showing that MM18423 has a dust temperature consistent with other DSFGs. This dust temperature is almost a factor 2 larger than what is reported by [McKean et al. 2011](#). We attribute this to the lack of photometric data available at the time, leaving the peak of the spectrum unconstrained. The emissivity β is somewhat higher, but not significantly different from the literature, where often a value of $\beta \sim 1.5$ is assumed. Finally we find a spectral index that is consistent with other DSFGs. As an example findings for α (measured over the range of 325 MHz to 3 GHz) from [Miettinen et al. 2017](#) are plotted in Fig. 4.4B together with MM18423+5938 which show that this object is consistent with other DSFGs found over a wide range of redshifts.



A. A comparison between our measured dust temperatures for MM18423 and the dust temperatures determined from AzTEC (*red*) and SPT (*blue*) samples reported in Miettinen et al. 2017 and Spilker et al. 2014 respectively along with a measurement of GN20 by Huang et al. 2014. Uncertainties of the literature sources are omitted for the sake of clarity, but are of the order of a few K. MM18423's dust temperature is consistent with these measurements.



B. A comparison between our measured spectral index for MM18423 and spectral indices determined from AzTEC (*red*) sources reported in Miettinen et al. 2017. Uncertainties of the literature sources are omitted for the sake of clarity, but are of the order of 0.5. Given our uncertainty MM18423's spectral index is consistent with these measurements.

4.3.1 Radio-FIR Correlation and SFR

Having an expression for the SED we can check if MM18423 is on the radio-FIR correlation which will tell us if the emission is due to star formation or that there could be other processes at play. This correlation was introduced by [Helou et al. 1985](#) through a parameter q and is defined as

$$q = \log \frac{F_{\text{FIR}}}{3.75 \times 10^{12} \text{ Hz}} - \log S_{1.4\text{GHz}} \quad (4.2)$$

where F_{FIR} is the FIR flux obtained by integrating the SED as

$$F_{\text{FIR}} = \int_{8\mu\text{m}}^{1000\mu\text{m}} S_{\lambda} d\lambda \approx \int_{300\text{GHz}}^{37\text{THz}} S_{\nu} d\nu \quad (4.3)$$

and $S_{1.4\text{GHz}}$ is the 1.4 GHz flux density. As we cannot properly integrate our simple SED over this range we use Equations 1.6 and 1.7 to estimate this flux. The full expression for the FIR luminosity then becomes

$$L_{\text{FIR}} = 1.91 \times 4\pi D^2 \times \int_{42.5\mu\text{m}}^{122.5\mu\text{m}} S_{\lambda} d\lambda. \quad (4.4)$$

Using the definition of luminosity, i.e. $L = 4\pi D^2 \times F$ we can rewrite Eqn. 4.2.

$$\begin{aligned} q &= \log \frac{F_{\text{FIR}} \text{ W m}^{-2}}{3.75 \times 10^{12} \text{ Hz} \times S_{1.4\text{GHz}}} \\ &= \log \frac{4\pi D^2 \times F_{\text{FIR}}}{3.75 \times 10^{12} \times 4\pi D^2 \times F_{1.4\text{GHz}}} \end{aligned}$$

where we used the unit Hz converts the flux density S into a flux F , leaving us with

$$q = \log \frac{L_{\text{FIR}}}{3.75 \times 10^{12} \times L_{1.4\text{GHz}}}.$$

The 1.4 GHz luminosity is calculated as

$$L_{1.4\text{GHz}} = 4\pi D_L^2 S_{1.4\text{GHz}} (1+z)^{-(1+\alpha)} \quad (4.5)$$

according to [Lestrade et al. 2011](#) where D_L is the luminosity distance. Its uncertainty is calculated using error propagation as

$$\begin{aligned} \sigma_L^2 &= \left(\frac{\partial L}{\partial S} \right)^2 \sigma_S^2 + \left(\frac{\partial L}{\partial \alpha} \right)^2 \sigma_{\alpha}^2 \\ &= \left[4\pi D_L^2 (1+z)^{-(1+\alpha)} \right]^2 \sigma_S^2 + \left[4\pi D_L^2 S_{1.4\text{GHz}} \cdot -(1+\alpha)(1+z)^{-(2+\alpha)} \right]^2 \sigma_{\alpha}^2 \\ &= \left[4\pi D_L^2 (1+z)^{-(1+\alpha)} \right]^2 \times \left[\sigma_S^2 + \frac{(1+\alpha)^2}{(1+z)^2} \sigma_{\alpha}^2 \right] \end{aligned}$$

giving us

$$\sigma_L = 4\pi D_L^2 (1+z)^{-(1+\alpha)} \times \sqrt{\sigma_S^2 + \frac{(1+\alpha)^2}{(1+z)^2} \sigma_{\alpha}^2} \quad (4.6)$$

Quantity		Value
L_{IR}	$10^{13} L_{\odot} \mu^{-1}$	5.11 ± 0.015
L_{FIR}	$10^{13} L_{\odot} \mu^{-1}$	9.76 ± 0.30
$L_{1.4\text{GHz}}$	$10^{25} \text{ W Hz}^{-1} \mu^{-1}$	$2.57 \pm 0.46^{\text{a}}$
$\log L_{\text{IR}}/L_{\odot}$		13.71 ± 0.01
$\log L_{\text{FIR}}/L_{\odot}$		13.99 ± 0.01
q		2.59 ± 0.47
SFR	$M_{\odot} \text{ yr}^{-1} \mu^{-1}$	1.69×10^4

TABLE 4.1: Luminosities and the q value derived from fitting the SED. The uncertainties were obtained by evaluating the quantities for each realization of the MCMC chain and subsequently using the 16th, 50th and 84th percentiles unless otherwise noted. When there is only one error given the upper and lower uncertainties were indistinguishable at the given precision. Note that these luminosities are not yet corrected for lensing. (a) Derived using the optimal parameter value and its error.

Similarly the error in q can be determined by first letting

$$A \equiv \frac{L_{\text{FIR}}}{3.75 \times 10^{12} \times L_{1.4\text{GHz}}}$$

and

$$\sigma_A = A \sqrt{\left(\frac{\sigma_{\text{FIR}}}{L_{\text{FIR}}}\right)^2 + \left(\frac{\sigma_{1.4\text{GHz}}}{L_{1.4\text{GHz}}}\right)^2}$$

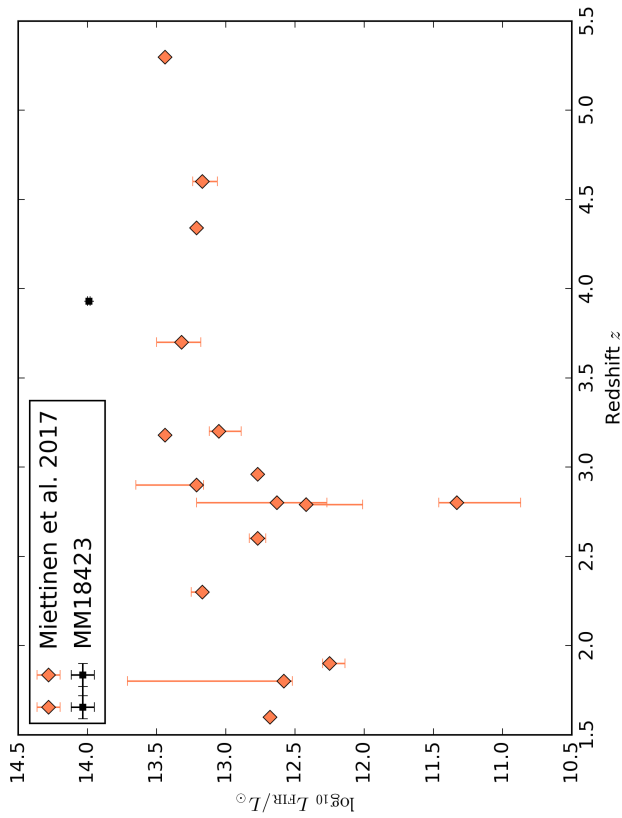
which using

$$\sigma_q = \left| \frac{\sigma_A}{A \ln 10} \right|$$

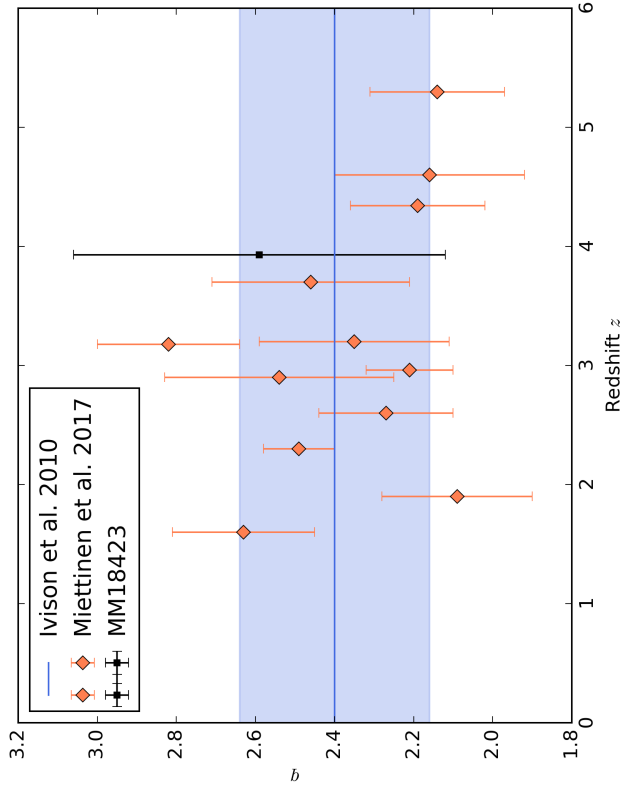
leads us to

$$\sigma_q = \frac{\sqrt{\left(\frac{\sigma_{\text{FIR}}}{L_{\text{FIR}}}\right)^2 + \left(\frac{\sigma_{1.4\text{GHz}}}{L_{1.4\text{GHz}}}\right)^2}}{\ln 10} \quad (4.7)$$

In Tab. 4.1 we summarize the various luminosities and the q parameter found from our SED model. The error on $L_{1.4\text{GHz}}$ comes directly from propagating the errors from the best fit for α and the $S_{1.4\text{GHz}}$ uncertainty, whereas the other quoted uncertainties are estimated by analyzing the scatter across all realizations in the MCMC chain. Note that $L_{1.4\text{GHz}}$, L_{IR} and L_{FIR} are all magnified due to lensing effects. The actual values can be an order of magnitude lower. The q parameter is not affected, because we take a ratio of two luminosities causing the magnification to divide out. This is under the assumption that the radio and FIR emission are co-spatial. In Figures 4.4A and 4.4B we compare our FIR luminosity and q parameter to those found by Miettinen et al. 2017 in a sample of AzTEC DSFGs. Taking into account the magnification (~ 12 by an early estimate of Lestrade et al. 2011) the FIR luminosity seems to be consistent with this sample. Our q parameter of $q = 2.59 \pm 0.47$ is in agreement with their findings as well. It also agrees with Ivison et al. 2010b who find a median value of $q = 2.40 \pm 0.24$.



A. Our FIR luminosity measurement for MM18423 plotted among measurements made from the AzTEC sample in Miettinen et al. 2017. MM18423 appears to lie above this sample by about one order of magnitude. This is most likely caused by the lensing magnification.



B. Our measurement of q for MM18423 plotted among measurements made from the AzTEC sample in Miettinen et al. 2017. MM18423 has a value for q that is perfectly consistent with those found in the AzTEC sample and is in agreement with other studies. The blue line indicates the value found by Ivison et al. 2010b and the shaded region their 1σ uncertainty region. The IR emission of MM18423 is predominantly due to intense star formation.

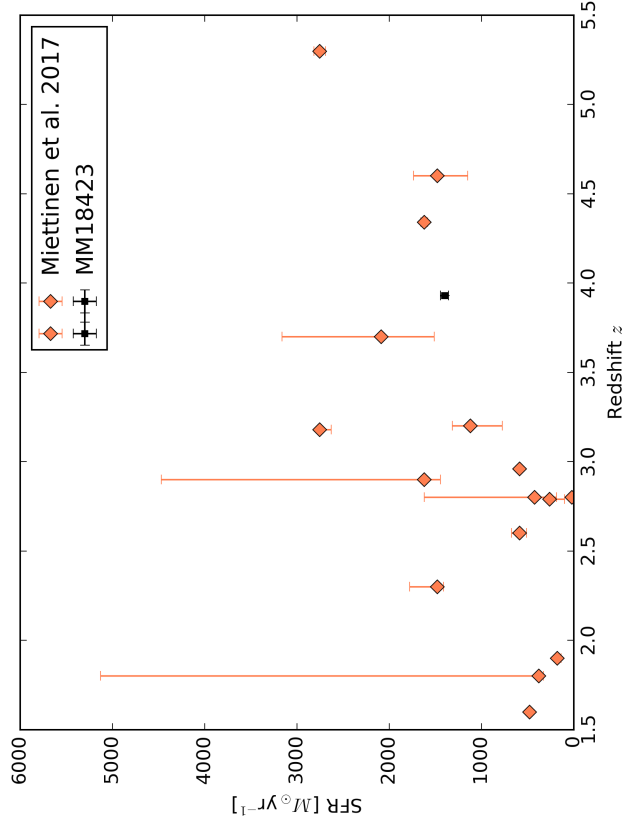
The FIR luminosity can be used to estimate the star formation rate in a galaxy following Eqn.1.4 published by [Kennicutt 1998a](#). Using this relation we find

$$\text{SFR} = 16827 \pm 517 \text{ M}_{\odot}\text{yr}^{-1}\mu^{-1} \quad (4.8)$$

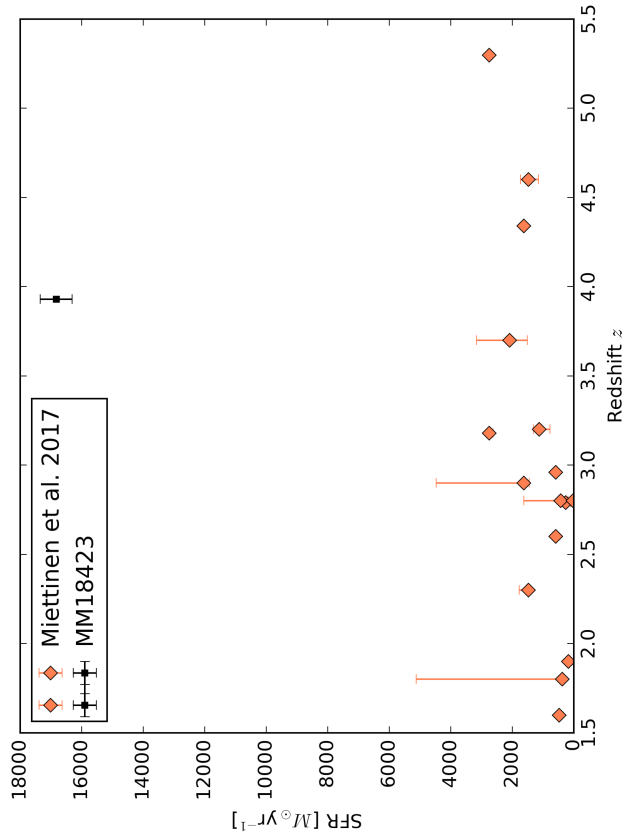
which is high; even for strong starbursting systems such as DSFGs. Assuming that this relation hold out to high redshift, this might be a hint on its own that gravitational lensing could be at play. In Fig. 4.4A we compare the SFR of MM18423 to other DSFGs in the AzTEC sample by [Miettinen et al. 2017](#). It is immediately obvious that our SFR does not fit the AzTEC sample. However if we take the $\mu \sim 12$ reported by [Lestrade et al. 2010](#) and correct for it MM18423's SFR of

$$\text{SFR} = 1402 \pm 43 \text{ M}_{\odot}\text{yr}^{-1} \frac{12}{\mu} \quad (4.9)$$

agrees well with the DSFGs in the sample.



B. A comparison between our SFR derived from L_{FIR} and the AzTEC sample from [Miettinen et al. 2017](#). Assuming a magnification of $\mu = 12$, MM18423+5938 agrees with the sample.



A. A comparison between our SFR derived from L_{FIR} and the AzTEC sample from [Miettinen et al. 2017](#).

Chapter 5

Conclusion

HAST but not least this section contains a summary of the results presented in this thesis together with concluding remarks about how MM18423 fits in with the rest of the population of dusty, starbursting galaxies at high redshift. First we looked at 1.1 μm HST observations which probe the rest-frame UV emission from the hot, young stars and show us the dust-unobscured region of the galaxy. Three lensed images can be identified after combining all the data. There is also a large edge-on disk galaxy nearby that, if close to the lens, can impact the lens modeling.

Next we analyzed 5 GHz observations made with the VLA in the A-array configuration. With this measurement a new datapoint could be added to the power-law part of the spectrum due to synchrotron emission. After stacking 10 datasets for almost 7 hours on source we identify two lensed images. From these images we measured a 5 GHz flux density of

$$S_{5\text{GHz}} = 74.2 \pm 29.6 \mu\text{Jy} \quad (5.1)$$

for MM18423+5938. To compare the spatial alignment of the radio emission with the rest-frame UV emission the 5 GHz data was overlaid on the HST imaging. No astrometric calibration was applied, so in all cases the pointing accuracy between HST and the VLA is not guaranteed so any conclusions from comparing the radio maps to the HST imaging should therefore be drawn cautiously. In any case the images seen in the radio map appear to line up (after some translation and rotation) with two of the three potential lensed images identified in the HST exposure.

Thirdly we analyzed the molecular gas in MM18423+5938 by looking at emission of the CO(1-0) and CO(2-1) rotational transitions. They trace the cold gas of a couple of Kelvin and slightly warmer gas of tens of Kelvin. The cold gas was observed in B and D array. In the D array the source is unresolved. This is ideal for measuring the flux density. A flux density of

$$S_{1-0} = 2.8 \pm 0.3 \text{ mJy} \quad (5.2)$$

was measured from the cleaned MFS map. This is somewhat in consistent with a previous measurement by [Lestrade et al. 2011](#) from C-array data, being . By fitting a Gaussian profile to the line we obtained an estimate of the line's velocity FWHM allowing us to calculate a line luminosity:

$$L'_{1-0} = 3.1 \pm 0.6 \times 10^{11} \mu^{-1} \text{K km s}^{-1} \text{pc}^2 \quad (5.3)$$

$$L_{1-0} = 1.5 \pm 0.3 \times 10^7 \mu^{-1} L_{\odot} \quad (5.4)$$

This line luminosity was converted to a molecular hydrogen gas mass using the CO-to-H₂ conversion factor for local ULIRGS $\alpha_{\text{CO}} = 0.8$. Assuming this factor also holds for DSFGs we obtain

$$M_{\text{gas}} = 2.6 \pm 0.5 \times 10^{11} \times \frac{\alpha_{\text{CO}}}{0.8} \mu^{-1} M_{\odot}. \quad (5.5)$$

With the high-resolution B-array data we gain more insight in the spatial distribution of the gas. Three peaks are identified at a $6\sigma_{\text{RMS}}$ level and two out of three at 8. There is also a hint of a diffuse Einstein ring connecting the images. Comparing it to the HST imaging and the 5 GHz map we find that the $8\sigma_{\text{RMS}}$ peaks are coincident with the west and north-east images in HST and line up with the two images identified in the 5 GHz map. The warmer gas traced by the CO(2-1) transition was studied using data taken in the B, C and D-array of the VLA. Unfortunately the B-array resolves out all but the brightest peaks of flux and the D-array could not be combined with the other data due to an additional offset from the phase center causing misalignment with the rest of the data. There was no time to investigate and correct this for this thesis. What we could have tried was to apply the flux calibration derived for the first dataset to the other two. This does assume however that this calibration is stable and applicable over the timespan of a month. How strongly this assumption holds depends on the weather condition among others. Fitting the clean spectrum of the CO(2-1) emission we find

$$S_{2-1} = 12.4 \pm 1.5 \text{ mJy}. \quad (5.6)$$

In both cases we find a slightly higher amplitude for the line, when compared to previous imaging by [Lestrade et al. 2011](#). In case of the CO(1-0) it is 32% higher. The data published in the paper, however, was reduced 6 years ago. Over this time calibration algorithms have likely improved. Our bandwidth is also significantly larger (2 GHz compared to 256 MHz; almost a factor of 10), which should improve the quality of the calibration due to broader frequency coverage for the calibrator sources. We therefore see no reason not to believe our result.

In the C-array data we can see a beautiful Einstein ring in the CO(2-1) emission. Comparing our C-array map to [Lestrade et al. 2011](#) (it is the same data) there are differences. We attribute these differences to multiple factors. First of all their map only shows emission averaged over the FWHM of the line, whereas our map shows the average of all channels with line emission. Secondly they used robust=1 weighting while we opted for natural weighting. The former leans slightly more towards resolution while the latter more towards lower noise. Lastly we used our own method to determine the weights for the visibilities to replace the standard weights given by CASA.

The spectrum of the CO(2-1) emission shows strong evidence for a double peak profile. This has been seen previously in DSFGs and provides evidence that MM18423+5938 has velocity structure, possibly a disk. Channel maps do not show signs of ordered rotation, with emission appearing in arbitrary positions between the channels. This could indicate a disturbed morphology due to a merger. Further investigation is necessary however to better explore the velocity structure of this object.

Finally we processed Herschel SPIRE observations of MM18423+5938 at 250, 350 and 500 μm . This emission traces the heated dust emission and allows us to study the dust-obscured star formation. With the addition of these three measurements the peak of MM18423+5938's SED can now be properly constrained allowing us to estimate a dust temperature and ultimately a star formation rate.

By fitting the modified blackbody part of the spectrum we estimate a dust temperature of $T_d = 37.8_{-1.9}^{+2.0}$ K emitting at a peak rest-frame wavelength of $82 \mu\text{m}$ and a dust emissivity $\beta = 1.68 \pm 0.17$. A power-law fit to the low frequency part of the spectrum finds a spectral index of $= -0.83 \pm 0.34$. Measuring the FIR luminosity $L_{8\mu\text{m}-1000\mu\text{m}}$ we find

$$L_{8\mu\text{m}-1000\mu\text{m}} = 9.76 \pm 0.30 \times 10^{13} \mu^{-1} L_{\odot} \quad (5.7)$$

which translates into a star formation rate of

$$\text{SFR} = 1.7 \times 10^4 \mu^{-1} M_{\odot} \text{ yr}^{-1} \quad (5.8)$$

Having both a radio and a FIR luminosity we checked whether MM18423 was on the Radio-FIR correlation. With a q-value of

$$q = 2.59 \pm 0.47 \quad (5.9)$$

this object is consistent with other DSFG samples at fits right on this correlation. This tells us the emission is predominantly coming from star formation and not an AGN for example.

5.1 Future Studies

To conclude this thesis I speculate on future work along with additional observations that could be useful to further explore this object. Starting off, the lensing galaxy is more complex than previously thought and would benefit greatly from more studies to classify its morphology. More studies of this target will also help determine whether there is additional structure in the lens or source plane.

For the SED, the data have constrained the possible range of parameters in a satisfactory way. Improvements that can be made are possibly additional photometric data points to constrain the turnover from a modified black body to a power law. This is not of major importance however. A better fit would be obtained if the spectrum was fit as a whole, i.e. simultaneously fitting the MBB and powerlaw part using an MCMC method.

To get a better understanding of the molecular gas, more data would be required. Low resolution observations in which the source is unresolved help in better measuring the total flux density which in turn allows for a better estimate of the molecular gas mass. The flux density can already be measured relatively well from the clean MFS maps, although there might be some missing flux in the CO(2-1) emission due to a lack in sensitivity. More observations would help in possibly picking up this emission. For the CO(2-1) emission, this could in principle be tested by applying the amplitude calibration for the first dataset to the other two, but it would be better to get additional observations with proper calibration.

In order to study the dynamics of the gas the signal-to-noise-ratio should be improved a little further such that velocity and possibly dispersion maps can be made. After that dynamic modeling of the line will be necessary in order to see if the double peak in the spectrum is consistent with a rotating disk, or something else. Without more detailed velocity information it is also difficult to discern whether MM18423+5938 is fueled by smooth accretion or has had a merger interaction in the past.

Additional observations that may prove useful would be high-resolution imaging at 1.4 GHz. The source is much brighter at this frequency as compared to 5 GHz. At 5 GHz there is apparently no association between the continuum and a more diffuse CO component to the south-west. Perhaps these additional observations will reveal if there is indeed no continuum emission at all coming from this region or, at the very least, it provides additional data to constrain the lens model.

All in all MM18423+5938 turned out to be a more complex object than first thought. Its morphology is more complex than one might assume at a first glance. The lensing galaxy is composed of two components, possibly two interacting galaxies. In NIR emission the system appears possibly quadruply imaged, but in the radio continuum we only confirm two of the four images. Finally there is a diffuse tail of emission to the south-west which might be associated with the gas in the source plane, but cannot be decidedly ruled out to be part of the lens plane. MM18423+5938 is an interesting object that would benefit well from further studies.

Bibliography

In:

- Barger, A. J. et al. (1998). "Submillimetre-wavelength detection of dusty star-forming galaxies at high redshift". In: *Nature* 394, pp. 248–251. DOI: [10.1038/28338](https://doi.org/10.1038/28338). eprint: [astro-ph/9806317](https://arxiv.org/abs/astro-ph/9806317).
- Barkana, R. and A. Loeb (2001). "In the beginning: the first sources of light and the reionization of the universe". In: *Phys. Rep.* 349, pp. 125–238. DOI: [10.1016/S0370-1573\(01\)00019-9](https://doi.org/10.1016/S0370-1573(01)00019-9). eprint: [astro-ph/0010468](https://arxiv.org/abs/astro-ph/0010468).
- Bartelmann, M. and P. Schneider (2001). "Weak gravitational lensing". In: *Phys. Rep.* 340, pp. 291–472. DOI: [10.1016/S0370-1573\(00\)00082-X](https://doi.org/10.1016/S0370-1573(00)00082-X). eprint: [astro-ph/9912508](https://arxiv.org/abs/astro-ph/9912508).
- Bell, E. F. (2003). "Estimating Star Formation Rates from Infrared and Radio Luminosities: The Origin of the Radio-Infrared Correlation". In: *ApJ* 586, pp. 794–813. DOI: [10.1086/367829](https://doi.org/10.1086/367829). eprint: [astro-ph/0212121](https://arxiv.org/abs/astro-ph/0212121).
- Bertoldi, F. et al. (2007). "COSBO: The MAMBO 1.2 Millimeter Imaging Survey of the COSMOS Field". In: *ApJS* 172, pp. 132–149. DOI: [10.1086/520511](https://doi.org/10.1086/520511).
- Bouwens, R. J. et al. (2016). "The Bright End of the $z \sim 9$ and $z \sim 10$ UV Luminosity Functions Using All Five CANDELS Fields*". In: *ApJ* 830, 67, p. 67. DOI: [10.3847/0004-637X/830/2/67](https://doi.org/10.3847/0004-637X/830/2/67). arXiv: [1506.01035](https://arxiv.org/abs/1506.01035).
- Bull, P. et al. (2016). "Beyond Λ CDM: Problems, solutions, and the road ahead". In: *Physics of the Dark Universe* 12, pp. 56–99. DOI: [10.1016/j.dark.2016.02.001](https://doi.org/10.1016/j.dark.2016.02.001). arXiv: [1512.05356](https://arxiv.org/abs/1512.05356).
- Carilli, C. (2011). *Characterizing a gravitational lens in the molecular Einstein ring SMG 18423+5938*. HST Proposal.
- Carilli, C. L. and F. Walter (2013). "Cool Gas in High-Redshift Galaxies". In: *ARAA* 51, pp. 105–161. DOI: [10.1146/annurev-astro-082812-140953](https://doi.org/10.1146/annurev-astro-082812-140953). arXiv: [1301.0371](https://arxiv.org/abs/1301.0371).
- Carilli, C. L. et al. (2007). "Radio and Millimeter Properties of $z \sim 5.7$ Ly α Emitters in the COSMOS Field: Limits on Radio AGNs, Submillimeter Galaxies, and Dust Obscuration". In: *ApJS* 172, pp. 518–522. DOI: [10.1086/516595](https://doi.org/10.1086/516595). eprint: [astro-ph/0612346](https://arxiv.org/abs/astro-ph/0612346).
- Carilli, C. L. et al. (2010). "Imaging the Molecular Gas in a Submillimeter Galaxy at $z = 4.05$: Cold Mode Accretion or a Major Merger?". In: *ApJ* 714, pp. 1407–1417. DOI: [10.1088/0004-637X/714/2/1407](https://doi.org/10.1088/0004-637X/714/2/1407). arXiv: [1002.3838](https://arxiv.org/abs/1002.3838).
- Carilli, C. L. et al. (2011). "Expanded Very Large Array Observations of a Proto-cluster of Molecular Gas-rich Galaxies at $z = 4.05$ ". In: *ApJ* 739, L33, p. L33. DOI: [10.1088/2041-8205/739/1/L33](https://doi.org/10.1088/2041-8205/739/1/L33). arXiv: [1105.2451](https://arxiv.org/abs/1105.2451).
- Casey, C. M. et al. (2009). "A search for neutral carbon towards two $z = 4.05$ submillimetre galaxies, GN20 and GN20.2". In: *MNRAS* 400, pp. 670–676. DOI: [10.1111/j.1365-2966.2009.15517.x](https://doi.org/10.1111/j.1365-2966.2009.15517.x). arXiv: [0908.3675](https://arxiv.org/abs/0908.3675).

- Casey, C. M. et al. (2014). “Dusty star-forming galaxies at high redshift”. In: *Phys. Rep.* 541, pp. 45–161. doi: [10.1016/j.physrep.2014.02.009](https://doi.org/10.1016/j.physrep.2014.02.009). arXiv: [1402.1456](https://arxiv.org/abs/1402.1456).
- Chapman, S. C. et al. (2003). “A median redshift of 2.4 for galaxies bright at submillimetre wavelengths”. In: *Nature* 422, pp. 695–698. doi: [10.1038/nature01540](https://doi.org/10.1038/nature01540). eprint: [astro-ph/0304235](https://arxiv.org/abs/astro-ph/0304235).
- Chapman, S. C. et al. (2010). “Herschel-SPIRE, far-infrared properties of millimetre-bright and -faint radio galaxies”. In: *MNRAS* 409, pp. L13–L18. doi: [10.1111/j.1745-3933.2010.00956.x](https://doi.org/10.1111/j.1745-3933.2010.00956.x). arXiv: [1009.3001](https://arxiv.org/abs/1009.3001).
- Collett, T. E. (2015). “The Population of Galaxy-Galaxy Strong Lenses in Forthcoming Optical Imaging Surveys”. In: *ApJ* 811, 20, p. 20. doi: [10.1088/0004-637X/811/1/20](https://doi.org/10.1088/0004-637X/811/1/20). arXiv: [1507.02657](https://arxiv.org/abs/1507.02657).
- Condon, J. J. (1992). “Radio emission from normal galaxies”. In: *ARA&A* 30, pp. 575–611. doi: [10.1146/annurev.aa.30.090192.003043](https://doi.org/10.1146/annurev.aa.30.090192.003043).
- Coppin, K. et al. (2010). “Mid-infrared Spectroscopy of Candidate Active Galactic Nuclei-dominated Submillimeter Galaxies”. In: *ApJ* 713, pp. 503–519. doi: [10.1088/0004-637X/713/1/503](https://doi.org/10.1088/0004-637X/713/1/503). arXiv: [1003.0447](https://arxiv.org/abs/1003.0447).
- Daddi, E. et al. (2009). “Two Bright Submillimeter Galaxies in a $z = 4.05$ Protocluster in Goods-North, and Accurate Radio-Infrared Photometric Redshifts”. In: *ApJ* 694, pp. 1517–1538. doi: [10.1088/0004-637X/694/2/1517](https://doi.org/10.1088/0004-637X/694/2/1517). arXiv: [0810.3108](https://arxiv.org/abs/0810.3108).
- Dahlen, T. et al. (2010). *Dithering strategies for WFC3*. Tech. rep.
- Davé, R. et al. (2010). “The nature of submillimetre galaxies in cosmological hydrodynamic simulations”. In: *MNRAS* 404, pp. 1355–1368. doi: [10.1111/j.1365-2966.2010.16395.x](https://doi.org/10.1111/j.1365-2966.2010.16395.x). arXiv: [0909.4078](https://arxiv.org/abs/0909.4078).
- Dekel, A. and J. P. Ostriker, eds. (1999). *Formation of Structure in the Universe*, p. 486.
- Dekel, A. et al. (2009). “Cold streams in early massive hot haloes as the main mode of galaxy formation”. In: *Nature* 457, pp. 451–454. doi: [10.1038/nature07648](https://doi.org/10.1038/nature07648). arXiv: [0808.0553](https://arxiv.org/abs/0808.0553).
- Downes, D. and P. M. Solomon (1998). “Rotating Nuclear Rings and Extreme Starbursts in Ultraluminous Galaxies”. In: *ApJ* 507, pp. 615–654. doi: [10.1086/306339](https://doi.org/10.1086/306339). eprint: [astro-ph/9806377](https://arxiv.org/abs/astro-ph/9806377).
- Dressel, L. (2016). *Wide Field Camera 3 Instrument Handbook, Version 8.0*. Baltimore: STScI.
- Duarte Puertas, S. et al. (2017). “Aperture-free star formation rate of SDSS star-forming galaxies”. In: *A&A* 599, A71, A71. doi: [10.1051/0004-6361/201629044](https://doi.org/10.1051/0004-6361/201629044). arXiv: [1611.07935](https://arxiv.org/abs/1611.07935).
- Eales, S. et al. (2010). “The Herschel ATLAS”. In: *PASP* 122, p. 499. doi: [10.1086/653086](https://doi.org/10.1086/653086). arXiv: [0910.4279](https://arxiv.org/abs/0910.4279).
- Ellis, R. S. (2010). “Gravitational lensing: a unique probe of dark matter and dark energy”. In: *Philosophical Transactions of the Royal Society of London Series A* 368, pp. 967–987. doi: [10.1098/rsta.2009.0209](https://doi.org/10.1098/rsta.2009.0209).
- Engel, H. et al. (2010). “Most Submillimeter Galaxies are Major Mergers”. In: *ApJ* 724, pp. 233–243. doi: [10.1088/0004-637X/724/1/233](https://doi.org/10.1088/0004-637X/724/1/233).
- Farnes, J. S. et al. (2014). “Faraday Rotation from Magnesium II Absorbers toward Polarized Background Radio Sources”. In: *ApJ* 795, 63, p. 63. doi: [10.1088/0004-637X/795/1/63](https://doi.org/10.1088/0004-637X/795/1/63). arXiv: [1406.2526](https://arxiv.org/abs/1406.2526).
- Finlator, K. et al. (2006). “The Physical and Photometric Properties of High-Redshift Galaxies in Cosmological Hydrodynamic Simulations”. In: *ApJ* 639, pp. 672–694. doi: [10.1086/499349](https://doi.org/10.1086/499349). eprint: [astro-ph/0507719](https://arxiv.org/abs/astro-ph/0507719).
- Fruer, D. T. et al. (2011). “Green Bank Telescope Zpectrometer CO(1-0) Observations of the Strongly Lensed Submillimeter Galaxies from the Herschel ATLAS”. In: *ApJ* 726, L22, p. L22. doi: [10.1088/2041-8205/726/2/L22](https://doi.org/10.1088/2041-8205/726/2/L22). arXiv: [1009.2194](https://arxiv.org/abs/1009.2194).

- Fruchter, A. S. and R. N. Hook (2002). “Drizzle: A Method for the Linear Reconstruction of Undersampled Images”. In: *PASP* 114, pp. 144–152. doi: [10.1086/338393](https://doi.org/10.1086/338393). eprint: [astro-ph/9808087](https://arxiv.org/abs/astro-ph/9808087).
- Genel, S. et al. (2014). “Introducing the Illustris project: the evolution of galaxy populations across cosmic time”. In: *MNRAS* 445, pp. 175–200. doi: [10.1093/mnras/stu1654](https://doi.org/10.1093/mnras/stu1654). arXiv: [1405.3749](https://arxiv.org/abs/1405.3749).
- Gonzaga, S. et al. (2012). *The DrizzlePac Handbook*.
- Hainline, L. J. et al. (2009). “A Mid-Infrared Imaging Survey of Submillimeter-Selected Galaxies with the Spitzer Space Telescope”. In: *ApJ* 699, pp. 1610–1632. doi: [10.1088/0004-637X/699/2/1610](https://doi.org/10.1088/0004-637X/699/2/1610).
- Harwit, M. and F. Pacini (1975). “Infrared galaxies - Evolutionary stages of massive star formation”. In: *ApJ* 200, pp. L127–L129. doi: [10.1086/181913](https://doi.org/10.1086/181913).
- Helou, G. et al. (1985). “Thermal infrared and nonthermal radio - Remarkable correlation in disks of galaxies”. In: *ApJ* 298, pp. L7–L11. doi: [10.1086/184556](https://doi.org/10.1086/184556).
- Helou, G. et al. (1988). “IRAS observations of galaxies in the Virgo cluster area”. In: *ApJS* 68, pp. 151–172. doi: [10.1086/191285](https://doi.org/10.1086/191285).
- Hodge, J. A. et al. (2011). “CO in GN20: The Nature of a $z=4$ Submillimeter Galaxy”. In: *ArXiv e-prints*. arXiv: [1112.3480](https://arxiv.org/abs/1112.3480) [[astro-ph.CO](https://arxiv.org/abs/astro-ph.CO)].
- Hodge, J. A. et al. (2012). “Evidence for a Clumpy, Rotating Gas Disk in a Submillimeter Galaxy at $z = 4$ ”. In: *ApJ* 760, 11, p. 11. doi: [10.1088/0004-637X/760/1/11](https://doi.org/10.1088/0004-637X/760/1/11). arXiv: [1209.2418](https://arxiv.org/abs/1209.2418).
- Hodge, J. A. et al. (2015). “The Kiloparsec-scale Star Formation Law at Redshift 4: Widespread, Highly Efficient Star Formation in the Dust-obscured Starburst Galaxy GN20”. In: *ApJ* 798, L18, p. L18. doi: [10.1088/2041-8205/798/1/L18](https://doi.org/10.1088/2041-8205/798/1/L18). arXiv: [1412.2132](https://arxiv.org/abs/1412.2132).
- Högbom, J. A. (1974). “Aperture Synthesis with a Non-Regular Distribution of Interferometer Baselines”. In: *A&AS* 15, p. 417.
- Huang, J.-S. et al. (2014). “HerMES: Spectral Energy Distributions of Submillimeter Galaxies at $z > 4$ ”. In: *ApJ* 784, 52, p. 52. doi: [10.1088/0004-637X/784/1/52](https://doi.org/10.1088/0004-637X/784/1/52). arXiv: [1401.6079](https://arxiv.org/abs/1401.6079).
- Ikarashi, S. et al. (2017). “Extremely Red Submillimeter Galaxies: New $z \sim 4$ -6 Candidates Discovered using ALMA and Jansky VLA”. In: *ApJ* 835, 286, p. 286. doi: [10.3847/1538-4357/835/2/286](https://doi.org/10.3847/1538-4357/835/2/286). arXiv: [1701.01448](https://arxiv.org/abs/1701.01448).
- Intema, H. T. et al. (2017). “The GMRT 150 MHz all-sky radio survey. First alternative data release TGSS ADR1”. In: *A&A* 598, A78, A78. doi: [10.1051/0004-6361/201628536](https://doi.org/10.1051/0004-6361/201628536). arXiv: [1603.04368](https://arxiv.org/abs/1603.04368).
- Ivison, R. J. et al. (2010a). “Herschel and SCUBA-2 imaging and spectroscopy of a bright, lensed submillimetre galaxy at $z = 2.3$ ”. In: *A&A* 518, L35, p. L35. doi: [10.1051/0004-6361/201014548](https://doi.org/10.1051/0004-6361/201014548). arXiv: [1005.1071](https://arxiv.org/abs/1005.1071).
- Ivison, R. J. et al. (2010b). “The far-infrared/radio correlation as probed by Herschel”. In: *A&A* 518, L31, p. L31. doi: [10.1051/0004-6361/201014552](https://doi.org/10.1051/0004-6361/201014552). arXiv: [1005.1072](https://arxiv.org/abs/1005.1072).
- Kennicutt Jr., R. C. (1998a). “Star Formation in Galaxies Along the Hubble Sequence”. In: *ARA&A* 36, pp. 189–232. doi: [10.1146/annurev.astro.36.1.189](https://doi.org/10.1146/annurev.astro.36.1.189). eprint: [astro-ph/9807187](https://arxiv.org/abs/astro-ph/9807187).
- (1998b). “The Global Schmidt Law in Star-forming Galaxies”. In: *ApJ* 498, pp. 541–552. doi: [10.1086/305588](https://doi.org/10.1086/305588). eprint: [astro-ph/9712213](https://arxiv.org/abs/astro-ph/9712213).
- Kereš, D. et al. (2009). “Galaxies in a simulated Λ CDM Universe - I. Cold mode and hot cores”. In: *MNRAS* 395, pp. 160–179. doi: [10.1111/j.1365-2966.2009.14541.x](https://doi.org/10.1111/j.1365-2966.2009.14541.x). arXiv: [0809.1430](https://arxiv.org/abs/0809.1430).
- Klypin, A. et al. (1999). “Where Are the Missing Galactic Satellites?” In: *ApJ* 522, pp. 82–92. doi: [10.1086/307643](https://doi.org/10.1086/307643). eprint: [astro-ph/9901240](https://arxiv.org/abs/astro-ph/9901240).

- Koekemoer, A. M. et al. (2002). *HST Dither Handbook*.
- Koopmans, L. V. E. (2005). “Gravitational imaging of cold dark matter substructures”. In: *MNRAS* 363, pp. 1136–1144. doi: [10.1111/j.1365-2966.2005.09523.x](https://doi.org/10.1111/j.1365-2966.2005.09523.x). eprint: [astro-ph/0501324](https://arxiv.org/abs/astro-ph/0501324).
- Kormann, R. et al. (1994). “Isothermal elliptical gravitational lens models”. In: *A&A* 284, pp. 285–299.
- Lestrade, J.-F. et al. (2009). “Search for cold debris disks around M-dwarfs. II”. In: *A&A* 506, pp. 1455–1467. doi: [10.1051/0004-6361/200912306](https://doi.org/10.1051/0004-6361/200912306). arXiv: [0907.4782](https://arxiv.org/abs/0907.4782).
- Lestrade, J.-F. et al. (2010). “Discovery of an extremely bright submillimeter galaxy at $z = 3.93$ ”. In: *A&A* 522, L4, p. L4. doi: [10.1051/0004-6361/201015673](https://doi.org/10.1051/0004-6361/201015673). arXiv: [1009.0449](https://arxiv.org/abs/1009.0449).
- Lestrade, J.-F. et al. (2011). “A Molecular Einstein Ring Toward the $z = 3.93$ Submillimeter Galaxy MM18423+5938”. In: *ApJ* 739, L30, p. L30. doi: [10.1088/2041-8205/739/1/L30](https://doi.org/10.1088/2041-8205/739/1/L30). arXiv: [1106.1432](https://arxiv.org/abs/1106.1432).
- Licquia, T. C. and J. A. Newman (2015). “Improved Estimates of the Milky Way’s Stellar Mass and Star Formation Rate from Hierarchical Bayesian Meta-Analysis”. In: *ApJ* 806, 96, p. 96. doi: [10.1088/0004-637X/806/1/96](https://doi.org/10.1088/0004-637X/806/1/96). arXiv: [1407.1078](https://arxiv.org/abs/1407.1078).
- Lima, M. et al. (2010). “Submillimeter Galaxy Number Counts and Magnification by Galaxy Clusters”. In: *ApJ* 717, pp. L31–L36. doi: [10.1088/2041-8205/717/1/L31](https://doi.org/10.1088/2041-8205/717/1/L31). arXiv: [1004.4889](https://arxiv.org/abs/1004.4889).
- Madau, P. and M. Dickinson (2014). “Cosmic Star-Formation History”. In: *ARA&A* 52, pp. 415–486. doi: [10.1146/annurev-astro-081811-125615](https://doi.org/10.1146/annurev-astro-081811-125615). arXiv: [1403.0007](https://arxiv.org/abs/1403.0007).
- Matthews, B. (2007). *KPOT_bmatthew_1: DEBRIS: Disc Emission via a Bias-free Reconnaissance in the Infrared/Sub-millimetre*. Herschel Space Observatory Proposal, id.86.
- McKean, J. P. et al. (2011). “A new perspective on the submillimetre galaxy MM 18423+5938 at redshift 3.9296 from radio continuum imaging”. In: *MNRAS* 414, pp. L11–L15. doi: [10.1111/j.1745-3933.2011.01043.x](https://doi.org/10.1111/j.1745-3933.2011.01043.x). arXiv: [1103.0583](https://arxiv.org/abs/1103.0583) [[astro-ph](https://arxiv.org/abs/astro-ph).CO].
- Miettinen, O. et al. (2017). “(Sub)millimetre interferometric imaging of a sample of COSMOS/AzTEC submillimetre galaxies. IV. Physical properties derived from spectral energy distributions”. In: *A&A* 597, A5, A5. doi: [10.1051/0004-6361/201628128](https://doi.org/10.1051/0004-6361/201628128). arXiv: [1609.01157](https://arxiv.org/abs/1609.01157).
- Moore, B. et al. (1999). “Dark Matter Substructure within Galactic Halos”. In: *ApJ* 524, pp. L19–L22. doi: [10.1086/312287](https://doi.org/10.1086/312287). eprint: [astro-ph/9907411](https://arxiv.org/abs/astro-ph/9907411).
- Moustakas, L. A. and R. B. Metcalf (2003). “Detecting dark matter substructure spectroscopically in strong gravitational lenses”. In: *MNRAS* 339, pp. 607–615. doi: [10.1046/j.1365-8711.2003.06055.x](https://doi.org/10.1046/j.1365-8711.2003.06055.x). eprint: [astro-ph/0206176](https://arxiv.org/abs/astro-ph/0206176).
- Murphy, E. J. (2009). “The Far-Infrared-Radio Correlation at High Redshifts: Physical Considerations and Prospects for the Square Kilometer Array”. In: *ApJ* 706, pp. 482–496. doi: [10.1088/0004-637X/706/1/482](https://doi.org/10.1088/0004-637X/706/1/482). arXiv: [0910.0011](https://arxiv.org/abs/0910.0011).
- Narayanan, D. et al. (2009). “The star-forming molecular gas in high-redshift Submillimetre Galaxies”. In: *MNRAS* 400, pp. 1919–1935. doi: [10.1111/j.1365-2966.2009.15581.x](https://doi.org/10.1111/j.1365-2966.2009.15581.x). arXiv: [0905.2184](https://arxiv.org/abs/0905.2184).
- Narayanan, D. et al. (2015). “The formation of submillimetre-bright galaxies from gas infall over a billion years”. In: *Nature* 525, pp. 496–499. doi: [10.1038/nature15383](https://doi.org/10.1038/nature15383). arXiv: [1509.06377](https://arxiv.org/abs/1509.06377).
- Nguyen, H. T. et al. (2010). “HerMES: The SPIRE confusion limit”. In: *A&A* 518, L5, p. L5. doi: [10.1051/0004-6361/201014680](https://doi.org/10.1051/0004-6361/201014680). arXiv: [1005.2207](https://arxiv.org/abs/1005.2207).
- Nierenberg, A. M. et al. (2017). “Probing dark matter substructure in the gravitational lens HE0435-1223 with the WFC3 grism”. In: *ArXiv e-prints*. arXiv: [1701.05188](https://arxiv.org/abs/1701.05188).

- Oesch, P. A. et al. (2016). “A Remarkably Luminous Galaxy at $z=11.1$ Measured with Hubble Space Telescope Grism Spectroscopy”. In: *ApJ* 819, 129, p. 129. doi: [10.3847/0004-637X/819/2/129](https://doi.org/10.3847/0004-637X/819/2/129). arXiv: [1603.00461](https://arxiv.org/abs/1603.00461).
- Oliver, S. J. et al. (2012). “The Herschel Multi-tiered Extragalactic Survey: HerMES”. In: *MNRAS* 424, pp. 1614–1635. doi: [10.1111/j.1365-2966.2012.20912.x](https://doi.org/10.1111/j.1365-2966.2012.20912.x). arXiv: [1203.2562](https://arxiv.org/abs/1203.2562).
- Pearson, E. A. et al. (2013). “H-ATLAS: estimating redshifts of Herschel sources from sub-mm fluxes”. In: *MNRAS* 435, pp. 2753–2763. doi: [10.1093/mnras/stt1369](https://doi.org/10.1093/mnras/stt1369). arXiv: [1308.5681](https://arxiv.org/abs/1308.5681).
- Peng, C. Y. et al. (2002). “Detailed Structural Decomposition of Galaxy Images”. In: *AJ* 124, pp. 266–293. doi: [10.1086/340952](https://doi.org/10.1086/340952). eprint: [astro-ph/0204182](https://arxiv.org/abs/astro-ph/0204182).
- Perley, R. A. and B. J. Butler (2013). “An Accurate Flux Density Scale from 1 to 50 GHz”. In: *ApJS* 204, 19, p. 19. doi: [10.1088/0067-0049/204/2/19](https://doi.org/10.1088/0067-0049/204/2/19). arXiv: [1211.1300](https://arxiv.org/abs/1211.1300) [[astro-ph](https://arxiv.org/abs/astro-ph).IM].
- Planck Collaboration et al. (2016). “Planck 2015 results. XIII. Cosmological parameters”. In: *A&A* 594, A13, A13. doi: [10.1051/0004-6361/201525830](https://doi.org/10.1051/0004-6361/201525830). arXiv: [1502.01589](https://arxiv.org/abs/1502.01589).
- Pooley, D. et al. (2009). “The Dark-matter Fraction in the Elliptical Galaxy Lensing the Quasar PG 1115+080”. In: *ApJ* 697, pp. 1892–1900. doi: [10.1088/0004-637X/697/2/1892](https://doi.org/10.1088/0004-637X/697/2/1892). arXiv: [0808.3299](https://arxiv.org/abs/0808.3299).
- Riechers, D. A. (2011). “Molecular Gas in Lensed $z > 2$ Quasar Host Galaxies and the Star Formation Law for Galaxies with Luminous Active Galactic Nuclei”. In: *ApJ* 730, 108, p. 108. doi: [10.1088/0004-637X/730/2/108](https://doi.org/10.1088/0004-637X/730/2/108). arXiv: [1101.5624](https://arxiv.org/abs/1101.5624).
- Riechers, D. A. et al. (2011a). “Extended Cold Molecular Gas Reservoirs in $z \sim 3.4$ Submillimeter Galaxies”. In: *ApJ* 739, L31, p. L31. doi: [10.1088/2041-8205/739/1/L31](https://doi.org/10.1088/2041-8205/739/1/L31). arXiv: [1105.4177](https://arxiv.org/abs/1105.4177) [[astro-ph](https://arxiv.org/abs/astro-ph).CO].
- Riechers, D. A. et al. (2011b). “Imaging the Molecular Gas Properties of a Major Merger Driving the Evolution of a $z = 2.5$ Submillimeter Galaxy”. In: *ApJ* 733, L11, p. L11. doi: [10.1088/2041-8205/733/1/L11](https://doi.org/10.1088/2041-8205/733/1/L11). arXiv: [1104.4348](https://arxiv.org/abs/1104.4348) [[astro-ph](https://arxiv.org/abs/astro-ph).CO].
- Riechers, D. A. et al. (2017). “Rise of the Titans: A Dusty, Hyper-Luminous “870 micron Riser” Galaxy at $z \sim 6$ ”. In: *ArXiv e-prints*. arXiv: [1705.09660](https://arxiv.org/abs/1705.09660).
- Robitaille, T. P. and B. A. Whitney (2010). “The Galactic star formation rate as seen by the Spitzer Space Telescope”. In: *Highlights of Astronomy* 15, pp. 799–799. doi: [10.1017/S1743921310011774](https://doi.org/10.1017/S1743921310011774).
- Rothberg, B. et al. (2013). “Unveiling the σ -discrepancy. II. Revisiting the Evolution of ULIRGs and the Origin of Quasars”. In: *ApJ* 767, 72, p. 72. doi: [10.1088/0004-637X/767/1/72](https://doi.org/10.1088/0004-637X/767/1/72). arXiv: [1302.1680](https://arxiv.org/abs/1302.1680).
- Rowan-Robinson, M. et al. (2017). “Extreme submillimetre starburst galaxies”. In: *ArXiv e-prints*. arXiv: [1704.07783](https://arxiv.org/abs/1704.07783).
- Rybak, M. et al. (2015a). “ALMA imaging of SDP.81 - I. A pixelated reconstruction of the far-infrared continuum emission”. In: *MNRAS* 451, pp. L40–L44. doi: [10.1093/mnrasl/slv058](https://doi.org/10.1093/mnrasl/slv058). arXiv: [1503.02025](https://arxiv.org/abs/1503.02025).
- Rybak, M. et al. (2015b). “ALMA imaging of SDP.81 - II. A pixelated reconstruction of the CO emission lines”. In: *MNRAS* 453, pp. L26–L30. doi: [10.1093/mnrasl/slv092](https://doi.org/10.1093/mnrasl/slv092). arXiv: [1506.01425](https://arxiv.org/abs/1506.01425).
- Scott, K. S. et al. (2008). “AzTEC millimetre survey of the COSMOS field - I. Data reduction and source catalogue”. In: *MNRAS* 385, pp. 2225–2238. doi: [10.1111/j.1365-2966.2008.12989.x](https://doi.org/10.1111/j.1365-2966.2008.12989.x). arXiv: [0801.2779](https://arxiv.org/abs/0801.2779).
- Siudek, M. et al. (2017). “The VIMOS Public Extragalactic Redshift Survey (VIPERS). Star formation history of passive red galaxies”. In: *A&A* 597, A107, A107. doi: [10.1051/0004-6361/201628951](https://doi.org/10.1051/0004-6361/201628951). arXiv: [1605.05503](https://arxiv.org/abs/1605.05503).

- Smail, I. et al. (1997). "A Deep Sub-millimeter Survey of Lensing Clusters: A New Window on Galaxy Formation and Evolution". In: *ApJ* 490, pp. L5–L8. doi: [10.1086/311017](https://doi.org/10.1086/311017). eprint: [astro-ph/9708135](https://arxiv.org/abs/astro-ph/9708135).
- Soifer, B. T. et al. (1986). "The luminosity function and space density of the most luminous galaxies in the IRAS survey". In: *ApJ* 303, pp. L41–L44. doi: [10.1086/184649](https://doi.org/10.1086/184649).
- Solomon, P. M. et al. (1992). "Warm molecular gas in the primeval galaxy IRAS 10214 + 4724". In: *ApJ* 398, pp. L29–L32. doi: [10.1086/186569](https://doi.org/10.1086/186569).
- Spilker, J. S. et al. (2014). "The Rest-frame Submillimeter Spectrum of High-redshift, Dusty, Star-forming Galaxies". In: *ApJ* 785, 149, p. 149. doi: [10.1088/0004-637X/785/2/149](https://doi.org/10.1088/0004-637X/785/2/149). arXiv: [1403.1667](https://arxiv.org/abs/1403.1667).
- Springel, V. et al. (2005). "Simulations of the formation, evolution and clustering of galaxies and quasars". In: *Nature* 435, pp. 629–636. doi: [10.1038/nature03597](https://doi.org/10.1038/nature03597). eprint: [astro-ph/0504097](https://arxiv.org/abs/astro-ph/0504097).
- Springel, V. et al. (2006). "The large-scale structure of the Universe". In: *Nature* 440, pp. 1137–1144. doi: [10.1038/nature04805](https://doi.org/10.1038/nature04805). eprint: [astro-ph/0604561](https://arxiv.org/abs/astro-ph/0604561).
- Strigari, L. E. et al. (2008). "A common mass scale for satellite galaxies of the Milky Way". In: *Nature* 454, pp. 1096–1097. doi: [10.1038/nature07222](https://doi.org/10.1038/nature07222). arXiv: [0808.3772](https://arxiv.org/abs/0808.3772).
- Tacconi, L. J. et al. (2008). "Submillimeter Galaxies at $z \sim 2$: Evidence for Major Mergers and Constraints on Lifetimes, IMF, and CO-H₂ Conversion Factor". In: *ApJ* 680, 246–262, pp. 246–262. doi: [10.1086/587168](https://doi.org/10.1086/587168). arXiv: [0801.3650](https://arxiv.org/abs/0801.3650).
- Tasca, L. A. M. et al. (2015). "The evolving star formation rate: M_{\star} relation and sSFR since $z \sim 5$ from the VUDS spectroscopic survey". In: *A&A* 581, A54, A54. doi: [10.1051/0004-6361/201425379](https://doi.org/10.1051/0004-6361/201425379). arXiv: [1411.5687](https://arxiv.org/abs/1411.5687).
- Taylor, G. B. et al., eds. (1999). *Synthesis Imaging in Radio Astronomy II*. Vol. 180. Astronomical Society of the Pacific Conference Series.
- Toft, S. et al. (2014). "Submillimeter Galaxies as Progenitors of Compact Quiescent Galaxies". In: *ApJ* 782, 68, p. 68. doi: [10.1088/0004-637X/782/2/68](https://doi.org/10.1088/0004-637X/782/2/68). arXiv: [1401.1510](https://arxiv.org/abs/1401.1510).
- Treu, T. (2010). "Strong Lensing by Galaxies". In: *ARA&A* 48, pp. 87–125. doi: [10.1146/annurev-astro-081309-130924](https://doi.org/10.1146/annurev-astro-081309-130924). arXiv: [1003.5567](https://arxiv.org/abs/1003.5567).
- Vegetti, S. and L. V. E. Koopmans (2009). "Bayesian strong gravitational-lens modelling on adaptive grids: objective detection of mass substructure in Galaxies". In: *MNRAS* 392, pp. 945–963. doi: [10.1111/j.1365-2966.2008.14005.x](https://doi.org/10.1111/j.1365-2966.2008.14005.x). arXiv: [0805.0201](https://arxiv.org/abs/0805.0201).
- Vieira, J. D. et al. (2013). "Dusty starburst galaxies in the early Universe as revealed by gravitational lensing". In: *Nature* 495, pp. 344–347. doi: [10.1038/nature12001](https://doi.org/10.1038/nature12001). arXiv: [1303.2723](https://arxiv.org/abs/1303.2723).
- Vogelsberger, M. et al. (2014). "Introducing the Illustris Project: simulating the coevolution of dark and visible matter in the Universe". In: *MNRAS* 444, pp. 1518–1547. doi: [10.1093/mnras/stu1536](https://doi.org/10.1093/mnras/stu1536). arXiv: [1405.2921](https://arxiv.org/abs/1405.2921).
- Walker, M. G. and J. Peñarrubia (2011). "A Method for Measuring (Slopes of) the Mass Profiles of Dwarf Spheroidal Galaxies". In: *ApJ* 742, 20, p. 20. doi: [10.1088/0004-637X/742/1/20](https://doi.org/10.1088/0004-637X/742/1/20). arXiv: [1108.2404](https://arxiv.org/abs/1108.2404).
- White, S. D. M. and M. J. Rees (1978). "Core condensation in heavy halos - A two-stage theory for galaxy formation and clustering". In: *MNRAS* 183, pp. 341–358. doi: [10.1093/mnras/183.3.341](https://doi.org/10.1093/mnras/183.3.341).
- Wiklind, T. et al. (2014). "Properties of Submillimeter Galaxies in the CANDELS GOODS-South Field". In: *ApJ* 785, 111, p. 111. doi: [10.1088/0004-637X/785/2/111](https://doi.org/10.1088/0004-637X/785/2/111). arXiv: [1402.3268](https://arxiv.org/abs/1402.3268).

-
- Wuyts, S. et al. (2010). "On Sizes, Kinematics, M/L Gradients, and Light Profiles of Massive Compact Galaxies at $z \sim 2$ ". In: *ApJ* 722, pp. 1666–1684. doi: [10.1088/0004-637X/722/2/1666](https://doi.org/10.1088/0004-637X/722/2/1666). arXiv: [1008.4127](https://arxiv.org/abs/1008.4127).

Appendix A

VLA Calibration Script

```

1  # CASA 4.7.0 required for spectra!
2  # Automatically (mostly) calibrates a JVLA observation.
3  # Must be run with an internet connection to determine antenna
   ↪ offsets and opacity measurements.
4  DEBUG = True
5  # Definitions
6  # Observation
7  flux_calibrator = '3C286'
8  flux_calibrator_band = 'Q'
9  myconfig = 'B' #
   ↪ VLA array configuration used for the observation.
10 myband = 'Q' #
   ↪ Observing band.
11
12 # MS specific
13 msfile = '11B-002.sb10148507.eb11232355.56131.253432314814.ms'
   ↪ # Original MS file.
14 myfield = '2,4,5' #
   ↪ Fields to split into separate file.
15 myfluxref, myphaseref, mytarget = '0', '1', '2' #
   ↪ The _NEW_ indices of the fields (starting from 0 on the lowest
   ↪ field).
16 myspw = '2~17' #
   ↪ Spectral windows of interest.
17 myopacspw = '0~15' #
   ↪ Spectral windows to calculate opacities for (again NEW indices
   ↪ (i.e. 0,1...)).
18 mssplit = '11B-002.srcs_Q.ms' #
   ↪ MS file with the interesting sources from 'myfield'.
19 msscans = '11B-002.srcs_Q.ms.txt' #
   ↪ Text file to write 'listobs' output to.
20 mstarget = 'target_Q.ms' #
   ↪ MS file of the target.
21 myimage = 'target_Q_image' #
   ↪ Image.
22 mycube = 'target_Q_cube' #
   ↪ Cube.

```

```

23 mycontsub = 'target_Q.ms.contsub' #
   → Continuum subtraction.
24 skymodel = 'target_Q.model' #
   → Sky model.
25 mymask = 'target_Q.mask' #
   → Mask.
26 myrefant = 'ea05' #
   → Reference antenna.
27
28 # Spectral line and imaging parameters.
29 myrestfreq = "46.76607GHz" #
   → Spectral line redshifted rest frequency.
30 mylinespw = '5' #
   → spw containing the line.
31 mylinechannels = '20~40' #
   → Channels in the selected spw containing the line.
32 myfitorder = 1
33 mylinechannels_spectrum = '340~360' #
   → Range of channels containing the line in the full spectrum.
34
35 myimsize = 512
36 #####
37 # DO NOT EDIT BELOW THIS LINE // DO NOT EDIT BELOW THIS LINE #
38 #####
39 # Telescope parameters
40 # Band center frequencies in GHz based on https://science.nrao.edu/facilities/vla/docs/manuals/oss2013B/performance/bands
   → cilities/vla/docs/manuals/oss2013B/performance/bands
41 vla_bands = {'4':0.071, 'P':0.35, 'L':1.5, 'S':3.0, 'C':6.0,
   → 'X':10.0, 'Ku':15.0, 'K':22.25, 'Ka':33.25, 'Q':45.0}
42 # Baseline lengths in km taken from https://science.nrao.edu/facilities/vla/docs/manuals/oss/performance/resolution
   → es/vla/docs/manuals/oss/performance/resolution
43 array_baseline_max = {'A':36.4, 'B':11.1, 'C':3.4, 'D':1.03}
44 # Calculate the field of view and angular resolution.
45 mylambda = (299792458) / (vla_bands[myband] * 1e9)
46 # VLA dishes are 25m.
47 myfov = (mylambda / 25) * 206265
48 myresolution = (mylambda / (array_baseline_max[myconfig]*1e3)) *
   → 206265
49 print 'Field of view [arsec]: ', myfov
50 print 'Angular resolution [arscec]: ', myresolution
51
52 import os
53 import sys
54
55 '''
56 The Python variable 'mysteps' will control which steps
57 are executed when you start the script using
58     execfile('scriptForCalibration.py')
59 e.g. setting
60     mysteps = [2,3,4]

```

```

61 before starting the script will make the script execute
62 only steps 2, 3, and 4
63 Setting mysteps = [] will make it execute all steps.
64 '''
65 # Calibration steps
66 thesteps = [0]
67 step_title = {0: 'Set the variables and initial split (split)',
68               1: 'A priori correction of opacity, antenna elevation
        → and antenna positions (gencal)',
69               2: 'Flag bad data (flagdata)',
70               3: 'Insert model of the flux calibrator (setjy)',
71               4: 'Short phase correction (gaincal)',
72               5: 'Delay correction (gaincal)',
73               6: 'Bandpass calibration (bandpass)',
74               7: 'Gain (Amplitude and Phase) calibration (gaincal)',
75               8: 'Determine the absolute flux-scale of the
        → calibrators (fluxscale)',
76               9: 'Applying the calibration tables (applycal)',
77               10: 'Split target (split)',
78               11: 'Continuum subtraction (uvcontsub)',
79               12: 'Create dirty cubes (clean)',
80               13: 'Continuum subtraction (imcontsub)'}
81
82 try:
83     print 'List of steps to be executed ...', mysteps
84     thesteps = mysteps
85 except:
86     while 1:
87         temp = raw_input('Variable 'mysteps' not set. Execute steps
        → 0-12? (y/n)').lower()
88         if temp == 'n':
89             sys.exit(0)
90         elif temp == 'y':
91             thesteps = range(13)
92             print 'Executing steps: ', thesteps
93             break
94         else:
95             print 'Unkown option, aborting.'
96             sys.exit(0)
97
98 #####
99 # Step 0: A priori splitting #
100 mystep = 0
101 if (mystep in thesteps):
102     casalog.post('Step '+str(mystep)+' '+step_title[mystep], 'INFO')
103     print 'Step ', mystep, step_title[mystep]
104
105     # Split off the selected fields into a separate MS file.

```

```

106 split(vis=msfile, outputvis=mssplit, keepmms=True, field=myfield,
    → spw=myspw, scan="", antenna="", correlation="rr,ll",
    → timerange="", intent="", array="", uvrange="",
    → observation="", feed="", datacolumn="data", keepflags=True,
    → width=1, timebin="0s", combine="")
107
108 # List properties of the created MS file.
109 listobs(vis=mssplit, selectdata=True, spw="", field="",
    → antenna="", uvrange="", timerange="", correlation="",
    → scan="", intent="", feed="", array="", observation="",
    → verbose=True, listfile=msscans, listunfl=False, cachesize=50,
    → overwrite=True)
110 # End of step 0. #
111 #####
112
113 #####
114 # Step 1: Calibration #
115 mystep = 1
116 if (mystep in thesteps):
117     casalog.post('Step '+str(mystep)+' '+step_title[mystep], 'INFO')
118     print 'Step ', mystep, step_title[mystep]
119     # Calculate mean zenith opacity per spectral window.
120     myTau = plotweather(vis=mssplit, doPlot=T)
121     # Generate tropospheric opacity calibration table.
122     gencal(vis=mssplit, caltable="opacity.cal", caltype="opac",
    → spw=myopacspw, antenna="", pol="", parameter=myTau)
123     # Generate ITRF (International Terrestrial Reference System)
    → antenna position corrections calibration table.
124     gencal(vis=mssplit, caltable="antpos.cal", caltype="antpos",
    → spw="", antenna="", pol="", parameter=[])
125     # Generate gain curve and efficiency calibration table.
126     gencal(vis=mssplit, caltable="gaincurve.cal", caltype="gceff",
    → spw="", antenna="", pol="", parameter=[])
127
128     # Check if antenna position corrections were necessary.
129     if os.path.exists('./antpos.cal'):
130         gtables = ['opacity.cal', 'antpos.cal', 'gaincurve.cal']
131         gtables2 = ['opacity.cal', 'antpos.cal', 'gaincurve.cal']
132         gfields = ['', '', '']
133     else:
134         gtables = ['opacity.cal', 'gaincurve.cal']
135         gtables2 = ['opacity.cal', 'gaincurve.cal']
136         gfields = ['', '']
137 # End of step 1. #
138 #####
139
140 #####
141 # Step 2: Flagging #
142 mystep = 2
143 if (mystep in thesteps):
144     casalog.post('Step '+str(mystep)+' '+step_title[mystep], 'INFO')

```

```

145     print 'Step ', mystep, step_title[mystep]
146     execfile('./flagger.py')
147 # End of step 2.    #
148 #####
149
150 #####
151 # Step 3: model of the flux calibrator - setjy #
152 mystep = 3
153 if (mystep in thesteps):
154     if DEBUG:
155         print 'SETJY using model source %s_%s.im' % (flux_calibrator,
156             ↪ flux_calibrator_band)
157         casalog.post('Step '+str(mystep)+' '+step_title[mystep], 'INFO')
158         print 'Step ', mystep, step_title[mystep]
159         # Set the flux scale for field 2 (the flux calibrator) using the
160         ↪ model.
161         setjy(vis=mssplit, field=myfluxref, spw="", selectdata=False, timeran
162             ↪ ge="", scan="", intent="", observation="", scalebychan=True, stand
163             ↪ ard="Perley-Butler
164             ↪ 2010", model='%s_%s.im'%(flux_calibrator, flux_calibrator_band)
165             ↪ , modimage=None, listmodels=False, fluxdensity=-1, spix=0.0, reffr
166             ↪ eq="1GHz", polindex=[], rotmeas=0.0, fluxdict={}, useephemdir=Fal
167             ↪ se, interpolation="nearest", usescratch=True, ismms=None)
168 # End of step 3.    #
169 #####
170
171 #####
172 # Step 4: short phase calibration. #
173 # Calculate calibrations for the phase changing as function of time.
174 mystep = 4
175 if (mystep in thesteps):
176     if DEBUG:
177         print 'INTPHASE using the following calibration tables: ' +
178             ↪ ', '.join(gtables)
179         casalog.post('Step '+str(mystep)+' '+step_title[mystep], 'INFO')
180         print 'Step ', mystep, step_title[mystep]
181         # Calculate the calibrations using only a few of the central
182         ↪ channels for each spectral window such that the response is
183         ↪ essentially flat as function of frequency.
184         gaincal(vis=mssplit, caltable="intphase.cal", field=myfluxref, spw="
185             ↪ *:28~36", intent="", selectdata=False, timerange="", uvrange="", a
186             ↪ ntenna="", scan="", observation="", msselect="", solint="int", com
187             ↪ bine="", preavg=-1.0, refant=myrefant, minblperant=4, minsnr=3.0,
188             ↪ solnorm=False, gaintype="G", smodel=[], calmode="p", append=False
189             ↪ , splintime=3600.0, npointaver=3, phasewrap=180.0, docallib=Fals
190             ↪ e, callib="", gaintable=gtables, gainfield=[], interp=[], spwmap=
191             ↪ ], parang=False)
192         gtables += ['intphase.cal']
193 # End of step 4.    #
194 #####

```

```

177
178 #####
179 # Step 5: residual delay calibration. #
180 # Calculate calibrations for the phase as function of frequency.
181 mystep = 5
182 if (mystep in thesteps):
183     if DEBUG:
184         print 'DELAYS using the following calibration tables: ' +
            ↪ ', '.join(gtables)
185         casalog.post('Step '+str(mystep)+' '+step_title[mystep], 'INFO')
186         print 'Step ', mystep, step_title[mystep]
187         # Calculate calibrations for the delays between antennas.
188         gaincal(vis=mssplit, caltable="delays.cal", field=myfluxref, spw="*:
            ↪ 6~60", intent="", selectdata=False, timerange="", uvrange="", ante
            ↪ nna="", scan="", observation="", msselect="", solint="inf", combin
            ↪ e="scan", preavg=-1.0, refant=myrefant, minblperant=4, minsnr=3.0
            ↪ , solnorm=False, gaintype="K", smodel=[], calmode="p", append=Fals
            ↪ e, splinetime=3600.0, npointaver=3, phasewrap=180.0, docallib=Fal
            ↪ se, callib="", gaintable=gtables, gainfield=[], interp=[], spwmap=
            ↪ [], parang=False)
189         gtables += ['delays.cal']
190 # End of step 5. #
191 #####
192
193 #####
194 # Step 6: bandpass calibration. #
195 # Match shape of bandpass to spectrum of object.
196 mystep = 6
197 if (mystep in thesteps):
198     if DEBUG:
199         print 'BANDPASS using the following calibration tables: ' +
            ↪ ', '.join(gtables)
200         casalog.post('Step '+str(mystep)+' '+step_title[mystep], 'INFO')
201         print 'Step ', mystep, step_title[mystep]
202         # Calculate calibrations for the bandpass.
203         bandpass(vis=mssplit, caltable="bandpass.cal", field=myfluxref, spw=
            ↪ "*:6~60", intent="", selectdata=True, timerange="", uvrange="", an
            ↪ tenna="", scan="", observation="", msselect="", solint="inf", comb
            ↪ ine="scan", refant=myrefant, minblperant=4, minsnr=3.0, solnorm=F
            ↪ alse, bandtype="B", smodel=[], append=False, fillgaps=0, degamp=3,
            ↪ degphase=3, visnorm=False, maskcenter=0, maskedge=5, docallib=Fal
            ↪ se, callib="", gaintable=gtables, gainfield=[], interp=[], spwmap=
            ↪ [], parang=False)
204         gtables += ['bandpass.cal']
205         gtables.remove('intphase.cal')
206 # End of step 6. #
207 #####
208 #####
209 # Step 7: phase & amplitude calibration. #
210 # Now use the full range of channels except the ones at the edge,
            ↪ because the response drops rapidly here.

```

```

211 mystep = 7
212 if (mystep in thesteps):
213     if DEBUG:
214         print 'FULL GAINCAL using the following calibration tables: '
                ↪ + ', '.join(gtables)
215     casalog.post('Step '+str(mystep)+' '+step_title[mystep], 'INFO')
216     print 'Step ', mystep, step_title[mystep]
217     # Calculate phase calibrations for the flux calibrator.
218     gaincal(vis=mssplit, caltable="gainphase.cal", field=myfluxref, spw=
                ↪ " *:6~60", intent="", selectdata=True, timerange="", uvrage="", an
                ↪ tenna="", scan="", observation="", msselect="", solint="int", comb
                ↪ ine="", preavg=-1.0, refant=myrefant, minblperant=4, minsnr=3.0, s
                ↪ olnorm=False, gaintype="G", smodel=[], calmode="p", append=False,
                ↪ splinetime=3600.0, npointaver=3, phasewrap=180.0, docallib=False
                ↪ , callib="", gaintable=gtables, gainfield=[], interp=[], spwmap=[]
                ↪ , parang=False)
219
220     # Calculate phase calibrations for the phase reference (Note
                ↪ 'append=True').
221     gaincal(vis=mssplit, caltable="gainphase.cal", field=myphaseref, spw
                ↪ = " *:6~60", intent="", selectdata=True, timerange="", uvrage="", a
                ↪ ntenna="", scan="", observation="", msselect="", solint="int", com
                ↪ bine="", preavg=-1.0, refant=myrefant, minblperant=4, minsnr=3.0,
                ↪ solnorm=False, gaintype="G", smodel=[], calmode="p", append=True,
                ↪ splinetime=3600.0, npointaver=3, phasewrap=180.0, docallib=False
                ↪ , callib="", gaintable=gtables, gainfield=[], interp=[], spwmap=[]
                ↪ , parang=False)
222     gtables += ['gainphase.cal']
223
224     # Calculate amplitude calibrations for the flux calibrator.
225     gaincal(vis=mssplit, caltable="gainamp.cal", field=myfluxref, spw="*
                ↪ :6~60", intent="", selectdata=True, timerange="", uvrage="", ante
                ↪ nna="", scan="", observation="", msselect="", solint="inf", combin
                ↪ e="", preavg=-1.0, refant=myrefant, minblperant=4, minsnr=3.0, sol
                ↪ norm=False, gaintype="G", smodel=[], calmode="ap", append=False, s
                ↪ plinetime=3600.0, npointaver=3, phasewrap=180.0, docallib=False,
                ↪ callib="", gaintable=gtables, gainfield=gfields+[myfluxref,
                ↪ myfluxref, myfluxref], interp=[], spwmap=[], parang=False)
226
227     # Calculate amplitude calibrations for the phase reference (Note
                ↪ 'append=True').
228     gaincal(vis=mssplit, caltable="gainamp.cal", field=myphaseref, spw="
                ↪ *:6~60", intent="", selectdata=True, timerange="", uvrage="", ant
                ↪ enna="", scan="", observation="", msselect="", solint="inf", combi
                ↪ ne="", preavg=-1.0, refant=myrefant, minblperant=4, minsnr=3.0, so
                ↪ lnorm=False, gaintype="G", smodel=[], calmode="ap", append=True, s
                ↪ plinetime=3600.0, npointaver=3, phasewrap=180.0, docallib=False,
                ↪ callib="", gaintable=gtables, gainfield=gfields+[myfluxref,
                ↪ myfluxref, myphaseref], interp=[], spwmap=[], parang=False)
229     gtables += ['gainamp.cal']

```

```

230 # End of step 7. #
231 #####
232
233 #####
234 # Step 8: absolute flux-scale calibration. #
235 # Transfer the calculated calibrations from the flux calibrator (field
    → 0) to the phase calibrator (field 1). Afterwards use the
    → calibrated flux calibrator to calibrate the phase calibrator
    → (bootstrapping).
236 mystep = 8
237 if(mystep in thesteps):
238     casalog.post('Step '+str(mystep)+' '+step_title[mystep], 'INFO')
239     print 'Step ', mystep, step_title[mystep]
240     flux = fluxscale(vis=mssplit, caltable="gainamp.cal", fluxtable="flux
    → ux.cal", reference=[myfluxref], transfer=[myphaseref], listfile=
    → "", append=False, refspwmap=[-1], gainthreshold=-1.0, antenna="",
    → timerange="", scan="", incremental=True, fitorder=1, display=True)
241
242     setjy(vis=mssplit, field=myphaseref, spw="", selectdata=False, timera
    → nge="", scan="", intent="", observation="", scalebychan=True, stan
    → dard="fluxscale", model="", modimage=None, listmodels=False, flux
    → density=-1, spix=0.0, reffreq="1GHz", polindex=[], polangle=[], ro
    → tmeas=0.0, fluxdict=flux, useephemdir=False, interpolation="near
    → est", usescratch=True, ismms=None)
243
244     gaincal(vis=mssplit, caltable="intphase2.cal", field=myphaseref, spw=
    → " *:28~36", intent="", selectdata=True, timerange="", uvrange="",
    → antenna="", scan="", observation="", msselect="", solint="int", co
    → mbine="", preavg=-1.0, refant=myrefant, minblperant=4, minsnr=3.0
    → , solnorm=False, gaintype="G", smodel=[], calmode="p", append=False
    → e, splinetime=3600.0, npointaver=3, phasewrap=180.0, docallib=False
    → se, callib="", gaintable=gtables2, gainfield=[], interp=[], spwmap
    → =[], parang=False)
245     gtables2 += ['intphase2.cal']
246
247     gaincal(vis=mssplit, caltable="delays2.cal", field=myphaseref, spw="
    → *:28~36", intent="", selectdata=True, timerange="", uvrange="", an
    → tenna="", scan="", observation="", msselect="", solint="inf", comb
    → ine="scan", preavg=-1.0, refant=myrefant, minblperant=4, minsnr=3
    → .0, solnorm=False, gaintype="K", smodel=[], calmode="p", append=Fa
    → lse, splinetime=3600.0, npointaver=3, phasewrap=180.0, docallib=F
    → alse, callib="", gaintable=gtables2, gainfield=[], interp=[], spwm
    → ap=[], parang=False)
248     gtables2 += ['delays2.cal']
249

```

```

250 bandpass(vis=mssplit,caltable="bandpass2.cal",field=myphaseref,sp
    ↪ w="*:6~60",intent="",selectdata=True,timerange="",uvrage="",
    ↪ antenna="",scan="",observation="",msselect="",solint="inf",co
    ↪ mbine="scan",refant=myrefant,minblperant=4,minsnr=3.0,solnorm
    ↪ =False,bandtype="B",smodel=[],append=False,fillgaps=0,degamp=
    ↪ 3,degphase=3,visnorm=False,maskcenter=0,maskedge=5,docallib=F
    ↪ else,callib="",gaintable=gtables2,gainfield=[],interp=[],spwm
    ↪ ap=[],parang=False)
251 gtables2 += ['bandpass2.cal']
252
253 gtables2.remove('intphase2.cal')
254
255 gaincal(vis=mssplit,caltable="gainphase2.cal",field=myphaseref,sp
    ↪ w="*:6~60",intent="",selectdata=True,timerange="",uvrage="",
    ↪ antenna="",scan="",observation="",msselect="",solint="int",co
    ↪ mbine="",preavg=-1.0,refant=myrefant,minblperant=4,minsnr=3.0
    ↪ ,solnorm=False,gaintype="G",smodel=[],calmode="p",append=Fals
    ↪ e,splintime=3600.0,npointaver=3,phasewrap=180.0,docallib=Fal
    ↪ se,callib="",gaintable=gtables2,gainfield=[],interp=[],spwmap
    ↪ =[],parang=False)
256 gtables2 += ['gainphase2.cal']
257
258 gaincal(vis=mssplit,caltable="gainamp2.cal",field=myphaseref,spw=
    ↪ "*:6~60",intent="",selectdata=True,timerange="",uvrage="",an
    ↪ tenna="",scan="",observation="",msselect="",solint="int",comb
    ↪ ine="",preavg=-1.0,refant=myrefant,minblperant=4,minsnr=3.0,s
    ↪ olnorm=False,gaintype="G",smodel=[],calmode="ap",append=False
    ↪ ,splintime=3600.0,npointaver=3,phasewrap=180.0,docallib=Fals
    ↪ e,callib="",gaintable=gtables2,gainfield=[],interp=[],spwmap=
    ↪ [],parang=False)
259 gtables2 += ['gainamp2.cal']
260 # End of step 8. #
261 #####
262
263 #####
264 # End of calibration #
265 #####
266
267 #####
268 # Apply the calibration to the data. #
269 #####
270 #####
271 # Step 9: Application of the calibration tables. #
272 mystep = 9
273 if(mystep in thesteps):
274     if DEBUG:
275         print 'APPLYCAL using the following calibration tables for
    ↪ field 0: ' + ','.join(gtables)
276         print 'APPLYCAL using the following calibration tables for
    ↪ field 1: ' + ','.join(gtables2)

```

```

277 casalog.post('Step '+str(mystep)+' '+step_title[mystep],'INFO')
278 print 'Step ', mystep, step_title[mystep]
279 # Apply calibrations to the flux calibrator.
280 applycal(vis=mssplit,field=myfluxref,spw="",intent="",selectdata=
    ↪ True,timerange="",uvrange="",antenna="",scan="",observation="
    ↪ ",msselect="",docallib=False,callib="",gaintable=gtables,gain
    ↪ field=gfields+[myfluxref, myfluxref, myfluxref,
    ↪ myfluxref],interp=['linear', 'linear', 'linear', 'nearest',
    ↪ 'nearest', 'linear', 'nearest'],spwmap=[],calwt=False,parang=
    ↪ False,applymode="",flagbackup=True)
281
282 # Apply calibrations to the phase reference.
283 applycal(vis=mssplit,field=myphaseref,spw="",intent="",selectdata
    ↪ =True,timerange="",uvrange="",antenna="",scan="",observation=
    ↪ "",msselect="",docallib=False,callib="",gaintable=gtables2,ga
    ↪ infield=gfields+[myphaseref, myphaseref, myphaseref,
    ↪ myphaseref],interp=['linear', 'linear', 'linear', 'nearest',
    ↪ 'nearest', 'linear', 'nearest'],spwmap=[],calwt=False,parang=
    ↪ False,applymode="",flagbackup=True)
284
285 # Apply calibrations to the target.
286 applycal(vis=mssplit,field=mytarget,spw="",intent="",selectdata=T
    ↪ rue,timerange="",uvrange="",antenna="",scan="",observation=""
    ↪ ,msselect="",docallib=False,callib="",gaintable=gtables2,gain
    ↪ field=gfields+[myphaseref, myphaseref, myphaseref,
    ↪ myphaseref],interp=['linear', 'linear', 'linear', 'nearest',
    ↪ 'nearest', 'linear', 'nearest'],spwmap=[],calwt=False,parang=
    ↪ False,applymode="",flagbackup=True)
287 # End of step 9. #
288 #####
289
290 #####
291 # Calibration applied #
292 #####
293
294 #####
295 # Split off corrected target and create dirty image. #
296 #####
297 #####
298 # Step 10: Split off the target. #
299 mystep = 10
300 if(mystep in thesteps):
301     casalog.post('Step '+str(mystep)+' '+step_title[mystep],'INFO')
302     print 'Step ', mystep, step_title[mystep]
303     split(vis=mssplit,outputvis=mstarget,keepmms=True,field=mytarget,
    ↪ spw="",scan="",antenna="",correlation="",timerange="",intent=
    ↪ "",array="",uvrange="",observation="",feed="",datacolumn="cor
    ↪ rected",keepflags=True,width=1,timebin="0s",combine="")

```

```

304     split(vis=mssplit,outputvis='phaseref.ms',keepmms=True,field=myph
      ↪ aseref,spw="",scan="",antenna="",correlation="",timerange="",
      ↪ intent="",array="",uvrange="",observation="",feed="",datacolu
      ↪ mn="corrected",keepflags=True,width=1,timebin="0s",combine="")
305     split(vis=mssplit,outputvis='fluxref.ms',keepmms=True,field=myflu
      ↪ xref,spw="",scan="",antenna="",correlation="",timerange="",in
      ↪ tent="",array="",uvrange="",observation="",feed="",datacolumn
      ↪ ="corrected",keepflags=True,width=1,timebin="0s",combine="")
306     # End of step 10.                                     #
307     #####
308
309     #####
310     # Step 11: Subtract continuum.                         #
311     mystep = 11
312     if (mystep in thesteps):
313         uvcontsub(vis=mstarget, field='',
      ↪ fitspw=mylinespw+':'+mylinechannels, excludechans=True,
      ↪ combine='spw', solint='int', fitorder=myfitorder, spw='',
      ↪ want_cont=False)
314     # End of step 11.                                     #
315     #####
316
317     #####
318     # Step 12: Create a dirty image and/or dirty cube. #
319     mystep = 12
320     if(mystep in thesteps):
321         cellsize = (myresolution / 4)
322         mycell = '%.2farcsec'%(cellsize)
323         # If the user has specified an image size in pixels use that
      ↪ value, else set it to a default value.
324         try:
325             myimsize = int(myimsize)
326         except:
327             myimsize = int(myfov / cellsize)
328         print 'Pixel scale : ', mycell
329         print 'Image size [pixels]: ', myimsize
330         casalog.post('Step '+str(mystep)+' '+step_title[mystep],'INFO')
331         print 'Step ', mystep, step_title[mystep]
332         if 11 in thesteps:
333             print 'Creating dirty continuum subtracted cube for target.'
334         else:
335             print 'Creating dirty cube for target.'

```

```

336 clean(vis=mstarget, imagename=mycube, outlierfile="", field="", spw="
    → ", selectdata=True, timerange="", uvrange="", antenna="", scan="",
    → observation="", intent="", mode="frequency", resmooth=False, grid
    → mode="", wprojplanes=-1, facets=1, cfcache="cfcache.dir", rotpainc
    → c=5.0, painc=360.0, aterm=True, psterm=False, mterm=True, wbawp=Fa
    → lse, conjbeams=True, epjtable="", interpolation="linear", niter=0
    → , gain=0.05, threshold="6.0e-5Jy", psfmode="clark", imagermode="c
    → sclean", ftmachine="mosaic", mosweight=False, scaletype="SAULT",
    → multiscale=[], negcomponent=-1, smallscalebias=0.6, interactive=
    → False, mask="", nchan=-1, start='', width='2MHz', outframe="", vel
    → type="radio", imsize=myimsize, cell=mycell, phasecenter="", restfr
    → eq=myrestfreq, stokes="I", weighting="natural", robust=0, uvtaper
    → =False, outertaper=[''], innertaper=['1.0'], modelimage="", resto
    → ringbeam=[''], pbcor=False, minpb=0.2, usescratch=True, noise="1.
    → 0Jy", npixels=0, npercycle=100, cyclefactor=1.5, cyclespeedup=-1,
    → nterms=1, reffreq="", chaniter=False, flatnoise=True, allowchunk=
    → False)
337 #print 'Creating dirty cube for phase reference.'
338 #clean(vis='phaseref.ms', imagename='phaseref_cube.ms', outlierfile
    → = "", field="", spw="", selectdata=True, timerange="", uvrange="", a
    → ntenna="", scan="", observation="", intent="", mode="frequency", r
    → esmooth=False, gridmode="", wprojplanes=-1, facets=1, cfcache="cf
    → cache.dir", rotpainc=5.0, painc=360.0, aterm=True, psterm=False, m
    → term=True, wbawp=False, conjbeams=True, epjtable="", interpolatio
    → n="linear", niter=0, gain=0.05, threshold="6.0e-5Jy", psfmode="cl
    → ark", imagermode="csclean", ftmachine="mosaic", mosweight=False,
    → scaletype="SAULT", multiscale=[], negcomponent=-1, smallscalebia
    → s=0.6, interactive=False, mask="", nchan=-1, start='22.6794GHz', w
    → idth='2MHz', outframe="", veltype="radio", imsize=myimsize, cell=
    → mycell, phasecenter="", restfreq="23.38348GHz", stokes="I", weigh
    → ting="natural", robust=0, uvtaper=False, outertaper=[''], innerta
    → per=['1.0'], modelimage="", restoringbeam=[''], pbcor=False, minp
    → b=0.2, usescratch=True, noise="1.0Jy", npixels=0, npercycle=100, c
    → yclefactor=1.5, cyclespeedup=-1, nterms=1, reffreq="", chaniter=F
    → alse, flatnoise=True, allowchunk=False)
339 #print 'Creating dirty cube for flux reference.'

```

```

340 #clean(vis='fluxref.ms', imagename='fluxref_cube.ms', outlierfile="
    ↪ ", field="", spw="", selectdata=True, timerange="", uvrange="", ant
    ↪ enna="", scan="", observation="", intent="", mode="frequency", res
    ↪ mooth=False, gridmode="", wprojplanes=-1, facets=1, cfcache="cfca
    ↪ che.dir", rotpainc=5.0, painc=360.0, aterm=True, psterm=False, mte
    ↪ rm=True, wbawp=False, conjbeams=True, epjtable="", interpolation=
    ↪ "linear", niter=0, gain=0.05, threshold="6.0e-5Jy", psfmode="clar
    ↪ k", imagermode="csclean", ftmachine="mosaic", mosweight=False, sc
    ↪ aletype="SAULT", multiscale=[], negcomponent=-1, smallscalebias=
    ↪ 0.6, interactive=False, mask="", nchan=-1, start='22.6794GHz', wid
    ↪ th='2MHz', outframe="", veltype="radio", imsize=myimsize, cell=my
    ↪ cell, phasecenter="", restfreq="23.38348GHz", stokes="I", weighti
    ↪ ng="natural", robust=0, uvtaper=False, outertaper=[''], innertape
    ↪ r=['1.0'], modelimage="", restoringbeam=[''], pbcor=False, minpb=
    ↪ 0.2, usescratch=True, noise="1.0Jy", npixels=0, npercycle=100, cyc
    ↪ lefactor=1.5, cyclespeedup=-1, nterms=1, reffreq="", chaniter=Fal
    ↪ se, flatnoise=True, allowchunk=False)
341 ', '
342 #####
    ↪ #####
343 # Create spectra of the flux calibrator, phase reference and
    ↪ target. #
344 # Flux calibrator.
345 specflux(imagename='fluxref_cube.ms', region='fluxref_region',
    ↪ chans='', stokes='I', mask='', function='flux density',
    ↪ unit='GHz', major='', minor='', logfile='fluxref_spectrum.txt')
346 # Phase reference.
347 specflux(imagename='phaseref_cube.ms', region='fluxref_region',
    ↪ chans='', stokes='I', mask='', function='flux density',
    ↪ unit='GHz', major='', minor='', logfile='fluxref_spectrum.txt')
348 # Target source
349 specflux(imagename='target_cube.ms', region='fluxref_region',
    ↪ chans='', stokes='I', mask='', function='flux density',
    ↪ unit='GHz', major='', minor='', logfile='fluxref_spectrum.txt')
350 # End of step 12.
    ↪ #
351 #####
    ↪ #####
352 ', '
353 # End of step 12. #
354 #####
355
356 #####
357 # Step 13: Perform image plane continuum subtraction. #
358 mystep = 13
359 if (mystep in thesteps):
360     imcontsub(imagename=mycube+'.image',
        ↪ linefile='target_K_cube.imcontsub',
        ↪ contfile='target_K_cube.imcontinuum', fitorder=1, region='',
        ↪ box='', chans='0~320,>380', stokes='I')

```

```
361 # End of step 13. #  
362 #####
```